5-2022

Nucleate boiling under different gravity values: numerical simulations & data-driven techniques.

Sandipan Banerjee
University of Louisville

NUCLEATE BOILING UNDER DIFFERENT GRAVITY VALUES: NUMERICAL SIMULATIONS & DATA-DRIVEN TECHNIQUES

By
Sandipan Banerjee

A Dissertation
Submitted to the Faculty of the
J B Speed School of Engineering
of the University of Louisville
in Partial Fulfillment of the Requirements
for the Degree of

Doctor of Philosophy
in Mechanical Engineering

Department of Mechanical Engineering
University of Louisville
Louisville, Kentucky

May, 2022

NUCLEATE BOILING UNDER DIFFERENT GRAVITY VALUES: NUMERICAL SIMULATIONS & DATA-DRIVEN TECHNIQUES

By

Sandipan Banerjee

Dissertation approved on

March 29 2022

by the following dissertation Committee:

Dissertation Director
Dr. Yongsheng Lian

Dr. Ellen Brehob

Dr. R. Eric Berson

Dr. Sam Park

Dr. Stuart Williams

ACKNOWLEDGMENTS

I would first like to express my deepest gratitude to my advisor, Dr. Yongsheng Lian, for providing me the opportunity to work and learn under him. I thank him for providing insightful feedback, sharing his valuable expertise, and for guiding and mentoring me throughout the course of my graduate studies at University of Louisville. You are everything one could look for in an advisor. You made my PhD an interesting and memorable experience. I will always be grateful to you for your support and kindness. Thank you for being such a great role model.

I thank Dr. Ellen Brehob, Dr. R. Eric Berson, Dr. Sam Park and Dr. Stuart Williams for being on my dissertation committee. Special thanks to Dr. Mark Sussman at Florida State University for his constant guidance throughout my time here at Louisville through online sessions. Our conversations always inspired me to work harder. I learnt a lot from him. I would also like to thank my colleagues for the amazing conversations we had in the lab: Ahmed Islam, Huan Jiang, and Zhenan Zhang.

From oceans apart, I thank my parents and brother for their unequivocal support and blessings. I thank my wife, Preetha, for her constant support and understanding, especially when times were hard. You kept me going on and this work would not have been possible without your counsel. This dissertation is dedicated to you.

Finally, I would like to acknowledge the financial support from the University Fellowship awarded by the University of Louisville.

ABSTRACT

NUCLEATE BOILING UNDER DIFFERENT GRAVITY VALUES: NUMERICAL SIMULATIONS & DATA-DRIVEN TECHNIQUES

Sandipan Banerjee

March 29 2022

Nucleate boiling is important in nuclear applications and cooling applications under earth gravity conditions. Under reduced gravity or micro-gravity environment it is significant too, especially in space exploration applications. Although multiple studies have been performed on nucleate boiling, the effect of gravity on nucleate boiling is not well understood. This dissertation primarily deals with numerical simulations of nucleate boiling using an adaptive Moment-of-Fluid (MoF) method for a single vapor bubble (water vapor or Perfluoro-n-hexane) in saturated liquid for different gravity levels. Results concerning the growth rate of the bubble, specifically the departure diameter and departure time have been provided. The MoF method has been first validated by comparing results with a theoretical solution of vapor bubble growth in super-heated liquid without any heat-transfer from the wall. Next, bubble growth rate and heat transfer results under earth gravity, reduced gravity and micro-gravity conditions are reported and they are in good agreement with experiments. A new method is proposed for estimating the bubble diameter at different gravity levels. This method is based on an analysis of empirical data at different gravity values and using power-series curve fitting to obtain a generalized bubble growth curve irrespective of the gravity value. This method is shown to provide a good estimate of the bubble diameter for a specific gravity value and time.

A new hybrid approach is proposed for calculating the contribution of the depletable liquid micro-layer trapped between the vapor bubble and the heater wall for numerical simulations in micro-gravity conditions is proposed in this work. This technique does not "model" the micro-layer, but calculates the contribution of the vapor flux from the micro-layer into the bubble and distributes it over the cells where the micro-layer should be present. The micro-layer is depletable because an evaporation term is part of the equation which maintains the reduction in the thickness of the micro-layer consistent with the behavior reported in experiments. Results for nucleate boiling simulations under micro-gravity conditions are reported using the proposed micro-layer approach in comparison with experiments performed on the International Space Station. Results for bubble growth rate, bubble shape and heat-flux are in good agreement with experiments and are verified with two different time-instants in the bubble life cycle.

Additionally, a data-driven model is proposed for the prediction of heat-flux from experimental parameters like wall super-heat, gravity, liquid sub-cooling, etc. Experimental data from multiple experiments under varying conditions for different liquids have been performed to date. Artificial Neural Networks (ANNs) have been used to predict nucleate boiling heat flux by learning from a dataset of twelve experimental parameters across 231 independent samples. An approach to reduce the number of parameters involved is proposed to increase model accuracy. The approach consists of two steps. In the first step, a feature importance study is performed to determine the most significant parameters. Only important features are used in the second step. In the second step, dimensional analysis is performed on these important parameters. Neural network analysis is then conducted based on the dimensionless parameters. The results indicate that the proposed feature importance study and dimensional analysis can significantly improve ANN performance. The results show that model errors based on the reduced dataset are considerably lower than those based on the

initial dataset. The study based on other machine learning models also shows the reduced dataset generates better results. The results also show that ANN outperforms other machine learning algorithms and outperforms a well-known boiling correlation equation. The effect of parameters on heatflux has been quantified, and the effect of parameters on different physical sub-processes in nucleate boiling has been analyzed. The effect of parameters on the boiling regimes has also been investigated. Additionally, the feature importance study concludes that wall superheats, gravity and liquid subcooling are the three most significant parameters in the prediction of heat flux for nucleate boiling.

The key contributions made in this work are listed below:

- MoF method simulations for nucleate boiling has been performed. Simulation results in earth gravity, and reduced gravity are in good agreement with experiments.
- A data-driven technique for prediction of effect of gravity on bubble growth rate has been proposed.
- A novel depletable microlayer approach for microgravity is proposed, results for bubble growth rate, bubble shape, and heat-flux are comparable to experiments performed on ISS.
- A novel data-driven technique has been used for heatlfux prediction. ANN outperforms XGB (Extreme Gradient Boosting), RFR (Random Forest Regression) and Rohsenow correlation in heatflux prediction.
- Dimensional Analysis and Feature Importance techniques help in reducing ANN error from 25.7% to 9.12%.

- Gravity, Wall super heat, and Liquid subcooling are the three most significant parameters in heatflux prediction. Novel results of quantification of parameter contribution in each boiling regime has been reported.

TABLE OF CONTENTS

LIST OF TABLES

LIST OF FIGURES

CHAPTER I

INTRODUCTION

1 Overview of Boiling Process

Boiling is a process which although is very common in residential as well as industrial field, is not completely well understood in the scientific community. One of the major importance of boiling process lies specifically in the heat-flux. A sample of the classical pool boiling curve is shown in figure 1.

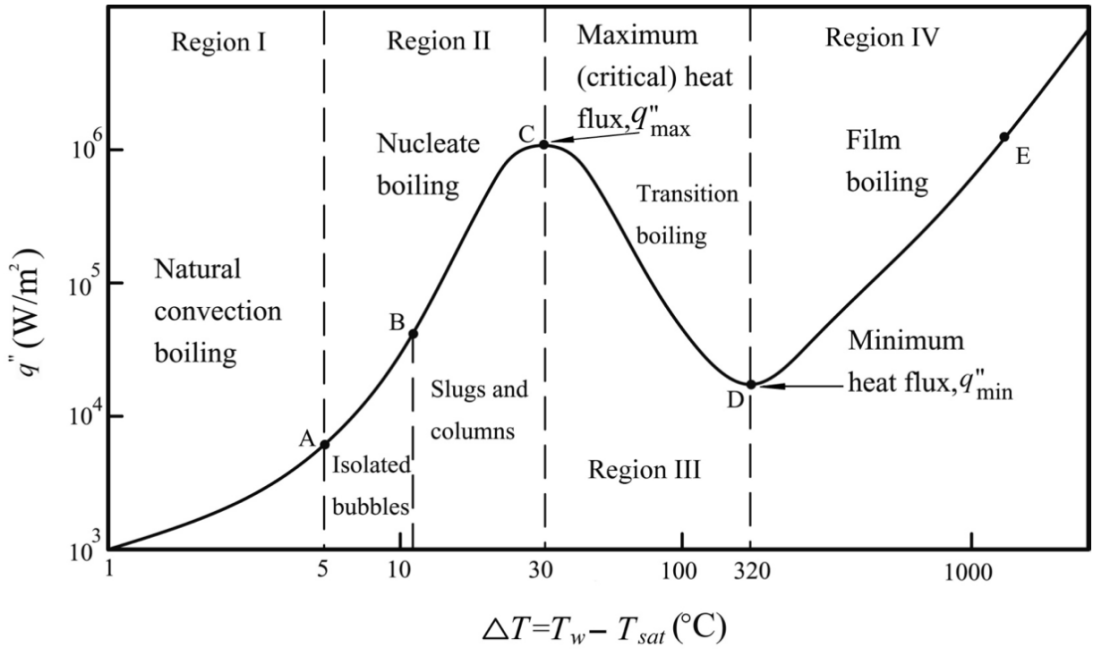

Figure 1. Boiling curve for water at 1 ATM pressure (Image Source: Transport Phenomena in Multi-phase Systems, by: Amir Faghri, Yuwen Zhang, 2006) [1]

Typically when a solid heater is submerged in a liquid which is maintained at its saturation temperature (T_{sat}), and the solid heater wall is at a higher temper-

ature (T_{wall} or T_w, both notations would be used interchangeably through out this dissertation), then the wall super-heat (defined as the difference between the wall temperature and the liquid saturation temperature, $\Delta T = T_w - T_{sat}$) is what drives the heating process. Figure 1 shows how the heat-flux varies with increasing wall super-heat. At low wall super-heats, heat transfer is mainly through natural convection, as the excess heat from the solid is used to heat up the bulk liquid shown in Region I. At Point A, starts region II which is denoted as ONB (Onset of Nucleate Boiling). A sharp increase in heat-flux is observed from point A. In this region of the plot, bubbles start to form. It should be noted that typically bubble nucleation occurs at kinks or imperfections in rough areas of the surface as the trapped gas molecules in the crevices add their free surface energy, and lesser energy is required for bubble nucleation. From point A to B, isolated single bubble formation is observed. The bubbles are held at the solid wall due to the surface tension force. These bubbles nucleate, grow to a certain size due to change in phase of surrounding liquid into vapor and finally depart when they are larger in size (i.e. when the buoyancy force exceeds the surface tension force). From point B onward, the heat-flux keeps increasing and isolated individual bubbles typically merge to form vapor slugs and vapor columns till it reaches point C. Point C is when the heat-flux reaches its maximum value. It is also know as Critical Heat Flux and typically denoted as CHF. Beyond the critical heat flux, the heat-flux starts to drop with increasing wall super-heat from point C to D, when it reaches the minimum heat-flux. This region is transition boiling. Beyond point D, vigorous boiling is observed which is the film boiling stage and heat-flux is again observed to increase.

The interest in Nucleate boiling phase mainly arises due to the high heat-flux. Energy can be efficiently transported using this mechanism which makes it suitable to industrial cooling processes, such as in Nuclear power plants. It can be argued that heat-flux in similar range to that of nucleate boiling phase would also be possible at

some time during film boiling phase as well (somewhere between point D and E in figure 1), however, it should be noted that the wall super heat required to reach film boiling is much higher, so much more energy needs to be used to reach that high wall super-heat (ΔT). At such high temperatures, damages to the heater wall could also be expected. Nucleate boiling achieves the high heat-flux with much lower energy expenditure. However, the problem lies in the ability to control the heat-flux such that it does not reach the CHF as this process very quickly reaches the CHF, and once it does the heat-flux starts decreasing which does not solve the purpose. The broader goal is to be able to reach and sustain the heat-flux at a level just near the CHF. In order to find that optimum value, a thorough understanding of the nucleate boiling process is required. As a first step the physics behind the isolated bubble regime needs to be understood well.

2 Background and Motivation

Correlations between the heat-flux and wall super-heat have been made with empirical results or based on modeling of sub-processes. Two main empirical correlations are discussed here in short. Rohsenow (1952) ([8]) related the heat-flux, $\dot{q}$ to the wall super heat, ΔT_w by the assumption of a single phase forced convection problem:

$$\frac{c_{pl}\Delta T_w}{h_{fg}} = C_s \left[\frac{\dot{q}\sqrt{\dfrac{\sigma}{g\left(\rho_l - \rho_v\right)}}}{\mu_l h_{fg}} \right]^{1/3} Pr_l^{1\text{or}1.7} \tag{1}$$

The power of 1/3 on the Reynolds Number and the power of 1 for water and 1.7 for all other liquids to the Prandtl Number (Pr) were obtained empirically. C_s depends on heater material and fluid combination. In equation 66, c_p is the specific heat, $\dot{q}$ is the heat-flux, h_{fg} is the latent heat of vaporization, σ is the surface tension, g is the acceleration due to gravity, ρ_l, ρ_v are the liquid phase and vapor phase densities respectively. μ_l is the viscosity of the liquid.

Stephan and Abdelsalam (1980) ([9]) provided a correlation valid for all liquids by determining the important fluid property groups using regression analysis. The correlation provided by them is given as:

$$\frac{\dot{q}D_d}{\Delta T k_l} = 0.23 \left(\frac{\dot{q}D_d}{T_{sat}k_l}\right)^{0.674} \left(\frac{\rho_v}{\rho_l}\right)^{0.297} \left(\frac{h_{fg}D_d^2}{\alpha_l^2}\right)^{0.371} \left(\frac{\rho_l - \rho_v}{\rho_l}\right)^{-1.73} \left(\frac{\alpha^2\rho_l}{\sigma D_d}\right)^{0.35} \quad (2)$$

The correlation provided by equation 2 does not consider the variation in degree of surface wettability, while the correlation provided by equation 66 does not consider heater geometry. The mechanism based correlations typically deal with 3 sub-processes ([10]), they are:

1. Number density of nucleation sites
2. Bubble departure diameter
3. Bubble release frequency

The number density of nucleation sites are determined by solid surface properties and thermal response of the substrate. Generally, for a slow growing bubble its departure diameter is believed to be determined by buoyancy and surface tension while by liquid inertia and surface tension for a fast growing bubble. The bubble release frequency is dependent on the bubble diameter at departure and bubble growth rate. For the understanding of single bubble dynamics, an in-depth study of the bubble departure diameter and bubble growth rate is crucial. Multiple correlations for the above subprocess have been proposed. Some key correlations are briefly discussed here. Fritz (1935) [11] correlated the bubble departure diameter (D_d) with the contact angle (ϕ), gravity (g), surface tension (σ), and densities of liquid (ρ_l), and vapor (ρ_v), respectively with:

$$D_d = 0.0208\sqrt{\frac{\sigma}{g(\rho_l - \rho_v)}} \quad (3)$$

Correlation provided in equation 3, does not hold true for high pressure cases. Gorenflo (1986) [12] proposed a correlation at high heat-flux:

$$D_d = C_1 \left(\frac{\mathrm{Ja}^4 \alpha_l^2}{g} \right)^{1/3} \left[1 + \sqrt{1 + \frac{2\pi}{3\mathrm{Ja}}} \right]^{4/3} \tag{4}$$

where α is the thermal diffusivity of the liquid, Ja is the Jakob number which is defined as:

$$\mathrm{Ja} = \frac{\rho_l c_{pl} \Delta T}{\rho_v h_{fg}} \tag{5}$$

and C_1 is a constant which has different values for different liquids. So far a correlation for the departure diameter of a bubble has not been proposed that has shown reasonable agreement with a wide variety of liquids under different conditions. As per [10], the main reason for not having a working correlation lies in the lack of knowledge of the temperature and velocity fields both of which have temporal and spatial variation.

In order to get a better correlation, one way could be performing numerical simulations of a single vapor bubble growth by varying different conditions like the wall-super-heat, gravity, the test liquid itself, and the effect of each variable could be well understood. It should be noted that numerical simulation of the nucleate boiling is a challenging task, mainly because of the multiple phases involved, with phase change occurring between the two predominant phases of liquid and vapor. Additionally, the vapor-liquid interface which defines the shape of the bubble is also critical for numerical simulations. Typically, a heater wall (solid) is submerged in a liquid maintained at its saturation temperature. The temperature of the solid wall is higher than the liquid saturation temperature. ($\Delta T_{wall} = T_{wall} - T_{sat}$)

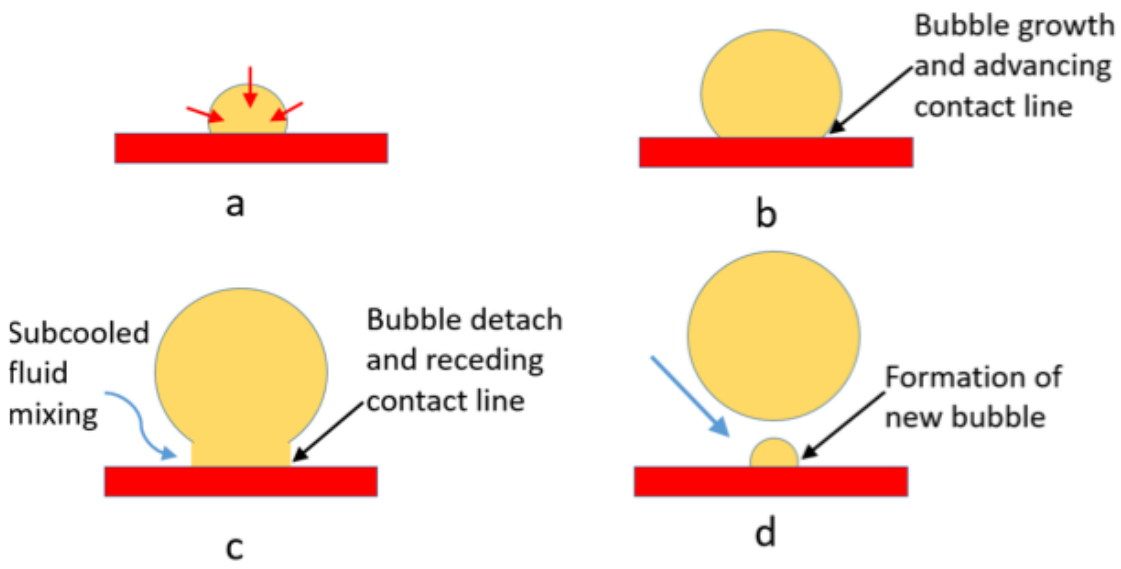

Figure 2. Stages of vapor bubble life cycle in nucleate boiling under earth gravity conditions)

Typically, the life cycle of a single vapor bubble in earth gravity consists of four stages as shown in figure 2:

1. **Nucleation-** A vapor bubble is formed or nucleated due to kinks and roughness on the heater surface.

2. **Bubble Growth-**

   - The nucleated vapor bubble starts to grow due to phase change of the surrounding liquid due to the heat transfer from the solid wall till it reaches a peak size.
   - It should be noted that as the bubble size increases, the bubble base radius increases as well. The bubble base radius is also called the contact line, which signifies the region of the vapor bubble coming in contact to the wall.
   - The bubble is held at its base to the wall by the surface tension force acting between the vapor and the solid wall.

3. **Departure phase-** In the departure phase, bubble base radius (contact line) starts to reduce, as the buoyancy force increases due to larger volume of the vapor bubble.

4. **Lift Off-** Bubble lifts off or pinches off when the buoyancy force exceeds the surface tension force.

Once a bubble lifts off, a new bubble generally forms or nucleates at the same location. One of the major factors of nucleate boiling is gravity. Typically, at the International Space Station (ISS), an efficient medium of heat transfer is required to make the components more compact. Conventional techniques like heat pipe cannot be used, as it was found that the hot end of the heat pipe quickly floods under micro-gravity conditions [13]. Nucleate boiling on the other hand could provide a better alternative solution of the problem and as nucleate boiling heat transfer performance strongly depends on the gravity level, it is critical to understand the effect of gravity over a wide range of gravity levels. There have been multiple experimental, as well as numerical studies performed. A brief review is presented below in the following two sub-sections.

Experimental studies of nucleate pool boiling under reduced and micro gravity conditions

It is well known that under reduced gravity nucleate pool boiling behavior is different. Siegel and Usiskin (1959) [14] performed one of the first studies to investigate nucleate boiling under reduced gravity conditions. They performed nucleate boiling experiments under free fall conditions and observed that vapor bubbles remained attached to the heater surface instead of departing as under earth gravity. This could be attributed to the reduced buoyancy force with reduction in gravity. The reduction in buoyancy does not allow the buoyancy force to overcome the surface tension force which holds the vapor bubble at the surface. Siegel and Keshock (1964) [5]

observed that under reduced gravity the bubble growth period was longer and the bubble departure diameter was larger. Their observation is consistent with that of Qiu *et al.*(2002) [15] who conducted experiments on parabolic flights. Kannengieser *et al.*(2010) [16] conducted boiling experiments on board the Sounding Rocket Maser 11. They found a large primary bubble stayed attached to the heater surface during the experiment. Using the Micro-heater Array Boiling Experiment (MABE) on the ISS, Raj *et al.*(2012) [17] performed nucleate boiling experiment using perfluoro-n-hexane (pfnh) which is a linear isomer of C_6F_{14}. This isomer is the principal constituent of FC-72 which is widely used as an electronic cooling fluid. They reported a large vapor bubble covering the entire heater surface and did not observe bubble lift off. Warrier *et al.*(2015) [18] also performed experiments under micro-gravity conditions using pfnh as the test liquid and reported a large bubble being formed near the heater in their experiment on the ISS. The large bubble formation could be seen as a result of reduced buoyancy and merging of small bubbles. At low wall super-heat temperature, the bubble departure was not observed, however at high wall super-heats, the large bubble could depart from the surface. Even if the bubble departed, the authors observed the bubble to continue to hover near the heater wall. They concluded that under micro-gravity conditions surface tension and inertia forces dominate during most of the bubble growth period, until a bubble reaches a relatively large size. The experimental data of Usiskin and Siegel (1961) [19] and Straub *et al.*(1990) [20] indicated that nucleate boiling heat transfer rate was insensitive to the gravity. However, Zhao *et al.*(2009) [21], conducted nucleate pool boiling experiment aboard a recoverable satellite and observed that under micro-gravity the nucleate pool boiling heat transfer rate was lower than that under terrestrial gravity. The critical heat flux values were about 3 orders of magnitude lower than that obtained at earth gravity. Warrier *et al.*(2015) [18] performed nucleate boiling experiments at micro-gravity and also at earth normal gravity using identical heating surface. Their results showed that

heat transfer coefficients decrease with the decrease in gravity level. Their observation is consistent with that of Straub *et al.*(1990) [20] too. Raj *et al.*(2012) [17] showed that at lower wall super-heats micro-gravity boiling heat fluxes were larger than those obtained at normal earth gravity, but the trend reversed at higher wall super-heats. The anomaly may be caused by the small heater sizes and high wall super-heats which resulted in film boiling instead of nucleate boiling in the experiments of Raj *et al.*(2012) [17]. Kannengieser *et al.*(2010) [16] showed that when the wall temperature was lower than the saturation temperature the Marangoni convection was the dominant heat transfer mechanism, while when it was higher than the saturation temperature, evaporation at the bubble base was the dominant heat transfer mechanism. However, they found little difference in the boiling heat transfer rates under micro gravity and earth gravity conditions. Experiments conducted on the ISS also showed the dependence of the heat flux on wall super-heat decreased as the pressure or liquid sub-cooling increased under micro-gravity (Warrier *et al.*(2015) [18]). However, the dependence of heat flux on wall super-heat was weakened at earth normal gravity in comparison to that under micro-gravity conditions. It is believed that geometry of the heated surface is a major factor in the differences observed. In general, experiments conducted using wires showed little or no change in nucleate boiling heat transfer as gravity was changed while experiments using flat heated surfaces generally showed reduced heat transfer under micro-gravity. With the advent of computational resources, CFD has also been used to study nucleate boiling by performing numerical simulations. A review of the significant past work of numerical simulations is provided in the following sub-section .

Numerical studies of nucleate pool boiling under reduced and micro gravity conditions

One of the first numerical approaches in Nucleate pool boiling was studied by Lee and Nydahl (1989) [22]. They modeled bubble dynamics in saturated nucleate pool boiling on a heated horizontal surface by solving the axi-symmetric Navier-Stokes and energy equations. They calculated the bubble growth rate, but they did not consider the change in bubble shape as their model assumed that the bubble maintained a hemispherical shape during its growth. Their model included a wedge-shaped micro-layer whose thickness was adjusted in an ad-hoc way to match the experimentally measured bubble growth. Mei *et al.*(1995) [23] investigated bubble growth and departure. However, their study ignored the hydrodynamics of the liquid motion by the growing bubble. Furthermore, their model assumed that heat transfer to the bubble was only through the micro-layer, which is not an accurate assumption for saturated liquid. Welch (1995) [24] used an interface tracking method to study the boiling problem. However, he only considered small distortions due to the limited capability of his method in handling topology changes. Son *et al.*(1999) [6] simulated nucleate boiling by assuming axi-symmetric and laminar flow. They used the level set method to capture the vapor-liquid interface. In their model, the computational domain was divided into micro and macro regions. The macro region included the bubble and the liquid surrounding the bubble. The micro region consists of the thin liquid micro-layer that forms underneath the bubble. In the micro region, the lubrication theory was used to model the micro-layer. The two regions were matched near the outer layer of the micro-layer. The model predicted the bubble growth but not the relation between the heat flux and wall super-heat. Abarajith *et al.*(2002) [25] used this model to investigate the effect of contact angle. Later, Abarajith *et al.*(2004) [26] used that model to study bubble merger in reduced gravity. They found that bubble merger in a plane lead to early bubble lift-off under low gravity conditions due to

the additional lift-off force developed from the merger process. They also found that in most cases the bubble departure diameter for merged bubbles was much smaller than that for a single bubble case. The bubble merger also increased time averaged wall heat flux. However, as pointed out by Tanguy *et al.*(2014) [27], the use of smoothing of the velocity jump condition at interface can lead to misleading mass prediction. Shin *et al.*(2005) [28] simulated three-dimensional nucleate boiling using the level contour reconstruction method. Their model included the effect of nucleation site density and was capable of predicting the relationship between the heat flux and the wall super-heat in a realistic surface. But they did not include contact line dynamics in their calculations. Wu and Dhir (2011) [29] conducted numerical simulations to investigate the effect of non-condensable gases. They found that accumulation of non-condensable gas caused a drop in the local vapor pressure and reduced the effect of sub-cooling. Direct numerical simulation of nucleate boiling imposes significant challenges due to the issues of wall contact. Further, the coupling of unsteady mass, momentum and energy transport with the complicated liquid-vapor interface dynamics and inter-facial physics such as surface tension and discontinuity in material properties pose numerical challenges. Tanguy *et al.*(2014) [27] conducted extensive simulation to compare different numerical methods for the simulation of boiling flows. They found that solving the thermal boundary layer accurately around the bubble and computation of the boiling mass flow rate are critical for the boiling flow simulation. One of the major challenges of numerical simulations of multi-phase problems is to capture the interface between two phases. In the MoF method used in this work, comparison between a reference centroid information corresponding to the interface is made with actual centroid information. The difference between the actual centroid and reference centroid is minimized while keeping the actual volume fraction and reference volume fraction same. This ensures a sharp interface. Multiple interface tracking methods have been proposed so far. A general summary of the

interface tracking mechanisms are included in Table 1.

Method	Publication	Summary of work
Level Set Method	Son and Dhir (1998) [30]	They performed numerical simulation of film boiling near critical pressures. The interface is captured by a level set method which is modified to include the liquid-vapor phase change effect.
	Gibou *et al.*(2007) [31]	They describe a sharp interface capturing method for the study of incompressible multiphase flows with phase change. They use the level set method to track the interface between the two phases and uses a ghost fluid approach to impose the jump conditions at the interface.
	Tanguy *et al.*(2007) [32]	They report simulations of two phase vaporizing flows. They use use both the Level Set Method and the Ghost Fluid Method to capture the interface motion accurately and to handle suitable jump conditions.
	Can and Prosperetti (2012) [33]	They report a a finite-difference computational method suitable for the simulation of vapor–liquid flows in which the dynamical effects of the vapor can be approximated by a time-dependent, spatially uniform pressure acting on the interface which is described by a level set method modified with a high-order "subcell fix" with mass conservation properties.
Front Tracking Method	Univerdi and Tryggvason (1992) [34]	They propose a method to simulate unsteady multi-fluid flows in which a sharp interface or a front separates in-compressible fluids of different density and viscosity is described. The flow field is discretized by a conservative finite difference approximation on a stationary grid, and the interface is explicitly represented by a separate, unstructured grid that moves through the stationary grid.
	Juric and Tryggvason (1998) [35]	They propose a numerical method to simulate liquid–vapor phase change. In this method, the conservation equations of mass, momentum and energy are discretized by a finite difference method on a regular grid and the phase boundary is explicitly tracked by a moving front.
Volume of Fluid Method	Welch and Wilson (2000) [36]	They report a numerical method for the simulation of flows with mass transfer due to changes of phase. They perform simulations on horizontal film boiling and use a volume of fluid (VOF) based interface tracking method in conjunction with a mass transfer model and a model for surface tension.

Method	Publication	Summary of work
Volume of Fluid Method (contd)	Ghosh *et al.*(2006) [37]	They report a numerical model based on the volume-of-fluid (VOF) method in spherico-symmetric geometry containing two immiscible phases They provide simulation results for rapid collapse phenomenon of vapor film around a hot metal in sub-cooled water.
	Yuan *et al.*(2008) [38]	This paper presents a numerical method for the simulation of boiling flows on non-orthogonal body-fitted coordinates. The volume-of-fluid (VOF) method based on piece-wise linear interface construction (PLIC) is used to track liquid-vapor interface and is extended to body-fitted coordinates.
	Haelssig *et al.*(2010) [39]	They used VoF for DNS of interface dynamics and simultaneous inter-phase heat and mass transfer in systems with multiple chemical species. The method incorporates the full interface species and energy jump conditions for vapour–liquid inter-phase heat and mass transfer. They present results of ethanol–water system for the cases of wetted-wall vapor–liquid contacting and vapor flow over a smooth, stationary liquid.
Coupled Level Set and Volume of Fluid	Tomar *et al.*(2005) [40]	They use a coupled level-set and volume-of-fluid method for modeling incompressible two-phase flows with surface tension. CLSVOF conserves mass and captures the complicated interfaces accurately. They report results for film boiling.
Phase Field Method	Jamet *et al.*(2001) [41]	In this method, the interface is described as a three-dimensional continuous medium across which physical properties vary by imposing that the internal energy of the fluid depends on its density gradient. They explore if this method can be used for cases with moving contact lines.
	Badillo (2012) [42]	They provide a phase-field model for simulation of bubble growth in the diffusion-controlled regime. The model accounts for phase change and surface tension effects at the liquid-vapor interface. They split the single phase field PDE to two separate equations, one controls the phase change and the other one controls the shape of the phase-field profile across the diffuse interface.

Method	Publication	Summary of work
Color Density Function	Sato and Ničeno (2013) [3]	They proposed a phase-change model for a mass-conservative interface tracking method. The mass transfer rate is directly calculated from the heat flux at the liquid–vapor interface, and the phase change takes place only in the cells which include this interface. The method was used in a projection based Navier Stokes equation solver on a staggered finite-volume algorithm on Cartesian grids.

Table 1. Different numerical methods used for boiling problem

Current nucleate pool boiling designs still depend on empirical correlations or mechanistic models which either ignore or insufficiently model many important physical phenomena (i.e., bubble departure, merger, and micro-layer formation and evaporation between bubble and heater surface). Further, the gravity effect on nuclear pool boiling is only poorly understood. A thorough understanding of these important physical phenomena and the gravity effect is vital for safe and efficient nucleate pool boiling design.

3 Micro-layer Formation and Evaporation

During the initial phase of bubble growth, the vapor-liquid interface grows much more faster than the bubble base, as the surface tension inhibits the growth of the bubble base to some extent. In order to incorporate the rapid growth, the interface bends towards the base. This bending traps a thin layer of liquid under the vapor bubble and above the heater wall. This thin layer of liquid is called as the micro-layer. The thickness of the micro-layer is typically in the order of microns, hence the name "micro-layer". Snyder and Edwards ([43]) first proposed the existence of a liquid micro-layer. Cooper and Lloyd ([44]) confirmed its existence with validation from experimental results. The typical life-cycle of the liquid micro-layer is that it forms during the initial phase of the bubble growth, then the micro-layer grows as the bubble grows while it continues to contribute to the bubble growth through the

its evaporation. As the bubble enters the departure phase, the micro-layer reduces in size and finally gets completely depleted before the bubble departs. Experiments have been performed to study the micro-layer behavior. Moore and Mesler ([45]), Hendricks and Sharp ([46]) , Yabuki and Nakabeppu ([47]) tried to predict the initial micro-layer thickness from the measurements by calculating the total heat removal and the temperature distribution in the wall.

A typical micro-layer is shown in figure 3. In the figure, r_{ml}, corresponds to the radial extent of the micro-layer in relation to the vapor bubble base, and r_d corresponds to the dry-out radius. An even thinner layer of liquid called the adsorption layer is also present under the dry-out radius as well. However, the adsorption layer does not evaporate, hence makes no significant contribution to the bubble growth via heat transfer or mass flux of vapor. This has been confirmed by Urbano *et al.*([48]).

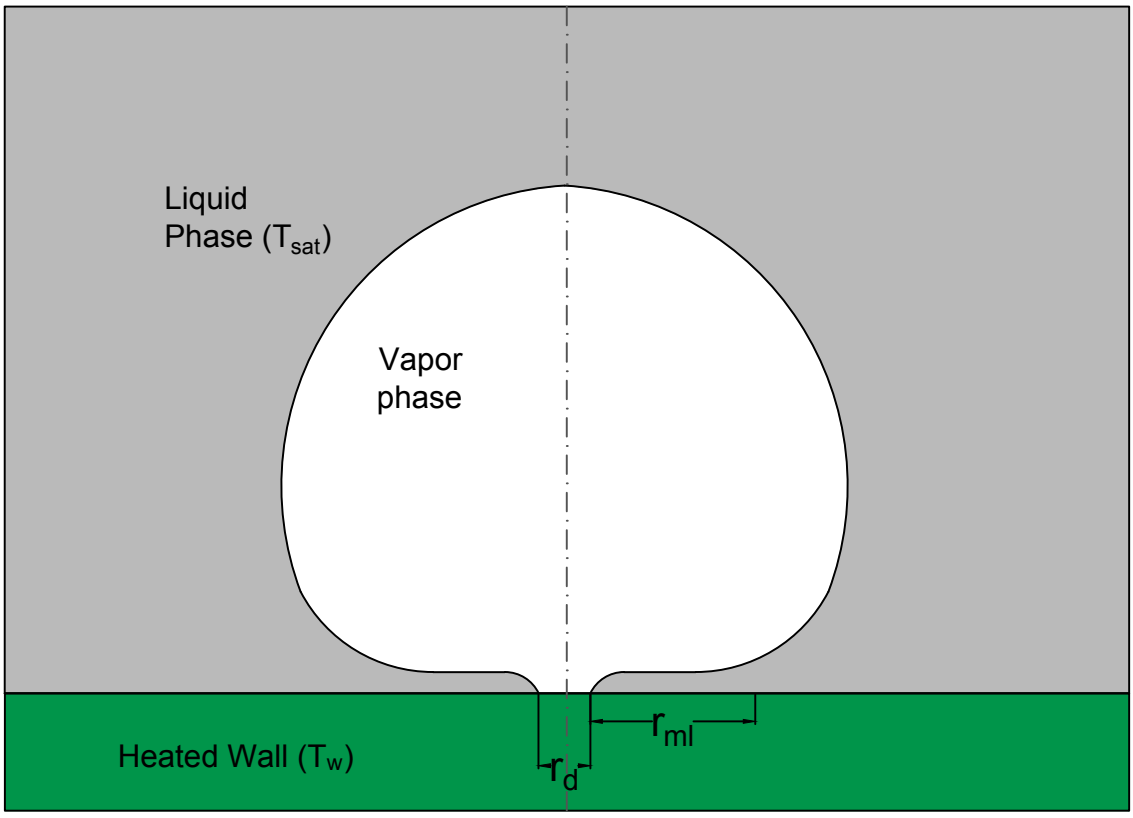

Figure 3. Typical Microlayer

Experiments have shown that the micro-layer typically extends almost for the entire radial extent of the bubble base, and its thickness being in the order of a few microns makes its aspect ratio to be very high. Moreover, since the micro-layer of liquid is the only thing that lies between the heater wall and the vapor bubble, it evaporates very rapidly, making it harder for measurements of the micro-layer size and thickness in experiments. This makes the uncertainty of the experimental correlations to be on the higher side. However, with advancement is optical photography some other studies have been performed as well. Jung and Kim ([49]) used interferometry and Utaka *et al.*([50]) used laser extinction method. Most of the experiments report the micro-layer thickness to be of a linear relationship with the bubble base radial location. [47] provided the correlation for the initial micro-layer thickness to be:

$$\delta = 0.0005099 r^{0.69} \tag{6}$$

Similar linear correlation have been provided by [50] as well:

$$\delta = 0.00446 r \tag{7}$$

However, both these correlations are for the specific case of water under earth gravity conditions. [50] also provided a similar correlation for ethanol as the test liquid, where the coefficient is different. For the case of ethanol the correlation is given as:

$$\delta_{ethanol} = 0.0102 r \tag{8}$$

As can be seen, the thickness maintains a linear profile with the radius for multiple liquids. These coefficients were based on empirical calculations. There are some analytical correlations available int he literature too. However, the ones that are analytical, typically estimate the so-called hydrodynamic thickness of the micro-layer. This refers to the micro-layer that would form if the bubble was considered to be growing only by vapor flux from the macro-layer region, i.e. if the evaporation of the

micro-layer was not taken into consideration VanStralen *et al.*([51]). [44] proposed the relation of the hydrodynamic thickness to be:

$$\delta_{hd} = 0.8\sqrt{\nu_l t} \tag{9}$$

where ν_l is the liquid kinematic viscosity and t is the time. Similar correlations with different coefficients have been proposed by Smirnov [52]:

$$\delta_{hd} = 1.04\sqrt{\nu_l t} \tag{10}$$

[51] proposed yet another different coefficient:

$$\delta_{hd} = 3.632\sqrt{\nu_l t} \tag{11}$$

These correlations did not consider the relation to be dependent on the radial location, and neither did they consider the wall-super heat temperature as a factor. Olander and Watts ([53]) provided an analytical formulation considering the above mentioned factors. They proposed:

$$\delta_{hd} = \frac{\pi}{4\sqrt{3}} \frac{\rho_v h_{fg}}{\rho_l c_{pl} \Delta T} \sqrt{\frac{\nu_l}{\alpha_l}} r \tag{12}$$

Although, [53] correlation takes into account the radial location, and wall super-heat into the formulation it does not consider the effect of depletion of the micro-layer.

As far as numerical simulations are concerned, there are considerable challenges in order to be able to account for the contribution of the micro-layer. Typically, the micro-layer thickness is in the order of (10^{-6}m) or microns, and the bubble radius is in the order of a few millimeters. So in order to fully resolve the micro-layer, the spatial resolution needs to be very fine to incorporate the length scale of the micro-layer thickness. This would make the computations very expensive as the domain of computation will need to be a lot larger, and each cell size would be very small, making the number of computations higher. In order to solve this issue, some form of modeling has been used in the research community. Wayner ([54])

proposed a model to consider the micro-layer contribution which was later modified by Stephan and Busse ([55]) and Son *et al.*([6]). The contact line model (also known as a triple line model in the literature) proposed by them addresses the line where the curved surface of the bubble intersects the heated surface. They divided the domain into macro and micro-region, where the micro-region consisted of the micro-layer area, and macro-layer consisted of the remaining portion of the domain. They solved the mass, momentum and energy conservation equations in both the regions. For the micro-layer, they approximated the momentum conservation equation by using lubrication theory. Using the conservation equations, a fourth order, non-linear differential equation is determined. This differential equation is solved to get the thickness of the micro-layer. The liquid flow into the micro-layer is considered to be driven by the pressure difference between the liquid pressure and vapor pressure. This micro-layer modeling approach showed to be in agreement with boiling experiments both in earth gravity and micro-gravity experiments. However, one of the major disadvantages of their model lies in the fact that the radial extent which the micro-layer encompasses corresponds to a very small portion of the bubble base. An example of the triple line model is shown in figure 4. The image on the right shows a zoomed in portion of the region near the triple point (i.e. where all three phases of liquid, vapor and solid, come into contact).

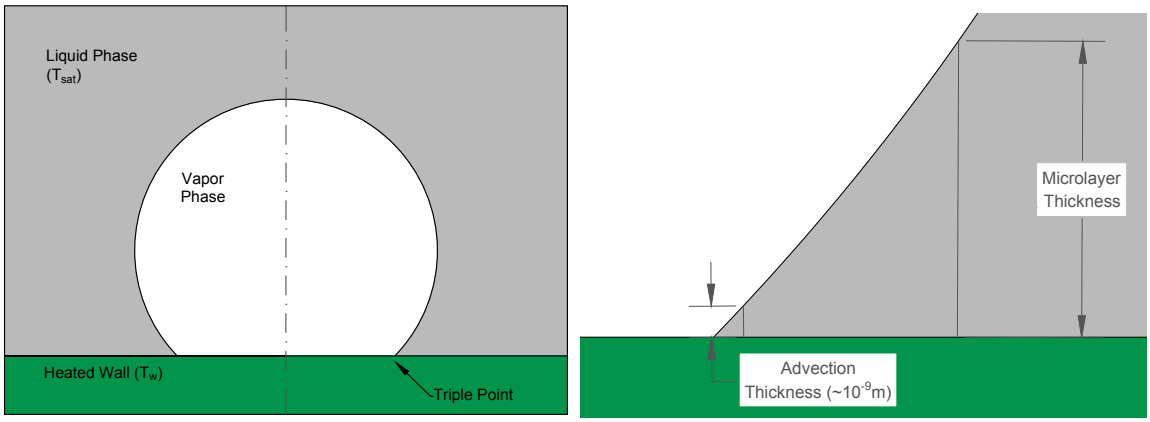

Figure 4. Microlayer in Triple Line Model or Contact Line Model

The contact line model is shown in figure 4. This is different from the actual micro-layer seen in experiments because the length of the micro-layer in the radial extent consists of a very small region which corresponds to the base of the triangle formed by the microlayer thickness line, the vapor bubble interface and the heater wall. In reality this assumption is not true, as experiments have shown that the micro-layer exists almost along the entire radial extent of the bubble base as shown in figure 3. This means that the evaporation of the micro-layer does not take into account of the entire region the micro-layer is present. Secondly, in reality the micro-layer has variable thickness, it grows initially and then reduces with time as it evaporates, however, this model assumes the micro-layer thickness as a constant value. This disadvantage extends to another related issue with the model. If the micro-layer size does not change, then the micro-layer does not deplete, which means micro-layer is present at all times, this is also not true, as experiments have proved that the micro-layer forms, grows in size, depletes away, so towards the very end of the bubble life cycle (i.e. in the departure phase), the micro-layer should no longer be present, making the contribution of vapor mass-flux from the micro-layer to the bubble to be zero. This is not the case with this model, it considers the micro-layer to be present at all times, hence the contribution of micro-layer is being calculated even when it

should not be. These are some of the physical limitations of this specific model, but there is a numerical limitation too. Due to the vanishing gradient problem associated with the temperature, there is a requirement for the minimum size of the micro-layer, the requirement is typically that the micro-layer thickness has to be greater than one cell size of the computational domain resolution. This method would not be able to handle a thickness value of the micro-layer lower than the cell size. So, for cases with very thin micro-layer, a very fine resolution would be needed, making the computation expensive due to longer run times.

Sato and Ničeno [56] proposed a depletable micro-layer model. They simulated the growth and departure for a single vapor bubble from a heated surface using a sub-grid scale modeling approach for the micro-layer. Although this model produces results which are in good agreement in comparison to experiments with respect to bubble growth rate, heat transfer rate and other bubble dynamics parameters in general, there are two major limitations with this model. First, the model uses the below equation to predict the micro-layer thickness:

$$\delta = C_{slope} R \tag{13}$$

where δ is the micro-layer thickness, and R is the radius of the bubble base. C_{slope} is a constant value which is estimated from the empirical coefficient shown in equation 7 from [50]. It should be noted that the experiment of [50], was performed under earth gravity conditions, using water as the test liquid. So, the constant value of the parameter C_{slope}, used in this model would be valid only under the assumptions of these specific conditions. The model cannot be scaled to micro-gravity conditions where in other liquids are used for the experiments owing to the density ratio difference. Later Hänsch *et al.*([57], [58]), proposed a modification to the model, by replacing the C_{slope} term with an expression for the initial micro-layer thickness by performing a back calculation from the rate of micro-layer depletion and the thickness of the depleted micro-layer to generate the initial micro-layer thickness. The

depleted micro-layer thickness value is used from experiments. Additionally, Hänsch *et al.*model requires very fine resolution. They report that at the liquid-solid interface the grid size is $0.5\mu m$, and time-step size of $2ns$ was needed. Such fine resolution and small time-step size, would make the computation very expensive which is sort of antithetical to the use of a modeling approach itself. The goal of the modeling for micro-layer is to make the computations faster, so that very fine resolution is not needed. Moreover, the model proposed has not been tested under micro-gravity conditions. Typically, under earth gravity the bubble growth rate is found to be $t^{1/2}$ where, t is the time, but in micro-gravity conditions, the bubble growth rate in single bubbles has been observed to be $t^{1/3}$. This model does not provide any consideration for that.

In this work, we report nucleate pool boiling results at different gravity levels using a simulation tool based on a novel Moment-of-Fluid method (MoF) ([59–61]) and validate the simulation results using experimental data in order to further study important physical phenomena and their effects on nucleate pool boiling. In Chapter II, the MoF method is discussed and results for the validation of the MoF method is presented by comparing with the analytical solution of Scriven [62] which does not consider the presence of a heated wall. It is an analytical expression, that provides the growth rate of a vapor bubble which is immersed in a super heated liquid. In Chapter III, results from simulation of a single vapor bubble growth and departure in presence of a heater wall is compared with experimental results for earth gravity conditions. Simulation result of bubble growth in reduced gravity environment is also provided along with comparison of experimental result. A new method for estimating bubble diameter at different gravity levels for nucleate pool boiling is also proposed [63]. In Chapter IV, a novel hybrid approach for a depletable micro-layer for micro-gravity is proposed after an explanation on the need for using a micro-layer for this case. Also given is a brief summary of the existing micro-layer models

along with their advantages and limitations. The reported micro-layer approach does not technically model the micro-layer, but only estimates the contribution of the micro-layer evaporation to the bubble growth. Simulation results for bubble growth rate, and heat flux is presented using the proposed micro-layer approach for micro-gravity conditions. Comparison with experiments performed on ISS are provided, which shows reasonable agreement in bubble shape at a time-instant, growth rate as well as heat-flux. In Chapter V, an investigation into leveraging the state of the art machine learning techniques is performed with the goal of predicting the heat-flux as a function of different experimental variables. Conclusions are reported in Chapter VI.

For the earth and reduced gravity experiments, water is the test liquid (corresponds to results in Chapter II, and most of III (i.e. in all sections except section 1), and perfluoro-n-hexane is the test liquid for micro-gravity conditions (corresponds to results in section 1 of Chapter III and entire Chapter IV). The values used for the physical properties of both liquids are provided in table 2 below for reference.

Property	**Water (Units)**	**Perfluoro-n-hexane (Units)**
Density of Liquid (ρ_l)	958 (kg/m^3)	1500.785 (kg/m^3)
Density of Vapor(ρ_v)	0.5956 (kg/m^3)	11.46 (kg/m^3)
Latent heat of vaporization (h_{fg})	2257E3 (J/kg)	86097 (J/kg)
Thermal conductivity of liquid (k_l)	0.68 (W/mK)	0.0603 (W/mK)
Specific heat capacity of vapor (c_{pv})	2029 (J/kgK)	784 (J/kgK)
Specific heat capacity of liquid (c_{pl})	4217 (J/kgK)	992.01 (J/kgK)

Table 2. Physical properties of the two liquids simulated

CHAPTER II

NUMERICAL METHOD AND CODE VALIDATION

This Chapter describes the numerical method, and reports the results of the case for bubble growth in super heated liquid in absence of wall-heat transfer. This case is chosen as the validation case as an analytical solution to this problem is available (Scriven [62]). The method used for the simulations is Moment of Fluid which is based on the works of [59–61]. A description of the MoF method is provided below:

1 Numerical Method: MoF

Governing Equations

The governing equations to be solved are the mass conservation equation, momentum conservation equation, and the energy conservation equation for each material for in-compressible, immiscible, multi-phase flow, which are given as follows: For each material m:

$$\nabla \cdot \vec{u} = 0 \tag{14}$$

$$(\Phi_m)_t + \vec{V_I} \cdot \nabla \Phi_m = 0, \qquad m = 1, 2, \cdots, M \tag{15}$$

$$\frac{\partial}{\partial t}(\rho_m \vec{u}) + \nabla \cdot (\rho_m \vec{u} \otimes \vec{u}) = -\nabla \cdot p_m \mathbb{I} + \nabla \cdot \vec{\tau} + \rho_m \vec{g} \quad \text{if } \Phi_m(\vec{x}, t) > 0 \tag{16}$$

$$\frac{\partial}{\partial t}(\rho_m C_{p,m} T) + \nabla \cdot (\vec{u}_m \rho_m C_{p,m} T) = \nabla \cdot (k_m \nabla T) + \vec{\tau} : \nabla \vec{u} \quad \text{if } \Phi_m(\vec{x}, t) > 0 \tag{17}$$

where for material m:

- ρ_m is the density, p_m is the pressure, $\vec{g}$ is the acceleration due to gravity. $\vec{u}\,(u, v, w)$ is the velocity field, $C_{p,m}$ is the heat capacity per unit mass at constant pressure, k_m is the thermal conductivity.

- $\vec{V_I}$ is the interfacial velocity, computed by [27, 31]:

$$\vec{V_I} = \vec{V}_{vap} - \frac{\dot{m}}{\rho_{vap}}\vec{n}_{lv} \tag{18}$$

$$\dot{m} = \frac{[k\nabla T \cdot \vec{n}_{lv}]\,\Gamma}{h_{fg}} \tag{19}$$

  where $\vec{n}_{lv}$ is the normal vector at the interface Γ, which points from liquid to vapor phase, h_{fg} is the latent heat of vaporization.

- Φ_m is the level-set function:

$$\Phi_m\,(\vec{x}, t) = \begin{cases} > 0, & \vec{x} \in m\,(\text{material}) \\ \leq 0, & \text{otherwise} \end{cases} \tag{20}$$

- Temperature at the phase change front (vapor-liquid interface) is always assumed to be the saturation temperature T_{sat}.

- $\vec{\tau}$ is the deviatoric stress tensor for a Newtonian fluid,

$$\vec{\tau} = \mu_m \left(\nabla\vec{u} + \nabla\vec{u}^T\right) \tag{21}$$

- $\vec{\tau} : \nabla\vec{u}$ is the viscous diffusion term, which is included here in the formulation, but neglected in the numerical implementation.

The numerical method is described on a rectangular Cartesian grid where the velocities (u and v) are discretized on the cell face centers and other variables such as the pressure (p), cell centroids (x), level-set functions (Φ_m), volume fractions (F_m), and temperature are discretized at the cell centers. The location of the definitions of the variables are shown in figure 5, where Γ is the interface.

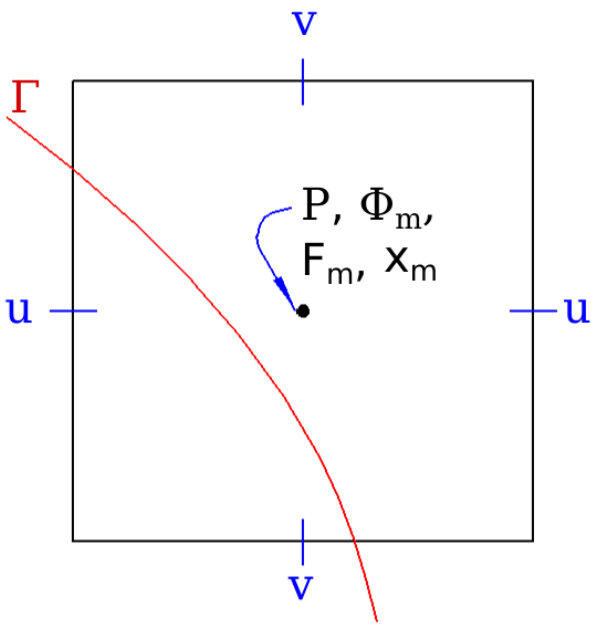

Figure 5. Variable definition in a cell

So, a single cell $\Omega_{i,j}$ centered at (x_i, y_j) is defined as:

$$\Omega_{i,j} = \left\{ \vec{x} : \left(x_i - \frac{\Delta x}{2}\right) < x < \left(x_i + \frac{\Delta x}{2}\right), \left(y_j - \frac{\Delta y}{2}\right) < y < \left(y_j + \frac{\Delta y}{2}\right) \right\} \quad (22)$$

The domain of material m in cell (i, j) is defined as $\Omega^m_{i,j}$, then the corresponding volume fraction (zeroth moment) and centroid position (first moment) are defined as:

$$F^m_{i,j,} = \frac{\int \Omega^m_{i,j} d\Omega}{\int \Omega_{i,j} d\Omega} \quad (23)$$

$$\vec{x}^m_{i,j,} = \frac{\int \Omega^m_{i,j} \vec{x} d\Omega}{\int \Omega_{i,j} d\Omega} \quad (24)$$

Jump Conditions

At the vapor-liquid interface, both liquid and vapor phase meet, so a jump condition needs to be applied at the boiling front Γ to maintain the conservation of mass, momentum and energy.

- **Mass Conservation:**

$$[\vec{u}]_\Gamma = -\dot{m}\left[\frac{1}{\rho}\right]_\Gamma \vec{n}_{lv} \tag{25}$$

where $[f] = f_{vap} - f_{liq}$ is the jump operator; and $\dot{m} = \rho_{vap}\left(\vec{u}_{vap} - \vec{V}_I\right)\cdot\vec{n}_{lv}$ is the change of local mass flow rate.

- **Momentum Conservation:** For in-compressible flows and Newtonian fluids, an appropriate jump in pressure must be satisfied at the boiling front to account for capillary, viscous and phase change effects,

$$[p]_\Gamma = \sigma\kappa + 2\left[\mu\frac{\partial\vec{u}_n}{\partial n}\right]_\Gamma - \left[\frac{1}{\rho}\right]_\Gamma \dot{m}^2 \tag{26}$$

$$\vec{t}_l\left[2\mu\mathbb{D}\right]\cdot\vec{n} = 0; \quad i = 1,2. \tag{27}$$

where σ is the surface tension, κ is the local interface curvature, and $\dfrac{\partial\vec{u}_n}{\partial n}$, is the normal derivative of the normal component of velocity. The third term on the right hand side is the recoiling pressure occurring with phase change, the recoil pressure has been ignored in the numerical implementation as it has been found to be of small value. $\vec{t}_l\,(i = 1,2)$ represents the two tangential normals in 3D space.

- **Energy Conservation:** Finally, the following energy jump equation have to be added to the formulation:

$$[k\nabla T\cdot\vec{n}]_\Gamma = \dot{m}\left(h_{fg} + \left(C_{p,l} - C_{p,v}\right)\left(T_{sat} - T_\Gamma\right)\right) \tag{28}$$

where T_{sat} is the saturation temperature. Since it is assumed that $T_\Gamma = T_{sat}$,

$$[k\nabla T\cdot]\vec{n}]_\Gamma = \dot{m}h_{fg} \tag{29}$$

The multiphase flow solver solves the three-dimensional Navier-Stokes equations using the variable density pressure projection algorithm ([64]) on block structured

adaptive mesh refinement grid (AMR) ([65]). It can handle both compressible ([60]) and incompressible flows ([2], [66]). The solver employs the state of the art Moment of Fluid method (MoF) to represent multiphase interfaces ([67], [66], [60], [68], [69]). It employs dynamic contact models for droplet impact problems ([70]). Tests have showed that the code has a high parallel efficiency of more than 96% on a 48-core workstation.

Interface Representation

During the MOF interface reconstruction process, a reference volume fraction function F_{ref} and a reference centroid, X^c_{ref} both corresponding to the real interface, are given in Figure 6 (left), and the actual volume fraction function, F_A, and the actual centroid, X^c_{act} corresponding to the reconstructed interface, are then computed as shown in Figure 6 (right).

The MOF method requires that the actual volume fraction be equal to the reference value and the actual centroid be as close to the reference centroid as possible. This becomes a constraint optimization problem formulated as follows:

$$\text{Minimize} \quad \|\mathbf{X}^c_{ref} - \mathbf{X}^c_A(\mathbf{n}, b)\|^2, \quad \text{Under constraint:} \quad \|F_{ref} - F_A(\mathbf{n}, b)\| = 0$$

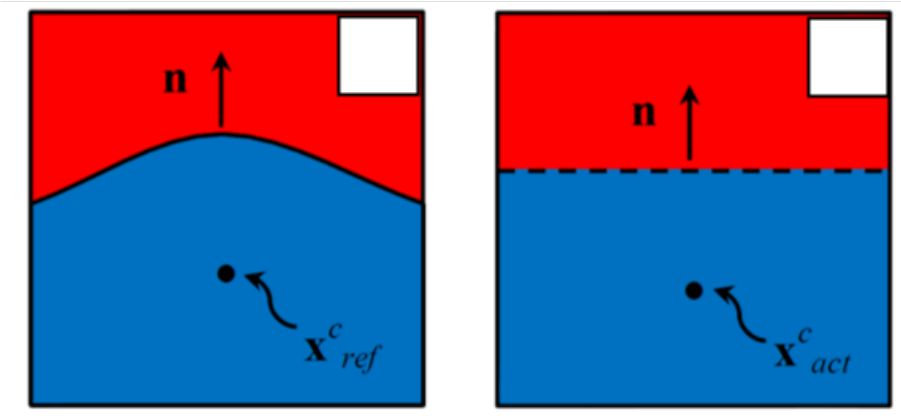

Figure 6. Surface reconstruction using the MOF method Li *et al.*(2013) [2] (left) the real interface and reference volume fraction and centroid; (right) the reconstructed interface and computed volume fraction and centroid.

As discussed in Jemison *et al.*(2013) [66], the use of centroid information ensures the MOF method maintains a sharp interface. In their simulations it was critical to maintain a sharp interface as they performed droplet impact simulations.

Phase Change Velocity

The contribution to the interface velocity due to phase change is divided into two parts:

- $V_{Ip} \rightarrow$ Velocity of material domain variation due to the phase change is evaluated by:

$$V_{Ip} = \frac{\dot{m}}{\rho_l} = \frac{[\kappa \nabla T] \cdot \vec{n}_{lv}}{\rho_l h_{fg}} \tag{30}$$

- $V_{Ie} \rightarrow$ Velocity due to gas expansion, is evaluated by:

$$V_{Ie} = \frac{V_{Ip}\left(\rho_l - \rho_v\right)}{\rho_v} \tag{31}$$

  Hence the volume and mass are preserved discretely with negligible error. In other words, from time T_0 to T_1:

$$\sum F_v^{i,j}\left(T_1\right)\rho_v V^{i,j} - \sum F_v^{i,j}\left(T_0\right)\rho_v V^{i,j} = \sum \left(-F_{liq}^{i,j}\left(T_1\right) + F_{liq}^{i,j}\left(T_0\right)\right)\rho_{liq} V^{i,j} \tag{32}$$

Next, the level-set functions and volume fractions are updated using the calculated phase change rates. The interface is perfectly sharp. This property is an extension to the work of Weymouth and Yue (2010) [71] to the phase problem. This property in the method addresses the over shoot and undershoot problem for material advection and volume conservation is maintained.

Section 2 reports results for validation of the MoF code. Comparison of results are provided with an analytical solution of vapor bubble growth in super heated liquid under absence of wall heat transfer.

2 Validation: Vapor bubble growth in super-heated liquid under absence of wall-heat transfer

Simulation of a growing vapor bubble in a super-heated liquid has been performed in r-z coordinate system. There is an analytical solution available for this problem in the literature, hence this provides a good basis for the code validation. The analytical solution was provided by Scriven (1959) [62]. In that paper, the author provided an equation which relates the bubble radius as a function of time for a specific super-heat.

Equation reported by Scriven [62] is:

$$R = 2 \cdot \beta_g \sqrt{\frac{k_l t}{c_{pl} \rho_l}} \tag{33}$$

where R is the radius of the bubble, t is the time, k_l is thermal conductivity of the liquid, and β_g is a growth constant which is determined by:

$$\frac{\rho_l c_{pl} \nabla T}{\rho_v \left(h_{fg} + \left(c_{pl} - c_{pv}\right) \nabla T\right)} = 2\beta_g^2 \int_0^1 \exp\left(\beta_g^2 \left(\left(1-\zeta\right)^{-2} - 2\left(1 - \frac{\rho_v}{\rho_l}\right)\zeta - 1\right)\right) d\zeta \tag{34}$$

where ρ_v, c_{pv} are the density and specific heat capacity of the vapor phase and h_{fg} is the latent heat of vaporization. ∇T is the super-heat (i.e. the difference between the saturation temperature of the liquid and the actual temperature of the liquid).

The simulations were run for three different super-heats and are compared with the analytical solution of Scriven. The system pressure is maintained to be constant at 1 atm. The initial bubble radius is 0.05 mm and the domain size in each direction is 0.1205 mm. The bubble radius is calculated in this case similar to Sato and Ničeno (2013) [3] using the equation (for 2-d case).

$$R = \frac{1}{2}\frac{D_x + D_y}{2} \tag{35}$$

where D_x, D_y are the bubble diameters in x and y directions respectively.

A grid convergence study is presented in figure 7 for the case of $\Delta T = 5K$. Here the domain is divided into 32 by 32, 64 by 64 and 96 by 96 points respectively in each

case. However, since the adaptive mesh refinement feature in the code has been used AMR = 1, this corresponds to a double value of the number of grid points in the multiphase regions. For the finest case of 96 by 96, the initial number of data points inside the bubble in each direction is about 80. From figure 7 it can be concluded that the 96 by 96 with amr=1 resolution has converged. Hence, this is the chosen resolution for the validation study.

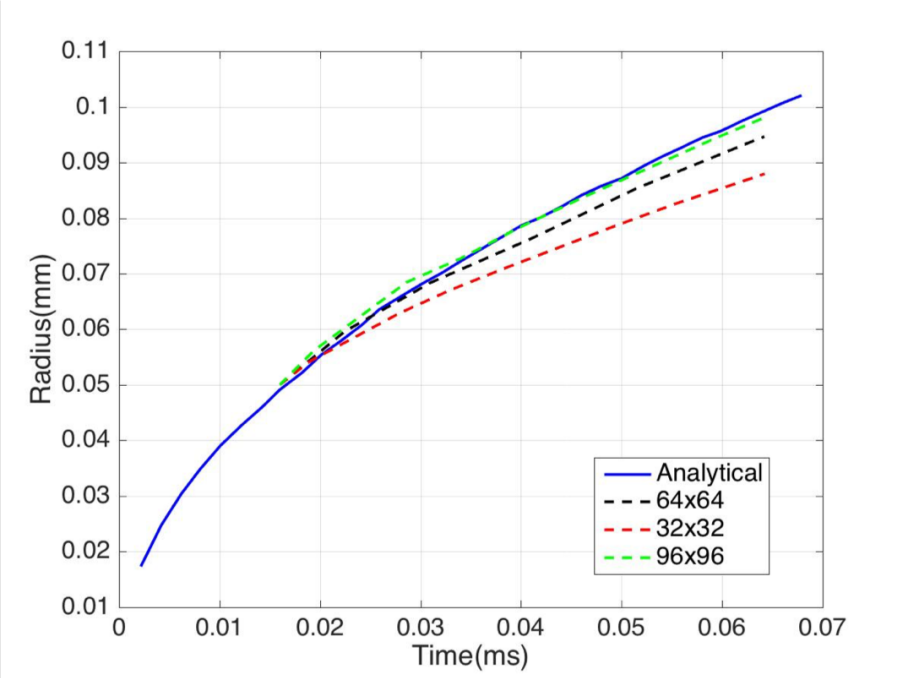

Figure 7. Resolution comparison: Growth rate at $\Delta T_w = 5K$

The rate of increase of the bubble radius provides good agreement with the analytical solution. It should be noted that the numerical simulation data points start from a radius of 0.05 mm, as that is the initial radius value used for the simulations. in figure 7. The comparison of the growth rates for different super-heats (5 K, 2.5 K and 1.25 K) with the respective analytical solutions are shown using a log-scale plot in Figure 8. The results are similar to that of Sato and Ničeno (2013) [3].

Table 3. MoF method percentage difference with Scriven equation

Superheat, ΔT	**Mean Error Percentage**
1.25K	2.97%
2.5K	3.41%
5.0K	1.06%

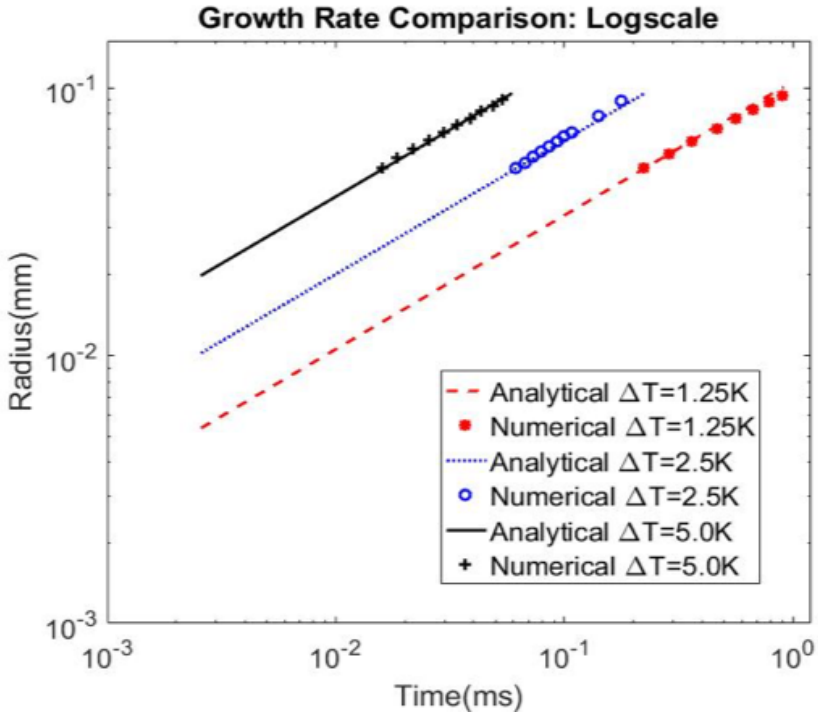

Figure 8. Growth rate comparison in log-scale

The mean percentage error for each superheat for the MoF predictions from the Scriven equation values are presented in table 3. The results show that error for all three superheats are lower than 4%.

Next, the velocity vectors for different super heats at the same time instant are plotted. Two counter-rotating vortical structures inside the vapor bubble could be observed, similar counter-rotating vortices were also reported by [3]. These vortical

structures are similar to the parasitic currents generated by the surface tension, which were also reported by [72].

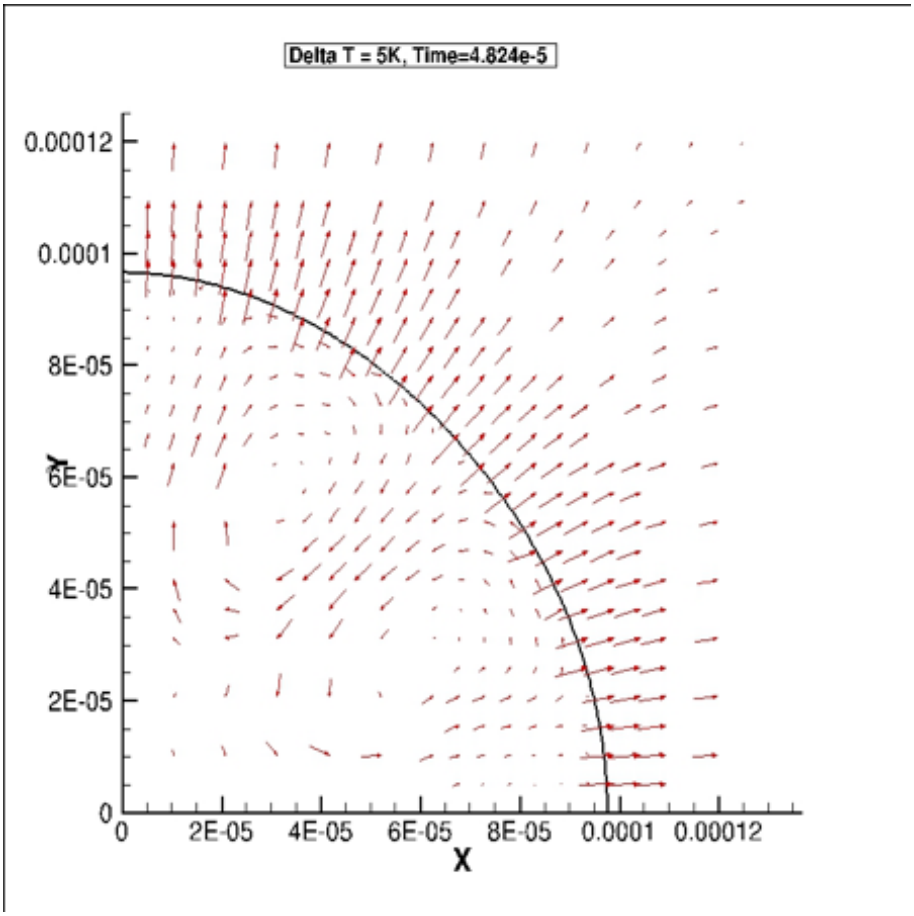

Figure 9. Velocity vector for super-heat=5k

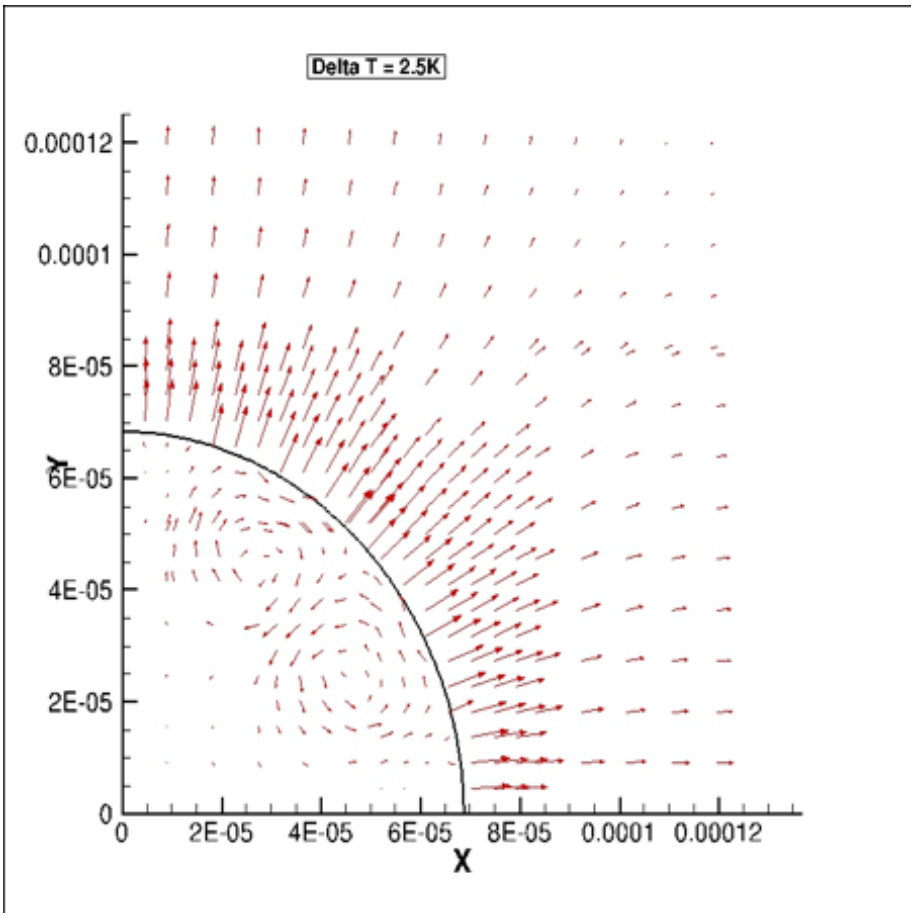

Figure 10. Velocity vector for super-heat=2.5k

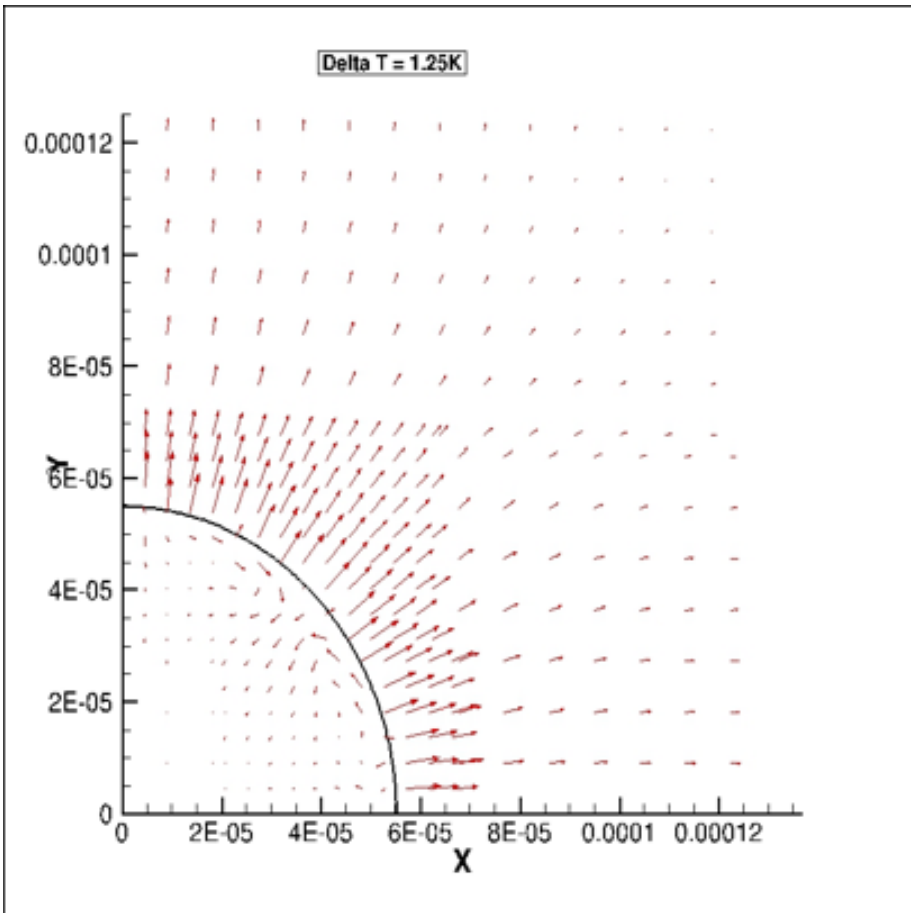

Figure 11. Velocity vector for super-heat=1.25k

Figure 9, Figure 10, and Figure 11 shows the velocity vectors for super-heats 5, 2.5, and 1.25K all three are at the same time instant of 4.824e-5 seconds.

Next, the boundary layer thickness at different super-heats is shown, at the time when the bubble radius is same for all three cases. It can be seen from figure 12 that the boundary layer thickness increases with decreasing super-heat which is also in agreement with the results from [3].

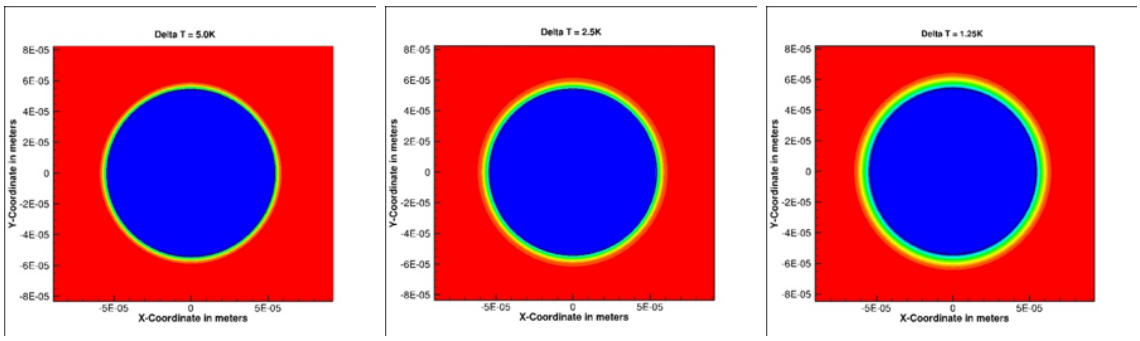

Figure 12. Boundary layer thickness for same radius (different times), super heat=5K, 2.5K, 1.25K (L-R)

However, they reported bulging at the ends of the boundary layer for lower super-heats, specifically for super-heat of 1.25K. In the MoF simulations, for the same radius plot (12), no bulging can be seen, and complete symmetry is maintained across the entire cross-section. However, in figure 13, which shows the results at the end time for the simulations, some bulging at the ends could be seen, but the bulging with the MoF method is much less pronounced than that of [3]. For reference and comparison of the degree of deformation in the temperature field, a snapshot of Figure number 24 on page 17 of Sato and Ničeno (2013) [3], is provided here (figure 14 in this thesis).

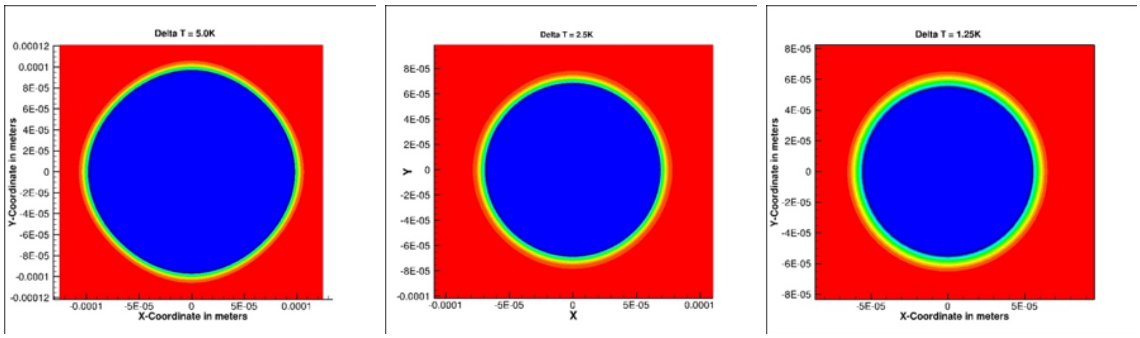

Figure 13. Boundary layer thickness for same time instant, super heat=5K, 2.5K, 1.25K (L-R)

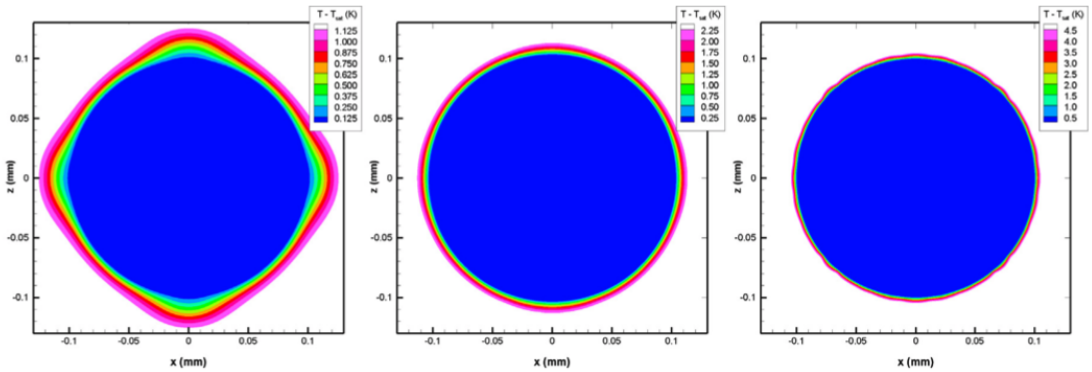

Figure 14. Boundary layer thickness from Sato and Ničeno (2013), super heat=1.25K, 2.5K, 5K (L-R), Image Source: [3]

This bulging of the temperature field (due to the thickening of the thermal layer) is believed to be caused by the artificial recirculating flow pattern with in the bubble.

CHAPTER III

NUCLEATE BOILING SIMULATIONS IN EARTH GRAVITY AND REDUCED GRAVITY CONDITIONS

Using the MoF method, the results of the numerical simulations of 2-d nucleated boiling of a single vapor bubble in earth gravity and reduced gravity are presented below.

1 Vapor bubble growth with heat transfer from the wall in earth gravity

Vapor bubble growth in presence of a wall heater is being considered under earth gravity. The wall is maintained at a constant temperature T_w. In this case as the heat transfer from the wall is considered and due to the presence of gravity, bubble departure is expected. Urbano *et al.* [73] and Guion *et al.* [74] showed the significance of a microlayer and provided a figure to determine the cases for which the microlayer contribution would be significant. They showed in figure 9a of their paper that whether the case falls in the microlayer regime (i.e. a microlayer is formed and hence contributes to bubble growth) or Contact Line regime depends on a combination of Jakob number $\left(\text{Ja} = \dfrac{\rho_l c_{pl}(T_w - T_s)}{\rho_v L_{vap}}\right)$, (where ρ corresponds to the density, c_p corresponds to the specific heat, T corresponds to temperature, and L_{vap} is the latent heat of vaporization, subscripts l, v, w, s corresponds to liquid, vapor, wall, and saturation), and Contact Angle. The figure 9a in Urbano *et al.*, shows that our simulation case (with Ja=21.03 and Contact Angle =50 degrees) falls under the Contact Line regime, hence no microlayer consideration is required. This is further verified with good agreement between the MoF simulations with the experiments. Similar results

were also reported by Tryggvason and Lu [75], who did not consider the microlayer contribution as well. For cases with higher Ja and Contact Angle, some form of microlayer modeling approach can be implemented as an extension to the MoF method. The results reported are a comparison with experimental results reported by Dhir [4]. In that paper, the authors provide numerical simulation as well as experimental results. The test liquid used is saturated water, with a wall superheat of $\Delta T_w = 7K$ and static contact angle of $\theta = 50^{\circ}$. Domain size of 64 by 128 was used, with AMR = 1, which makes the effective grid size to be 128 by 256 points. We simulate half of the bubble and use symmetric boundary conditions. Thus for the initial bubble size of diameter = 0.00075m, the number of grid points inside the bubble along the diameter is $\sim$ 26. Figure 15 shows the snapshot of the bubble growth life-cycle at different time instants. Figure 15 shows the snapshot of the bubble growth life-cycle at different time instants.

Figure 15 shows the snapshot of the bubble growth life-cycle at different time instants. Dhir [4] did not provide bubble shape for the case of $\Delta T = 7K$, so we compare the bubble shape at departure with Dhir [4] results for the case of $\Delta T = 8.5K$ in figure 16. Results in figure 16, show that the MoF method provides reasonably good prediction for bubble shape at departure in comparison to experiments. A comparison plot of the MoF method is presented with both the numerical result as well as experimental result of Dhir [4] for the bubble growth rate indicating the departure diameter and the departure time in figure 17. It should be noted that in this case, as per Dhir [4], the diameter is calculated as equivalent bubble diameter for an equal volume sphere. Figure 17 shows the comparison of departure diameter and departure time. In their paper, Dhir (2001) [4] reported that their numerical simulations overpredicted the departure time and the departure diameter. For departure diameter, the percent difference between MoF simulation and experimental case is 1.12%, Dhir [4] is at 0.54%. But, the percentage difference of departure time between MoF simulation

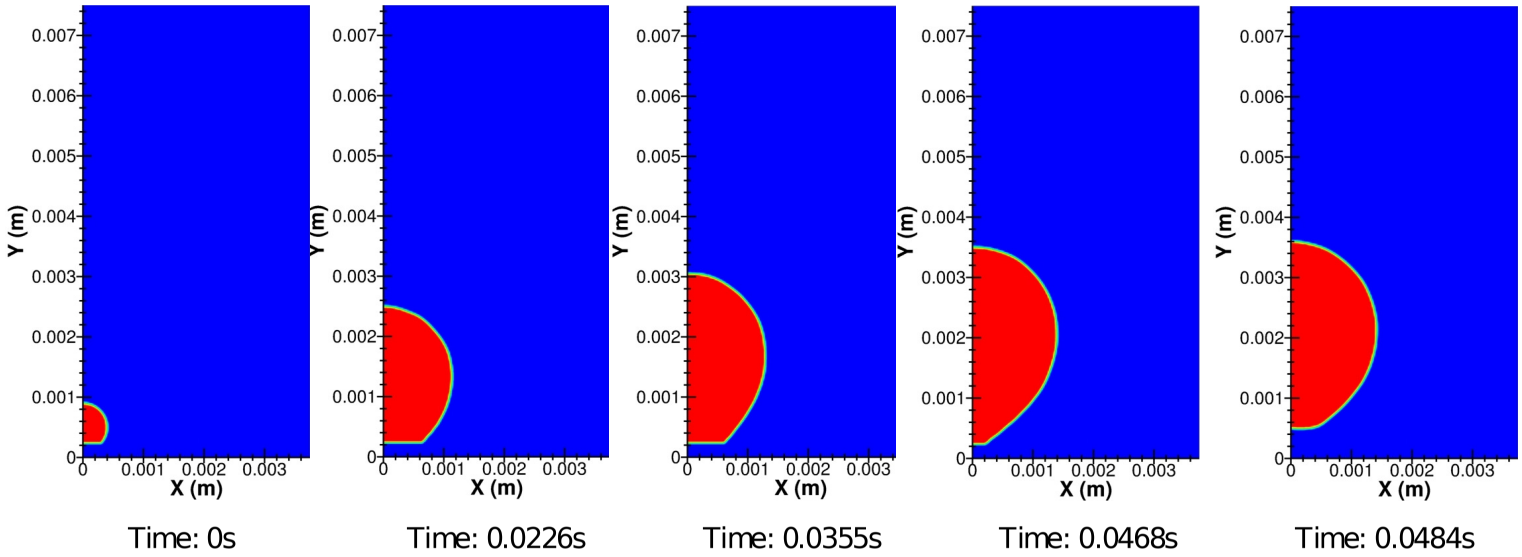

Figure 15. Snapshots of bubble growth and departure in earth gravity

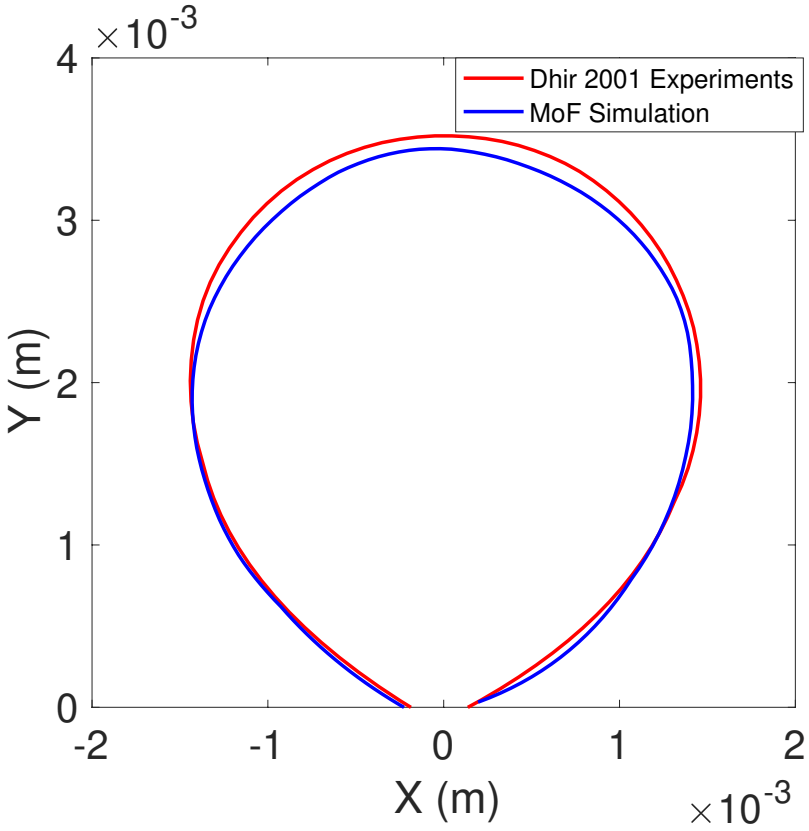

Figure 16. Bubble shape at departure comparison between MoF and Dhir [4] for $\Delta T = 8.5K$

with experimental result is 16.72% which is more accurate than that of Dhir [4] at 21.43%. Since the bubble in the MoF results has an initial radius, the data has been shifted such that in all the cases in figure 17, the vapor bubbles are at the same initial radius at the initial time to maintain consistency and accuracy between previously published and current results.

Dynamic contact angle has been used in the studies by Ajaev *et al.* [76], Mukherjee *et al.* [77], Jo *et al.* [78] among others. Ajaev *et al.* [76], explores dynamic contact angle for evaporating liquids on inclined surfaces, not nucleate boiling. However, the study by Mukherjee *et al.* [77] explores the effect of static contact angle, and different cases of dynamic contact angles on single bubble nucleate boiling. They conclude that the vapor-removal rate shows very little change for three following cases: static contact

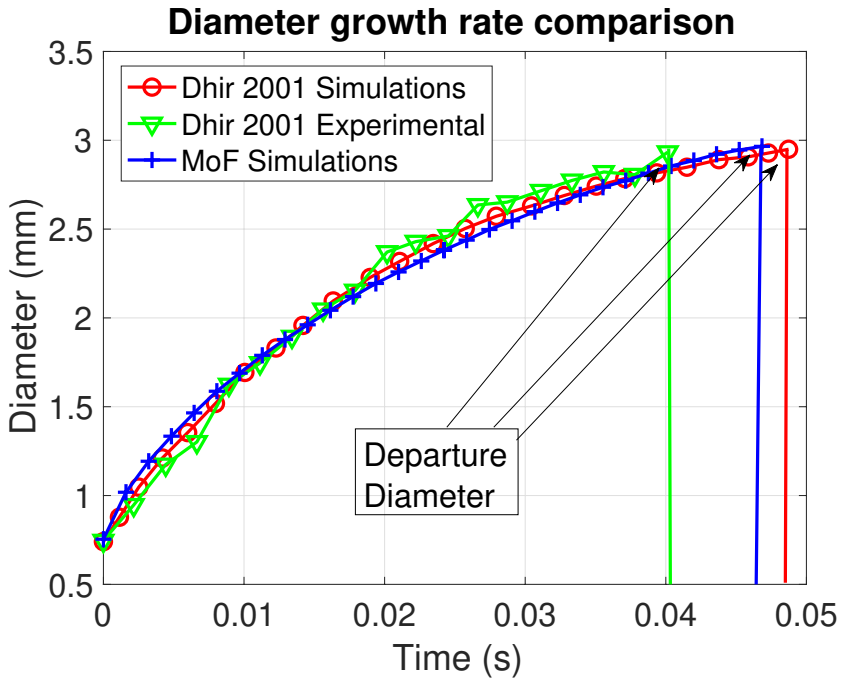

Figure 17. Bubble growth rate comparison under earth gravity conditions

angle (Case 1), dynamic contact angle with constant value advancing and receding angle (Case 2) , and dynamic contact angle as a function of interfacial velocity (Case 3).

We compare two different modeling techniques for the dynamic contact angle. We use the Jiang [79], and Kistler [80] models of dynamic contact angle formulation. The Jiang model calculates the dynamic contact angle ,θ_d, using

$$\frac{\cos\theta_s - \cos\theta_d}{\cos\theta_s + 1} = \tanh(4.96\mathrm{Ca}^{0.702}) \tag{36}$$

where θ_s is the static contact angle, Ca (Capillary number) is given as: $\mathrm{Ca} = \dfrac{\mu V_{cl}}{\sigma}$, where μ is the dynamic viscosity of the liquid, V_{cl} is the contact line velocity, and σ is the surface tension. One drawback of the Jiang model is that it is not as accurate for large values of Ca [81]. However, since Ca values are significantly small in our simulations, that drawback is not applicable. Using the the Jiang model, we found the maximum range of the Dynamic Contact Angle to be about 2°, which shows that the

effect of the dynamic contact angle in this case is negligible. The results for growth rate for nucleate boiling in earth gravity using these two models in comparison to the static contact angle model, and experimental results from Dhir [4] are reported in figure 18.

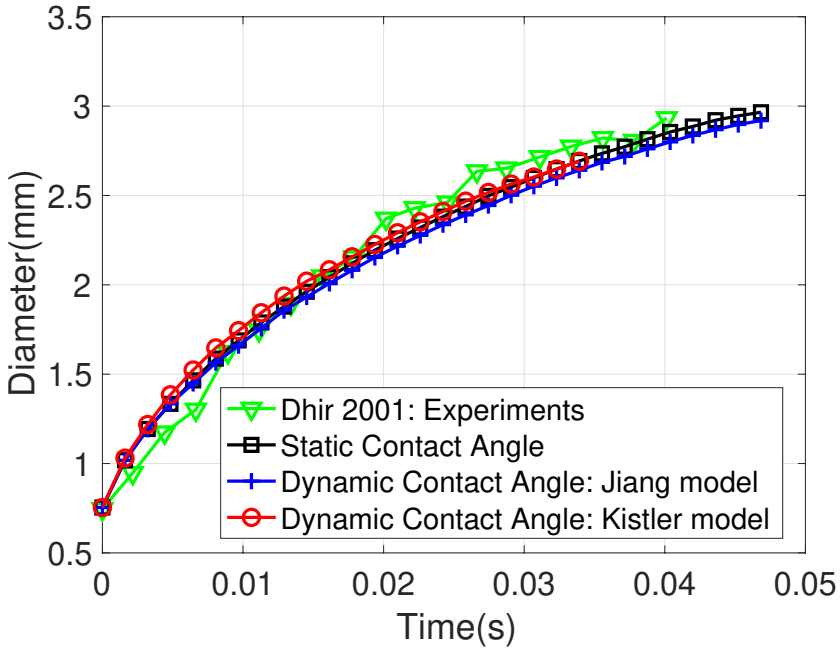

Figure 18. Growth rate comparison for different contact angle models

The results in figure 18, shows that the departure time and diameter for the Kistler model is under-predicted (which can be seen from where the curve for each case ends), where as for the Jiang model, it is similar to the static contact angle model for the earth gravity case. The growth rate, however, is almost similar for both Jiang and Kistler models in comparison to the static contact angle model. These results are in agreement with the conclusions of Mukherjee *et al.*, that the vapor removal rate sees very little change. Hence, for the results reported in this dissertation, a static contact angle model has been used.

Next, a plot of the heat transfer rate as a function of time is reported in figure 19. Here the heat transfer is calculated as the heat energy per unit time required to

vaporize the volume of liquid corresponding to bubble growth in that time. Since it considers the total heat supplied to the bubble, it takes into account both the heat transfer from the wall and the heat transfer from the surrounding liquid.

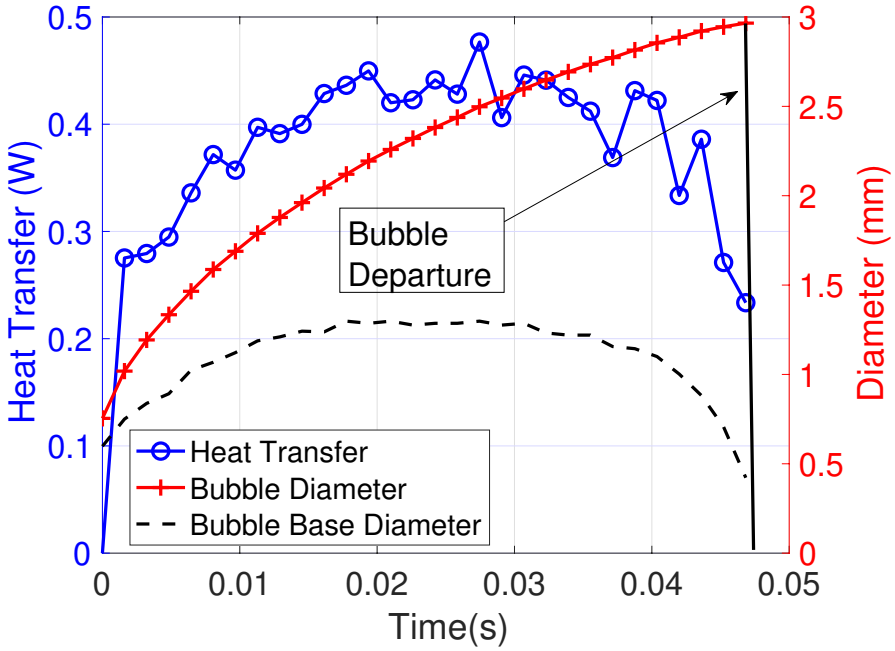

Figure 19. Heat Transfer as a function of time in earth gravity

The bubble growth rate is also plotted on the right Y-axis of figure 19. A peak could be observed in the heat transfer rate at a later stage of the bubble life-cycle. During the departure phase, the bubble base starts to shrink, which means increased quantity of colder water surrounds the bubble, this makes the vapor bubble lose some of its heat by conduction to the colder water, i.e. conduction of heat from the vapor bubble is increased, hence more heat is transferred to the bubble. The peak signifies this additional heat transfer. Finally, there is a drop in the heat transfer rate, as the bubble enters departure phase, this is evident from the shrinking size of the bubble base diameter from about 0.03s mark to the ultimate lift-off. Heat transfer rate continues to drop till the bubble lifts off and departs indicated by the vertical line, which is in agreement to the reasoning provided above.

Vapor bubble growth with heat transfer from the wall in reduced gravity

In the case of reduced gravity, a comparison of the MoF simulations are presented in comparison with results from experiments by Siegel and Keshock [5]. In this paper, the authors provide experimental results for reduced gravity cases which were performed using a drop tower. The results are for a case with wall superheat of $\Delta T_w = 11.1K$, and $g_z = 1.4\% g_e$, where g_z corresponds to the effective gravity value and g_e corresponds to the value of gravity at earth. The simulations were carried out using a grid resolution of 128 by 256 and amr = 1. which makes the effective grid size to be 256 by 512 in the X-direction and Y-directions respectively. The initial number of grid points inside the bubble along the diameter is 26, as only half the bubble is simulated due to symmetric boundary conditions. The bubble shape at different time instants are shown in figure 20. With reduced gravity environment, the bubble did not observe departure similar to that in the experiments.

Figure 21 shows the bubble growth rate comparison of numerical results of MoF method with experimental results of Siegel and Keshock [5]. The growth rate results provided by the MoF simulation is in good agreement with the experimental results. Next, the heat transfer as a function of time is provided for the reduced gravity case in figure 22.

Heat transfer in the reduced gravity case does not observe the drop in comparison to the earth gravity case, as the bubble does not enter the departure phase in this case. The growth rate is also plotted along the right y-axis for reference.

Vapor bubble growth in micro-gravity conditions

MoF simulation of boiling in micro-gravity conditions is compared with experiments on the International Space Station (ISS) by Dhir *et al.* [7]. For the experiments, the wall superheat was in a range of $4^\circ - 7^\circ$C and the liquid sub-cooling varied from $5^\circ - 1^\circ$C due to variance in pressure. For the comparison of the numerical

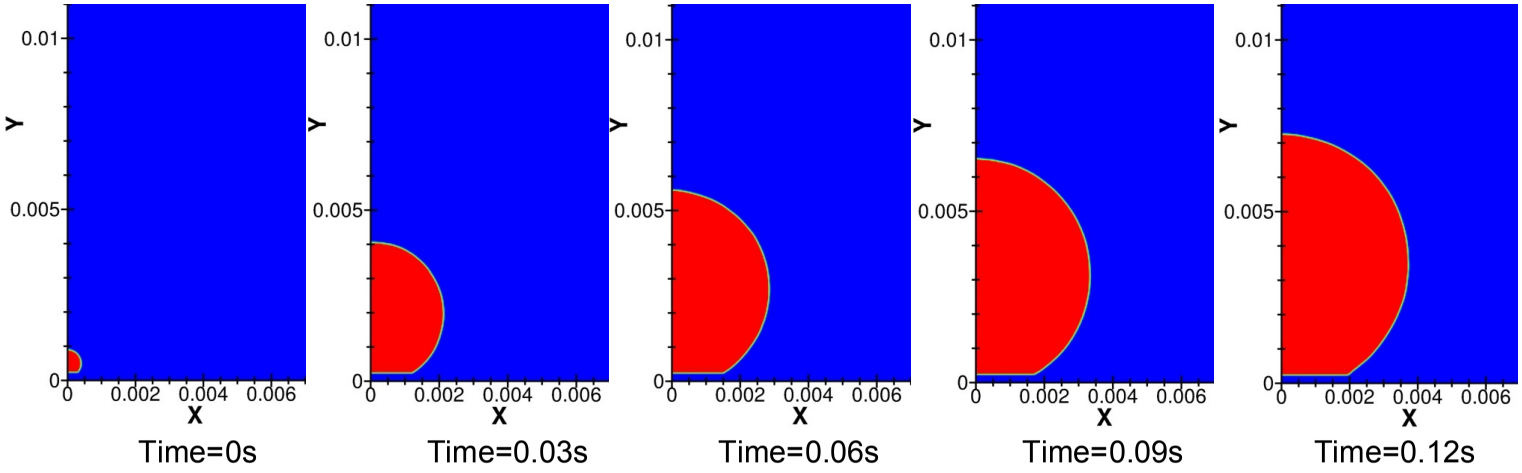

Figure 20. Snapshots of bubble growth in reduced gravity

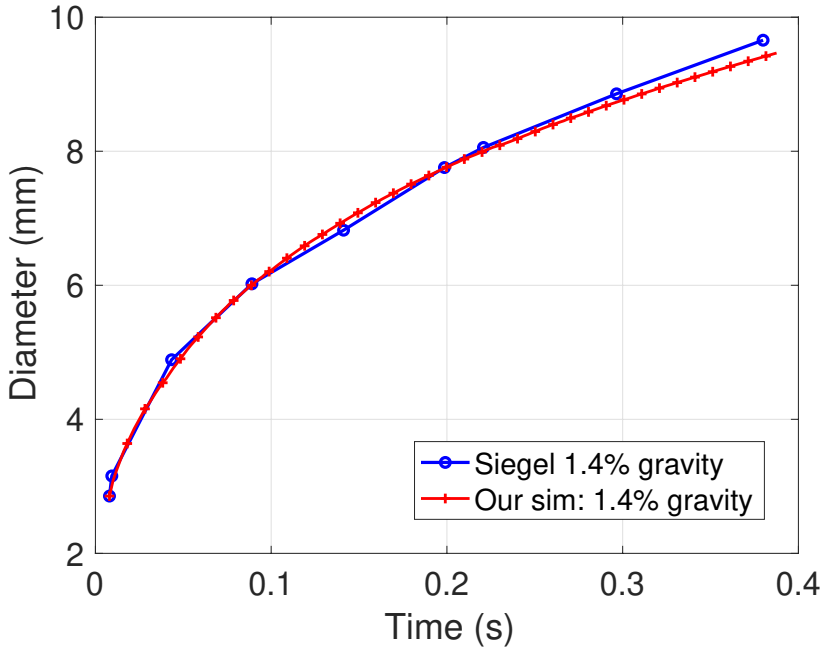

Figure 21. Bubble growth rate comparison of numerical results of MoF method with experimental results under reduced gravity conditions ($g_z = 1.4\% g_e$)

simulation using MoF method with the micro-gravity simulations, we use a saturated liquid (i.e. no sub-cooling). Dhir *et al.* [7] reported multiple challenges with their experiments on ISS, one of the key challenges being a heater malfunction, which resulted in the system pressure to vary and this resulted in an increase in the liquid saturation temperature. As a consequence of this increase in the liquid saturation temperature, the liquid subcooling got introduced. Dhir *et al.*then increased the wall temperature to compensate for the increase in liquid subcooling. However, in our simulations the system pressure, liquid saturation temperature, and wall temperature were maintained to be constant through-out the simulation. Hence, there was no need for sub-cooling or increasing wall temperature in the MoF simulations. The wall superheat for our simulations is set to be constant at 16°C. The MoF simulation is run for a domain of 32mm by 32mm with a base resolution of 144x144 and a refinement setting of 2. As mentioned earlier, a refinement value of 2 corresponds to a resolution

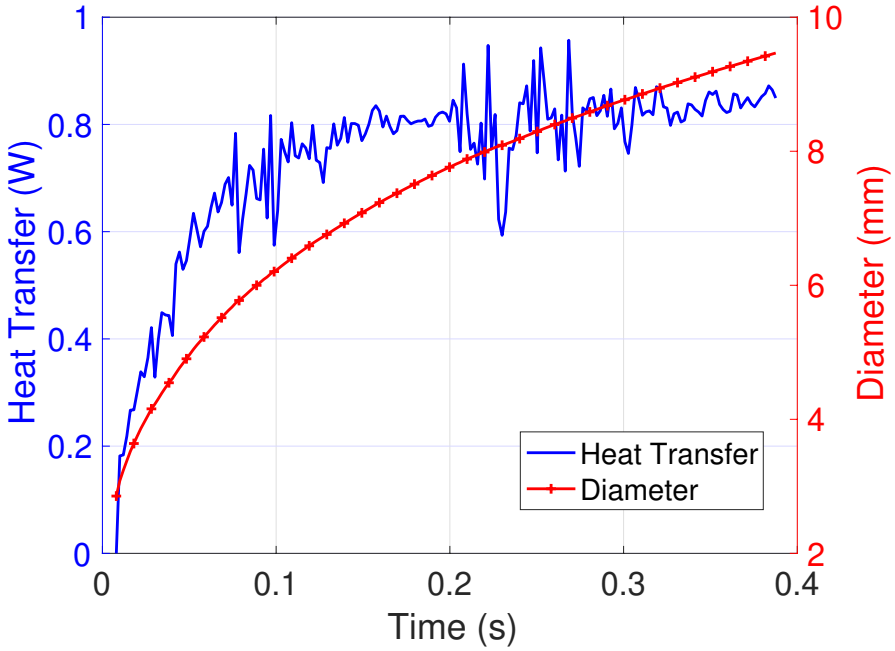

Figure 22. Heat transfer as a function of time for reduced gravity case

of 576 by 576. This results in about 110 initial grid points inside the bubble in along the diameter. For our results we performed the simulations for about 5 seconds of total run time, where in the bubble diameter reached a size of about 20mm. For the micro gravity case, since the bubble size is larger, the domain is also larger, making the required resolution to be very fine. This makes the simulation computationally very expensive and time consuming. The reason for that is the time-step size is very small due to the stability time constraint for surface tension. The stability time constraint due to surface tension $t_{surf} \propto (\Delta x)^{3/2}$. Since Δx is very small, t_{surf} is also very small, which requires a large number of time-steps to reach a significant total simulation time value. Figure 23 shows a comparison of the experimental results with the MoF simulations for the same test liquid (perfluoro-n-hexane) in micro-gravity conditions.

The results from the MoF simulation are in good overall agreement with the experimental ones. As in the experiments, the simulations also did not observe bubble

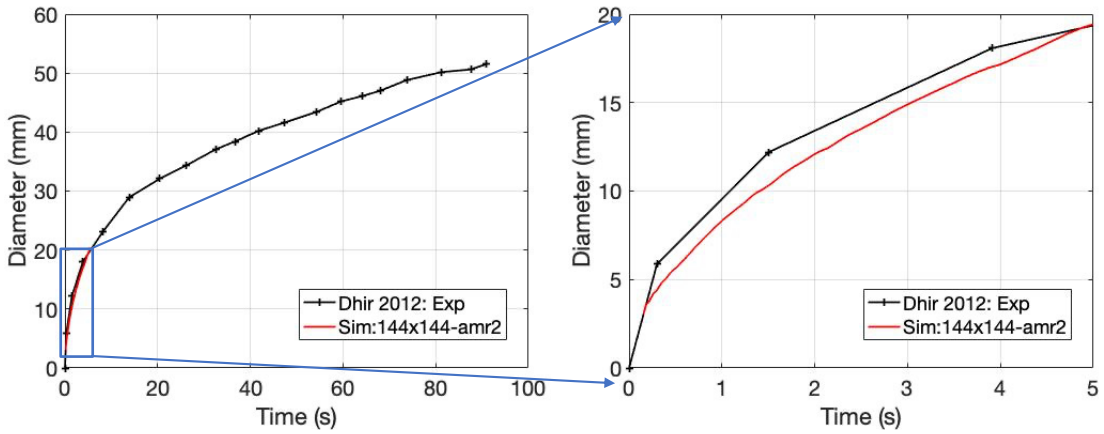

Figure 23. Bubble growth rate comparison of numerical results of MoF method for micro-gravity conditions with experiments on ISS

departure in the micro-gravity environment. A zoomed in plot for the portion of the run time of the simulation is added on the right side of figure 23. In order to provide a qualitative understanding of the above simulation under micro-gravity, the heat transfer rate is also plotted in figure 23 as a function of time. In figure 24, the

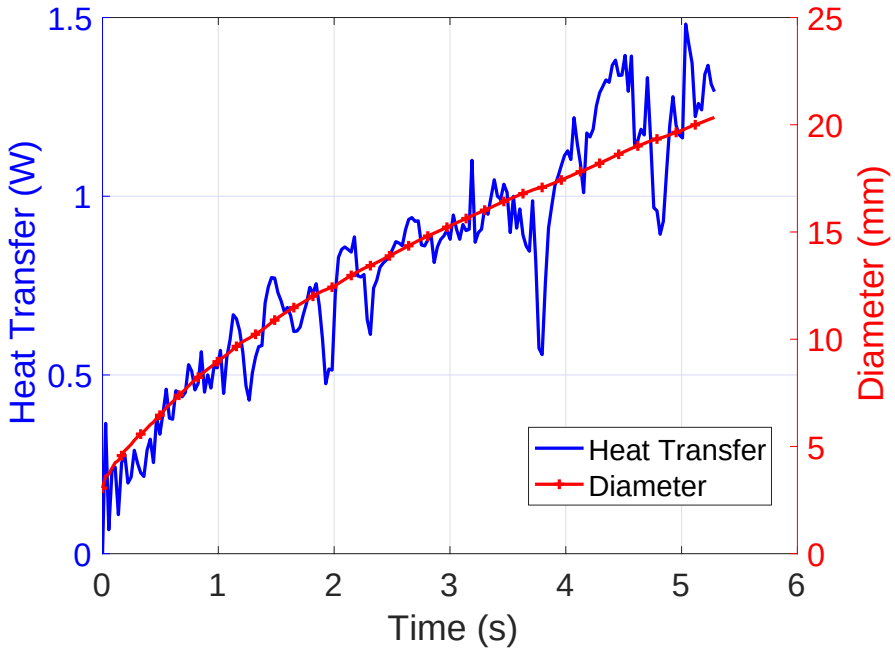

Figure 24. Heat Transfer as a function of time for micro-gravity simulations

growth rate is also plotted on right y-axis for reference. The slight difference in the growth rate of the simulations in comparison to the experiments could be attributed to the uncertainties in the experiment itself which are mentioned in details in their paper. Moreover, only one experiment for single bubble case was completed in the experiments, which makes the statistical uncertainty considerably high.

Based on the heat transfer plots provided for each gravity case, it can be seen that for the same amount of heat transfer of 0.5W, the bubble diameter is different. For earth gravity with water, the diameter at 0.5W of heat transfer is about 2.5mm, the same for water in reduced gravity is 6mm, and the same for Pfnh in micro-gravity in 8.3mm. From the results it can be concluded that as gravity is reduced, less heat transfer is required to reach the same bubble diameter.

More significantly, the results show that for the experiments, the wall super-heat was 7°C, but for the simulations a wall-super heat of 16°C was required. The reason for this could be attributed to the absence of the micro-layer contribution in the simulations. This shows the importance of micro-layer evaporation specifically in micro-gravity conditions. A novel approach for calculating the contribution from the depletable micro-layer in micro-gravity condition is proposed in Chapter IV.

In section 2 we propose a new method to determine the bubble diameter at any gravity level using a non-dimensional equation model.

2 New method for determining bubble diameter at different gravity levels

So far, bubble growth and departure results for cases at different gravity levels have been reported. A closer analysis of the results shows that there is a similar pattern to the growth rate curves of the bubbles at each gravity level. The growth rate changes with gravity. For this case, we use the experimental results at reduced gravity by Siegel and Keshock [5]. In their paper, they used a drop tower to control the value of the gravity. We use their results for three different gravity values of 1.4%, 3.0%,

and 6.1% of earth gravity. This has been shown in figure 25.

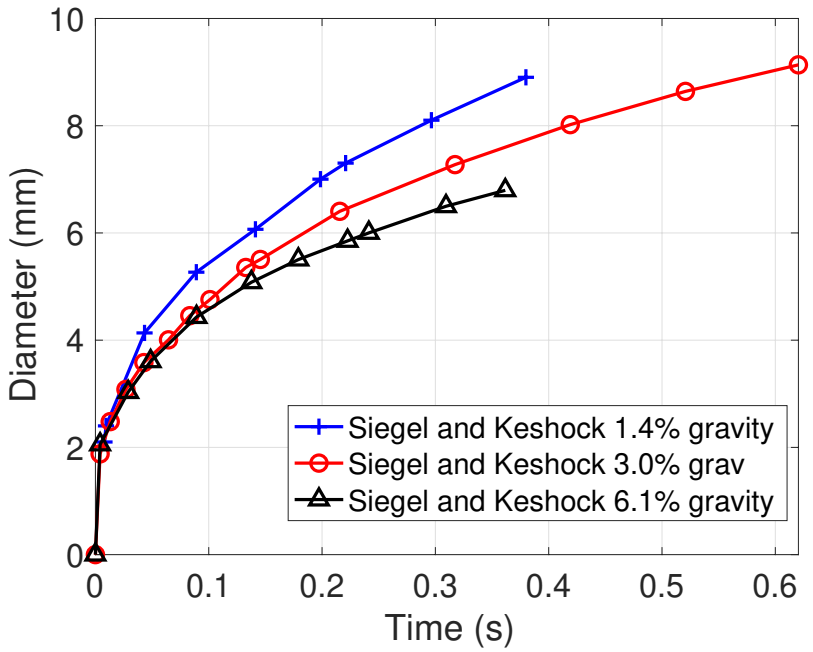

Figure 25. Bubble growth rate in different gravity values (experimental data from [5])

The goal is to develop a method by obtaining a generalized growth curve irrespective of the gravity level. Keeping all other parameters constant, if we change only the value of gravity, the growth rate of the bubble changes and this change can be attributed to the change in gravity value only. For these cases, we use the experimental data for growth rates for experiments at different gravity levels and we perform an analysis by starting with making the relevant values dimensionless. Next, we use a power-series curve fitting where we try to "fit" the growth rate curves at different gravity values into a single curve and generate a common equation which would be a close match for the data of all the gravity levels. We propose the generalized equation to be:

$$d^* = \frac{D}{(g^*)^C \times D_e} \tag{37}$$

$$g^* = \frac{g}{g_e} \tag{38}$$

$$t^* = \frac{T}{T_e} \tag{39}$$

where d^* is the non-dimensional diameter, D is the diameter of the bubble at any time instant, g^* is the non-dimensional gravity, g is the gravity value in question and g_e is the earth gravity value. C is the coefficient for the specific case and D_e is the departure diameter at earth gravity. t^* is the non-dimensional time, where T is the time instant of the simulation or the experiment and T_e is the departure time at earth gravity. It should be noted that T_e and D_e could be any value for time and length respectively. Both T_e and D_e are used as constant values and their significance lies only in non-dimensionalization of the time and diameter.

We start by choosing one time instant from figure 25, available in Supplemental Material, part of the ASME Digital Collection for all three gravity values. In this case we chose $t = 0.3003s$. Next we plot the diameters at this time-instant for all three gravity values and perform a curve fitting, as shown in figure 26.

Based on the curve fitting equation, we can generate the model equations which is shown above. Using the model equations, we plot the growth rates at three different gravity level in figure 27, available in Supplemental Material, part of the ASME Digital Collection. It should be noted that the values of the coefficients of the equation are specifically for the case of Siegel and Keshock [5]. Only data from Seigel and Keshock is used since this is the only paper which provides experimental results at different gravity levels, by keeping all other parameters constant. Since the proposed equation is mainly dependent on gravity, it is imperative to keep other variables such as wall superheat, system pressure, etc. constant. The test liquid (water in this case) parameters, the superheat value and all other parameters that contribute to

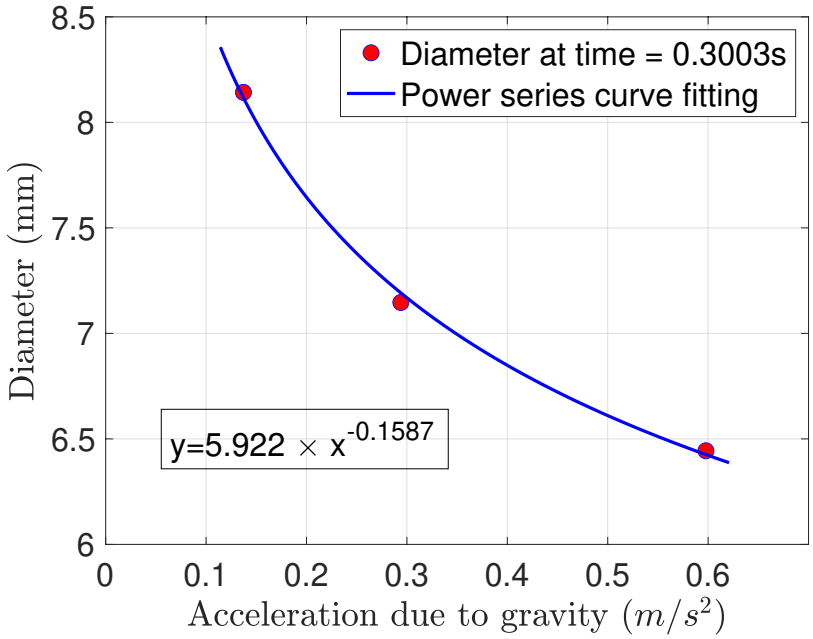

Figure 26. Curve fit for diameter at same time instant for different gravity levels

the growth of a bubble also contribute towards the calculation of the coefficients. The coefficient C for this case was calculated to be $C = -0.1587$.

The somewhat combined general curve shown in figure 27, can then predict the effective diameter of a bubble if the time instant and the gravity value is known. We validate this claim by calculating the d^* from the 3.0% gravity value, and then plug in the d^* to predict the diameters at 1.4% and 6.1% gravity values at those time instants. This is compared with the experimental results in figure 28.

It shows that the model is accurate at gravity levels for both higher and lower values than the one which was used to calculate d^*. Additionally, although the diameter from only one time-instant was used for performing the curve fit to generate the coefficient, the model predicts accurate results for all time-instants.

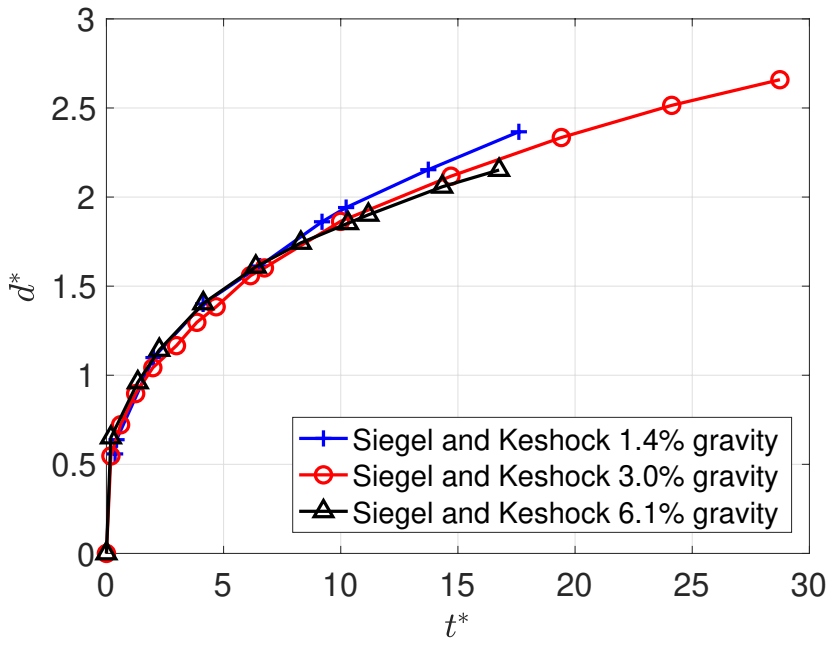

Figure 27. Generalized growth rate curve for different gravity levels

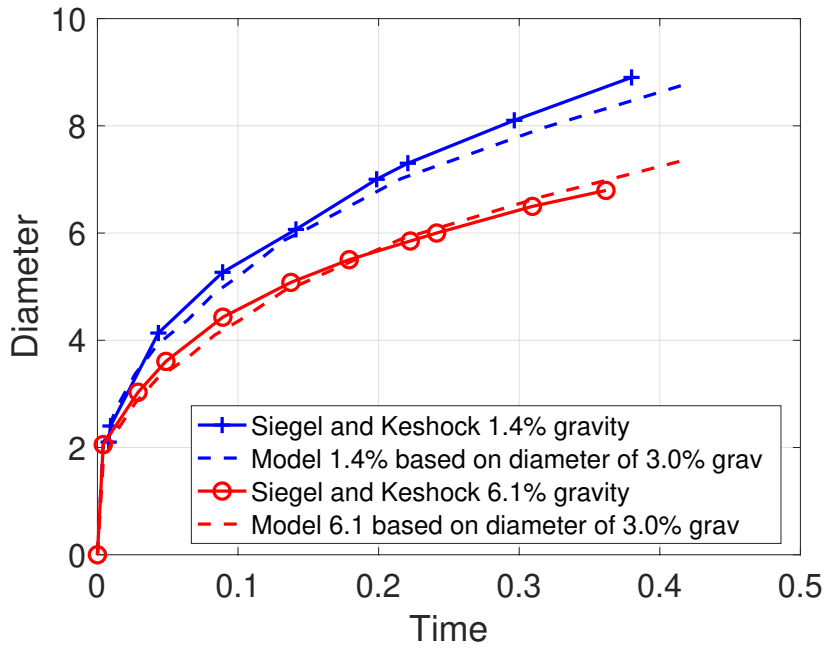

Figure 28. Comparison of model prediction with experimental results

CHAPTER IV

SIMULATIONS IN MICRO-GRAVITY CONDITIONS USING A NOVEL MICRO-LAYER APPROACH

The results for micro-gravity in Chapter III showed the importance of micro-layer contribution specifically for micro-gravity cases. In this chapter, we propose a novel approach to calculate the contribution of the depletable micro-layer in micro-gravity conditions [82].

1 Existing Micro-layer models

This section provides background on existing micro-layer models available in the literature. As introduced in Chapter I, a micro-layer is formed during the initial phase of the bubble life cycle. As the growth rate is much faster during this period, the speed of the interface growth is faster than the speed of the bubble base growth as the surface tension force in the bubble base hinders it growth to some extent. In order to compensate for the slower speed of the bubble base, the vapor-liquid interface of the bubble bends near the end and traps a thin later of liquid between the vapor bubble and the solid heater wall. This thin liquid layer has a thickness on the order of μm, hence the name micro-layer. Snyder and Edwards [43] first proposed the existence of a liquid micro-layer. Cooper and Lloyd [44] confirmed its existence with validation from experimental results. The typical life-cycle of the liquid micro-layer is that it forms during the initial phase of the bubble growth, then the micro-layer grows as the bubble grows while it continues to contribute to the bubble growth through the its evaporation. As the bubble enters the departure phase, the micro-layer reduces

in size and finally gets completely depleted before the bubble departs. In numerical simulations, the micro-layer is particularly challenging as the size of the micro-layer demands a small cell size where as the bubble size is typically on the order of a few mms. This makes the simulations computationally very expensive if the micro-layer needs to be resolved. Typically some form of modeling technique has been used in the community, some major modeling techniques along with their advantages and limitations are described below.

Triple line models or Contact line models

Wayner [54] proposed a model to consider the micro-layer contribution which was later adopted by Son *et al.* [6]. The contact line model (also known as a triple line model in the literature) proposed by them addresses the line where the curved surface of the bubble intersects the heated surface. They divided the domain into macro and micro-region, where the micro-region consisted of the micro-layer area, and macro-layer consisted of the remaining portion of the domain. A snapshot of the model from [6] is provided in figure 29.

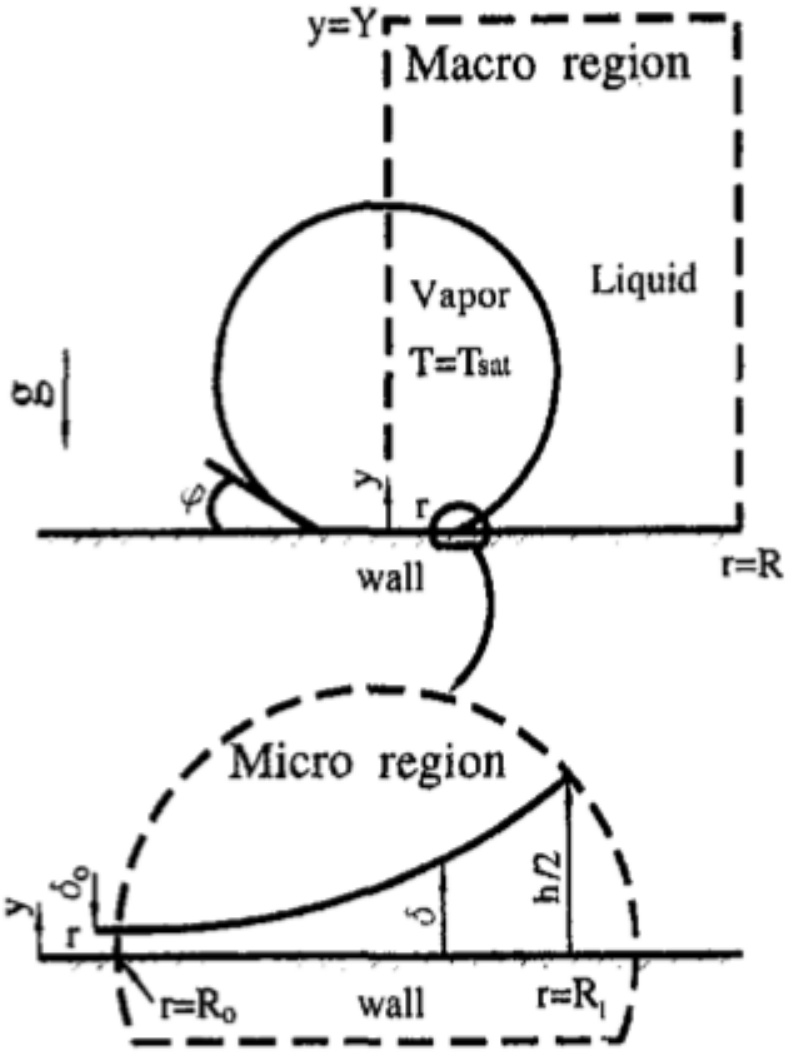

Figure 29. Microlayer in Triple Line Model from Son *et al.*, Img Source: [6]

They solved the mass, momentum and energy conservation equations in both the regions. For the micro-layer, they approximated the momentum conservation equation by using lubrication theory, so for the micro-layer, the momentum conservation equation for them becomes:

$$\frac{\partial p_l}{\partial r} = \mu_l \frac{\partial^2 u_l}{\partial y^2} \tag{40}$$

The fluid flow into the micro-layer is driven by the pressure difference, which is

calculated as:

$$p_l = p_v - \sigma\kappa - \frac{A}{\delta^3} + \frac{q^2}{\rho_v h_{fg}^2} \tag{41}$$

where p_l, p_v are the pressures associated with the liquid and vapor phases respectively. σ is the surface tension which is taken as a function of temperature, κ is the curvature. A is the dispersion constant which is an empirical term and evaporation heat-flux, q is approximated using the Clausius-Clapeyron equation:

$$q = h_{ev}\left[T_{int} - T_v + \frac{(p_l - p_v)T_v}{\rho_l h_{fg}}\right] \tag{42}$$

Using the conservation equations, a fourth order, non-linear differential equation is formulated.

$$\partial'''' = f(\partial, \partial', \partial'', \partial''') \tag{43}$$

This differential equation is solved to get the thickness of the micro-layer using boundary conditions. The liquid flow into the micro-layer is considered to be driven by the pressure difference between the liquid pressure and vapor pressure. Although, this micro-layer modeling approach was in agreement with experiments, some of the assumptions made in the model description do not reflect the actual physics of the process. The micro-layer length is considered for a small portion under the vapor bubble, this assumption is not true as experiments have shown that the micro-layer is formed along almost the entire length of the bubble base, barring a very small dry-out radius. So, the contribution of the micro-layer along the entire radial extent is not considered. Moreover, the micro-layer thickness is supposed to vary as the bubble life cycle proceeds and eventually deplete itself by evaporation, however this model assumes the micro-layer to be of a constant thickness and does not take into consideration the depletion too. From the numerical perspective, this model imposes a requirement that the micro-layer thickness needs to be about a cell size, which is also going to make it computationally expensive specifically for a case with thin micro-layer.

Depletable whole micro-layer models

Whole micro-layer models typically consider the micro-layer length to be along the entire radial extent of the bubble. Models which add the evaporation term in determining the micro-layer thickness so that the micro-layer would evaporate away or deplete away are called depletable models. Both of these are consistent with the actual physics behind the process confirmed by experimental results. Sato and Ničeno [56] proposed the first depletable micro-layer model. They simulated the growth and departure for a single vapor bubble from a heated surface using a sub-grid scale modeling approach for the micro-layer. The model uses the equation below to predict the micro-layer thickness:

$$\delta = C_{slope} R \tag{44}$$

where δ is the micro-layer thickness, and R is the radius of the bubble base. C_{slope} is a constant value which is estimated from the empirical coefficient shown in equation 7 from [50]. It should be noted that the value for C_{slope} used in the simulations, is just the initial value. They run the simulation with the initial value, compare to the experimental results, and based on the agreement with the results they modify the value used in the model. But this coefficient is specific to the test liquid water, and is also specific to the conditions of the experiment (for example the wall super heat). Due to these limitations, the model cannot be scaled to other liquids, and specifically to micro-gravity conditions as the test liquid typically used under micro-gravity is perfluoro-n-hexane instead of water. The coefficient for perfluoro-n-hexane is not yet known. From the numerical perspective, the model needs an additional sub-grid scale modeling technique which needs to be implemented by using a finite volume description for the micro-layer. Later Hänsch *et al.* [57, 58], proposed a modification to the model, by replacing the C_{slope} term in the expression for the initial micro-layer thickness by performing a back calculation from the rate of micro-layer depletion and the thickness of the depleted micro-layer to generate the initial micro-layer thickness.

But the depleted micro-layer value is generated from experiments too, which is in turn dependent on the test liquid of water, and the same disadvantages of the method to be not applicable for micro-gravity experiments with perfluoro-n-hexane persists with this model too. Additionally, Hänsch *et al.* [57,58] model requires very fine resolution. They report that at the liquid-solid interface the grid size is $0.5\mu m$, and time-step size of $2ns$ was needed. Such fine resolution and small time-step size, would make the computation very expensive which is sort of antithetical to the use of a modeling approach itself. Also, under earth gravity the bubble growth rate is found to be $t^{1/2}$ where, t is the time, but in micro-gravity conditions, the bubble growth rate in single bubbles has been observed to be $t^{1/3}$, which means the bubble growth rate slows down a little bit, and this implies that the contribution of the micro-layer should also reduce by the same fraction. Since both the whole micro-layer depletable models are specific to earth gravity conditions, they correctly do not implement this.

In the following section, a hybrid approach for calculating the contribution of a depletable micro-layer specifically for micro-gravity conditions is proposed. Details pertaining to the formulation of the approach is provided in the subsequent section, followed by comparison of results using the micro-layer model for the bubble growth, bubble shape, and heat-flux under micro-gravity conditions using pfnh as test liquid with experimental results performed on the ISS using the same liquid under same conditions from Dhir *et al.* [7].

2 Hybrid approach to calculate contribution of micro-layer under micro-gravity conditions

The term "hybrid" is used because this technique of calculation is a mixture of both the Contact Line model as well as the Whole depletable micro-layer model. The MoF code still treats the vapor bubble to be attached to the heater, that is it does not consider the presence of the micro-layer, but this approach calculates the flux of

vapor if the micro-layer were to be present in an ad-hoc way, and adds the flux term to the cells where the micro-layer would have been. This approach uses the benefits of both methods, the micro-layer life-cycle is in line to the actual physical process, and there is no additional sub-grid modeling necessary as only the contribution of the micro-layer is considered, which is the main goal of these models. Since no specific modeling of the micro-layer is needed, the term "approach" is used instead of calling it a model. But, even in the whole micro-layer models described above, the micro-layer thickness is typically estimated from experimental results. This is a major drawback of these models as the experiments are with specific liquids with different properties using specific wall-super heats. The same constant value would not be applicable to other liquids, hence the micro-layer thickness would be different.

For the hybrid approach implementation, a typical micro-layer is shown in figure 30. It should be noted than in figure 30, the micro-layer length considered is denoted as r_{mac}, the micro-layer thickness at the outer edge of the bubble is h_{mac}, and micro-layer thickness at the inner edge is h_{mic}, which is set to a very small value of $10^{-9}m$, corresponding to a few molecules thickness or the advection thickness mentioned earlier in Chapter I. the dry out radius of the neck of the bubble is denoted as r_{mic}, calculated from above mentioned h_{mic} value and using the same slope as that of h_{mac} and r_{mac}. r_{mac} is calculated at each step by using a color function technique. Based on the r_{mac}, the h_{mac} value is calculated which is the micro-layer thickness. In the hybrid approach, the initial thickness h_{mac} is estimated in a two step process, in the first step the hydrodynamic thickness is estimated using the analytical formulation of Olander and Watts1969 [53], which is given as:

$$h_{mac,1}(r) = \frac{\pi}{4\sqrt{3}} \frac{\rho_v h_{fg}}{\rho_l c_{pl} \Delta T} \sqrt{\frac{\nu_l}{\alpha_l}} r_{mac} \tag{45}$$

where $h_{mac,1}$ denotes the first step of the thickness determination. ρ_v and ρ_l are the densities of vapor phase and liquid phase respectively. ΔT is the wall super heat, ν_l is the kinematic viscosity of the liquid, and α_l is the liquid thermal diffusivity. This

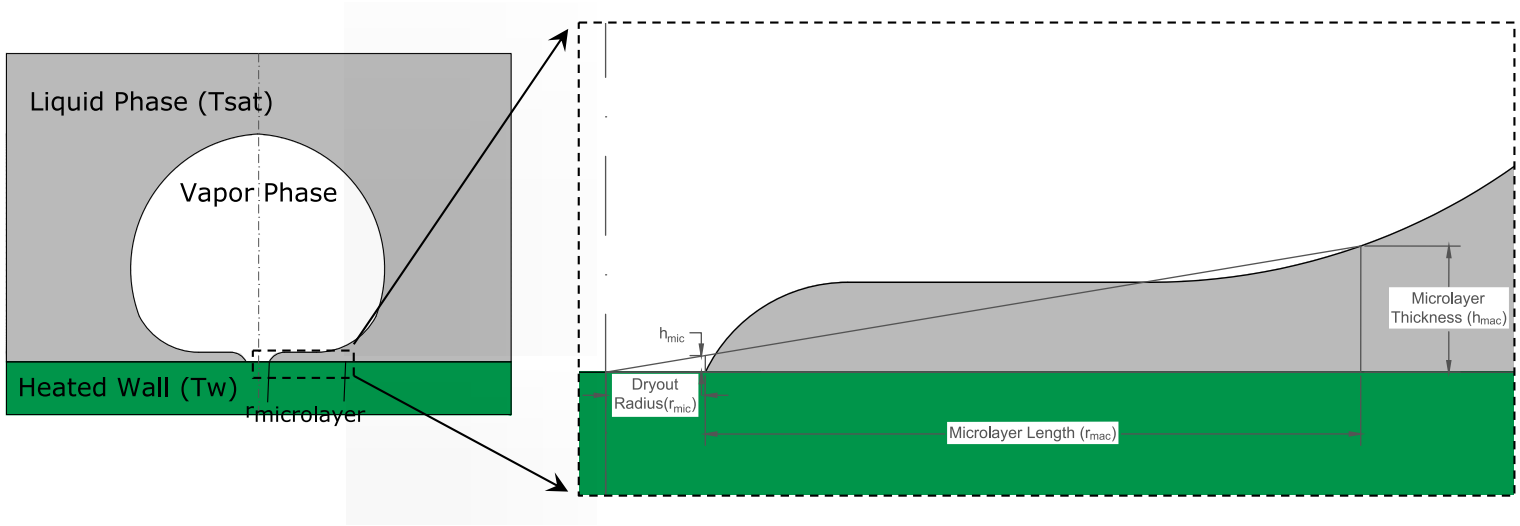

Figure 30. Micro-layer formulation in hybrid approach

equation provides an estimate of the initial micro-layer thickness based on the properties of the liquid in question, as well as the wall-super heat provided, and the radius of the base of the bubble. Also, this equation maintains the linear relationship between the radius and thickness of the micro-layer which has been reported by [50], and [47] using experiments. The two major drawbacks of this equation includes the fact that this equation makes an assumption that the bubble shape is spherical, which is not necessarily true under earth gravity conditions, as the bubble shapes are typically somewhat elongated in the vertical direction in terrestrial gravity conditions which would then change the micro-layer thickness as the base radius would be different. But in micro-gravity conditions, the bubble shapes have been found to be more oblate shaped (as in more squashed than the elongated shape in earth gravity condition) and hence resembles a sphere as can be seen in figure 31 from Dhir *et al.* [7] which shows bubble shapes at different time instants from experiments on the ISS.

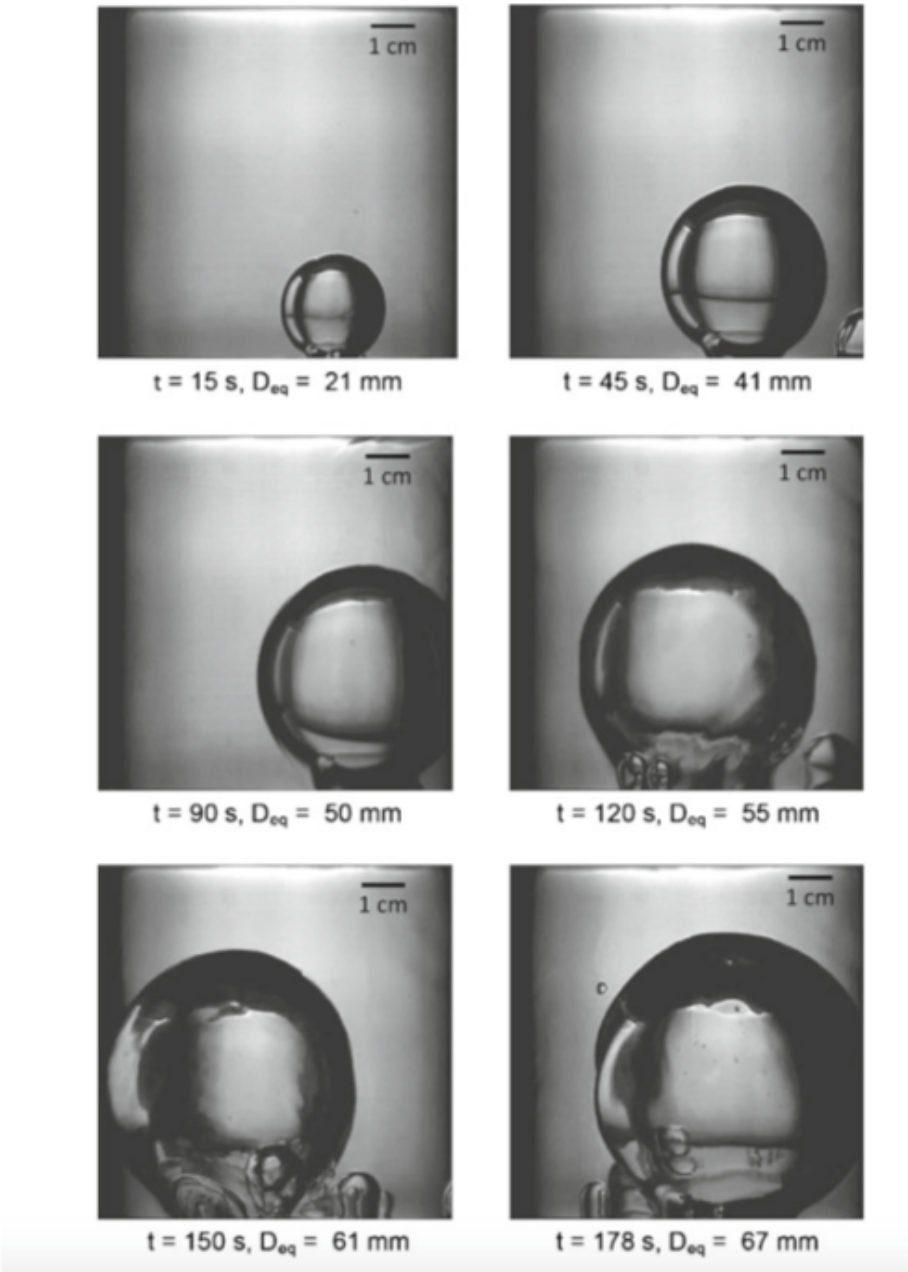

Figure 31. Bubble shape in micro-gravity form experiments on ISS: Img Source: Dhir *et al.* [7]

So, under micro-gravity conditions, this drawback becomes an advantage because spherical is the precise shape the bubble possesses and the assumption becomes indeed accurate. Second drawback of the equation is that it does not consider the depletion

or evaporation of the micro-layer. However, the hybrid approach uses an evaporation term [57, 58] which negates the drawback. This is the second step of the estimation of the micro-layer thickness.

$$h_{mac}(r,t) = \sqrt{(h_{mac,1}(r))^2 - \frac{2k_l(T_w - T_{int})}{\rho_l h_{fg}}t} \tag{46}$$

Using this equation, the micro-layer thickness is variable with time, based on the evaporation. Once the micro-layer thickness is known, the contribution of micro-layer in form of vapor flux is calculated. The derivation of the equation used for that is provided below starting with figure 32.

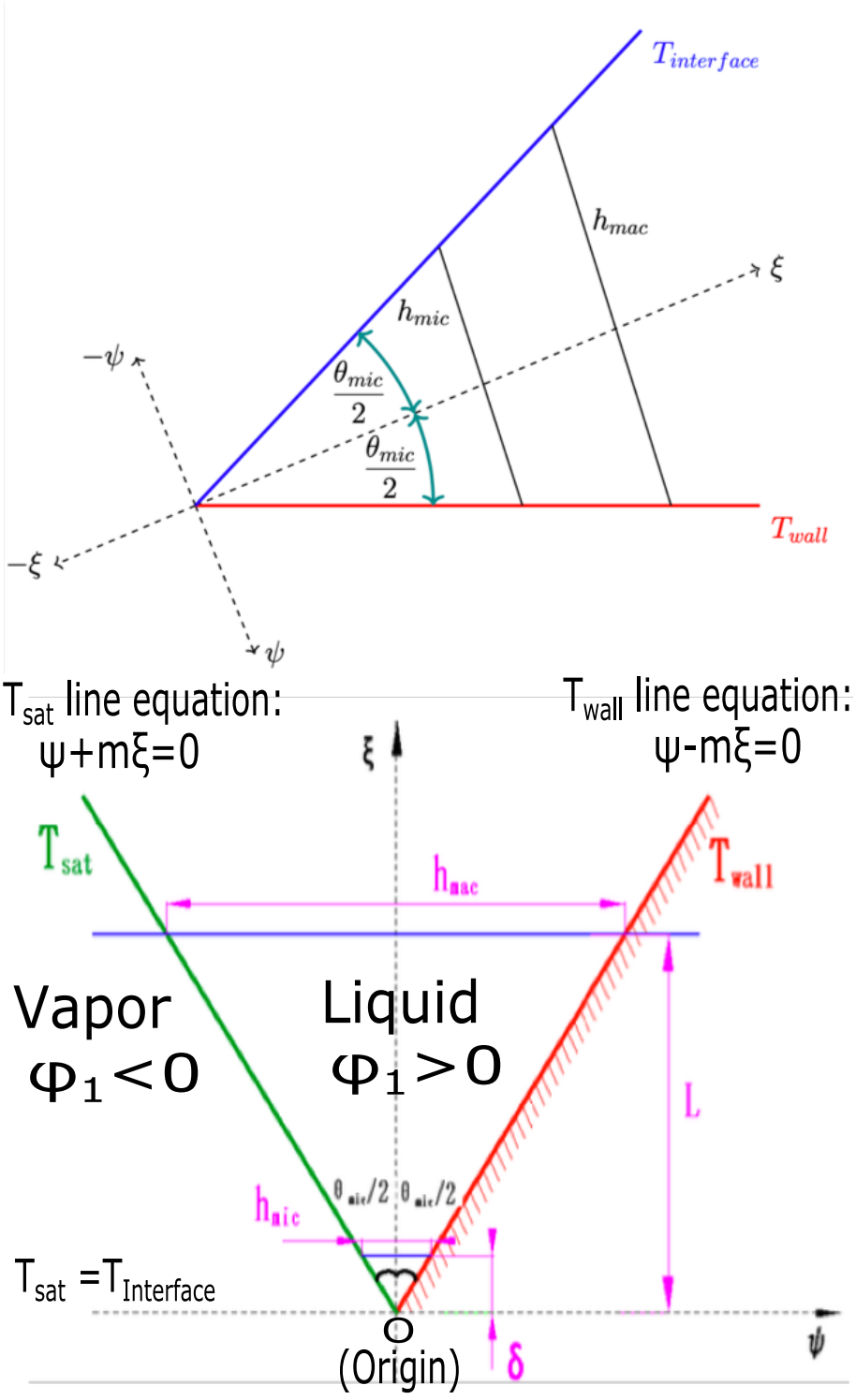

Figure 32. Calculation of micro-layer contribution

A portion of the micro-layer is shown in figure 32 (top), where T_{wall} and $T_{interface}$

denote the temperature of the wall and the interface (which is set to be the saturation temperature) respectively. Two axis perpendicular to each other are chosen as ξ and ψ. In order to better visualize the calculation, the image on the left is rotated so that ψ is along the x-axis and ξ is along the y-axis. Based on the figure, the following can be formulated:

$$\frac{h_{mac}/2}{L} = \tan\left(\frac{\theta_{mic}}{2}\right) = m \tag{47}$$

where m is the slope. Thus,

$$\psi_{wall} = h(\xi) = m\xi \tag{48}$$

and,

$$\psi_{Interface} = -h(\xi) = -m\xi \tag{49}$$

So, using interpolation the temperature as a function of ψ, and ξ can be written as:

$$T(\psi,\xi) = \left(\frac{T_s + T_w}{2}\right)\frac{\psi + h(\xi)}{0 + h(\xi)} - \frac{T_s\psi}{h(\xi} \tag{50}$$

Next, we set

$$\tilde{T} = \frac{T_s + T_w}{2} \tag{51}$$

and rewrite $T(\psi,\xi)$ as:

$$T(\psi,\xi) = \tilde{T} + \frac{(\tilde{T} - T_s)\psi}{h(\xi)} \tag{52}$$

The derivatives of $T(\psi,\xi)$ with respect to each of ψ and ξ becomes:

$$T_\psi = \frac{\tilde{T} - T_s}{h(\xi)} \tag{53}$$

$$T_\xi = \frac{-h'}{h^2}(\tilde{T} - T_s)\psi \tag{54}$$

ϕ_1 is a signed distance function. The subscript "1" denotes liquid phase. So ϕ_1 is positive in liquid region and negative in vapor region. The zero level set of ϕ_1 is the T_{sat} line in figure 32. Thus:

$$\phi_1 = \psi + m\xi \tag{55}$$

so the normal pointing into the liquid region from the vapor:

$$\vec{n} = \frac{\nabla\phi_1}{|\nabla\phi_1|} = \begin{bmatrix} 1 \\ m \end{bmatrix} \frac{1}{\sqrt{1+m^2}} \tag{56}$$

Thus, for the normal temperature gradient from the liquid phase region:

$$\nabla T \cdot \vec{n} = \frac{1}{\sqrt{1+m^2}} \begin{bmatrix} T_\psi \\ T_\xi \end{bmatrix} \cdot \begin{bmatrix} 1 \\ m \end{bmatrix} \tag{57}$$

This can be re-arranged as:

$$\begin{aligned} \nabla T^T \vec{n} = \begin{bmatrix} T_\psi & T_\xi \end{bmatrix} \vec{n} = \begin{bmatrix} \frac{\tilde{T} - T_s}{h(\xi)} & \frac{-h'}{h^2}(\tilde{T} - T_s)\psi \end{bmatrix} \begin{bmatrix} 1 \\ m \end{bmatrix} \frac{1}{\sqrt{1+m^2}} \\ = \frac{\tilde{T} - T_s}{h} \left[\sqrt{1+m^2}\right] \end{aligned} \tag{58}$$

Now,

$$\frac{1}{L-\delta} = \int_\delta^L \frac{1}{h(\xi)} d\xi = \frac{1}{L-\delta} \frac{1}{m} \ln \xi|_\delta^L = \frac{\ln \frac{L}{\delta}}{m(L-\delta)} \tag{59}$$

where $2\delta m = h_{micro}$. Thus, using these expressions, the average flux can be calculated as:

$$\frac{\tilde{T} - T_s}{m(L-\delta)} \left(\ln \frac{L}{\delta}\right) \sqrt{1+m^2} = \frac{T_w - T_s}{h_{macro} - h_{micro}} \left(\ln \frac{h_{macro}}{h_{micro}}\right) \sqrt{1+m^2} \tag{60}$$

Since m is very small, $\sqrt{1+m^2} \approx 1$, so the total mass of liquid from the region using the conduction equation becomes:

$$\dot{m}_{tot}^{liq} = \frac{-k_l(r_{mac} - r_{mic})}{h_{macro} - h_{micro}} \Delta T \log \left(\frac{h_{macro}}{h_{micro}}\right) / h_f g \tag{61}$$

where k_l is the thermal conductivity of the liquid, $(r_{mac} - r_{mic})$ is the area in 2-d, and h_{fg} is the latent heat of vaporization which converts heat energy to mass. Next, mass-flux contribution from each time-step is then computed and distributed across the relevant cells.

$$\dot{m}_{avg} = \frac{\dot{m}_{tot}}{n_{cell}} \times dt \tag{62}$$

where dt is the discretization time-step size. Average Vapor volume flux is calculated by multiplying a factor f.

$$\dot{v}_{avg}^{vap} = f \times \dot{m}_{avg}/\rho_v \tag{63}$$

The factor f ensures the $t^{1/3}$ growth rate for micro-gravity by limiting the vapor volume flux after r_{base} reaches a certain size ($size_{perim}$). This variable ($size_{perim}$) is a user defined value, and the simulations are run with different values and based on the comparison with experiments a final value is determined. A study on the effect of this parameter will be discussed later in this chapter. The algorithm for the factor, f can be summarized as:

`if` $(r_{base} \leq size_{perim})$ `then` $f = 1$

`else if` $(r_{base} > size_{perim})$ `then` $f = \dfrac{size_{perim}}{r_{base}}$

Here it is assumed that the contribution of the micro-layer is proportional to the bubble growth rate. A summary of the comparison of this approach with the two leading models are provided below in table 4.

Feature	**Dhir model**	**Sato model**	**Proposed Method**
Depletable Micro-layer	✗	✓	✓
Variable Micro-layer Thickness	✗	✓	✓
Length along majority radial extent	✗	✓	✓
Thickness of 1-cell size not required	✗	✓	✓
Thickness not based on water	✓	✗	✓
Sub-grid scale modeling not required	✓	✗	✓

Table 4. Comparison summary of microlayer model

As can be seen from table 4, the proposed novel approach addresses all the disadvantages of both the triple line model as well as the whole microlayer models available in the literature specifically for the cases under micro-gravity conditions.

3 Results and Discussion

Boiling results for a single vapor bubble in micro-gravity conditions is provided in this Section with comparison to the results from Dhir *et al.*(2012) [7], who performed the experiments on the ISS. The wall super-heat varied from $4^\circ - 7^\circ$C in the experiments. In the reported simulations a constant wall super heat of 7°C is used with no liquid sub-cooling. Perfluro-n-hexane is used as the test liquid, whose properties are given in table 2. First, a grid convergence study is reported in Figure 33, where the resolutions of 128x128, 192x192, and 256x256 are reported.

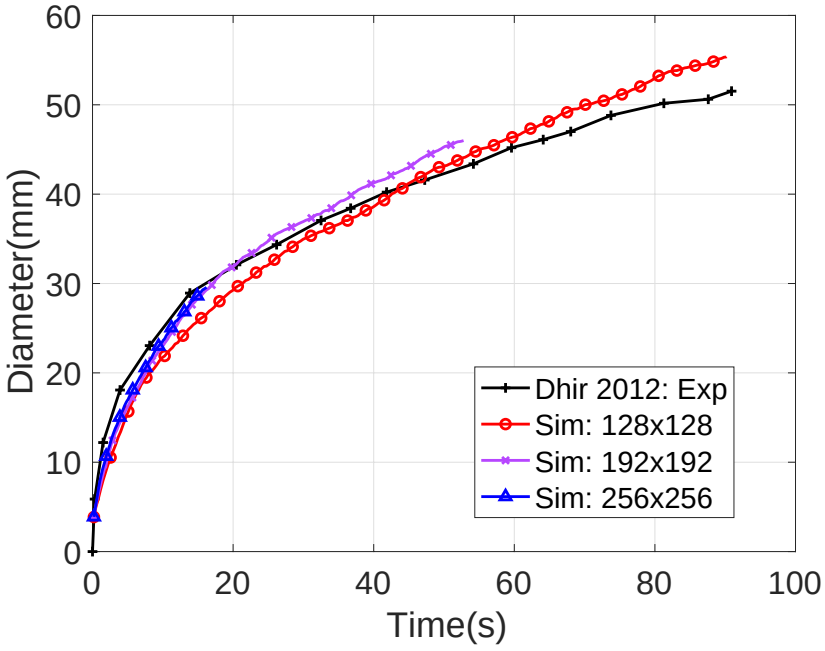

Figure 33. Grid convergence study

From Figure 33, it can be observed that 256x256 and 192x192 have converged. However, although 128x128, reports some difference, the has a maximum percentage difference between 128x128 and 192x192 at any point is $< 4.8\%$. Thus 128x128 can be considered to be a reasonable approximation. The domain size in each direction is 0.064 meters, which makes the cell size $\Delta x = 5.0 \times 10^{-4} m$ for 128x128, $\Delta x = 3.33 \times 10^{-4} m$ for 192x192, and $\Delta x = 2.5 \times 10^{-4} m$ for 256x256. This corresponds to 16 points inside the initial bubble along the diameter for 256x256, 12 points for 192x192, and 8 points for 128x128. As the 128x128 is computationally less expensive compared to the finer grid sizes and the percentage difference is in an acceptable range, 128x128 is chosen to be the default resolution for all the results reported from here onward. The time-step is calculated automatically based on the CFL stability criteria. It should also be noted that the $size_{perim}$ variable is set to a value of 0.04m for the cases in Figure 33. The simulations are in good agreement with the experimental results.

The assumption that contribution of the microlayer is proportional to the bubble growth rate is a reasonable one. In microgravity conditions, the growth rate is $\approx t^{1/2}$ initially and then $\approx t^{1/3}$ as opposed to earth gravity in which case the growth rate is $\approx t^{1/2}$. This can be seen from Figure 34.

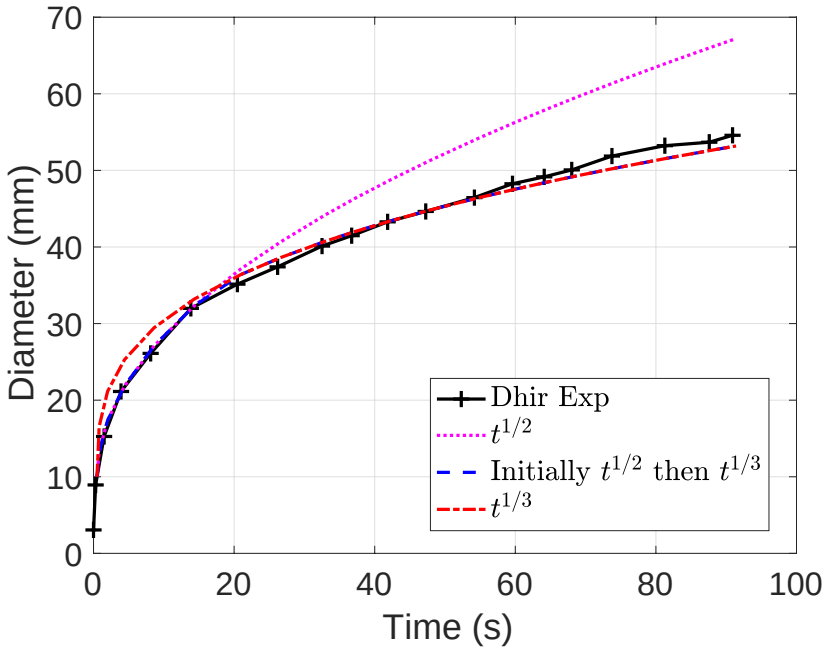

Figure 34. Comparison of growth rate with respect to different powers of time

As seen in Figure 34, the $t^{1/2}$ curve gives a good match initially, however it over predicts the diameter later. For the $t^{1/3}$ curve, the diameter is over predicted in the initial phase, but gives a good match in the later stage. A linear combination of these two powers gives the best match which follows $t^{1/2}$ initially, and $t^{1/3}$ later. The $size_{perim}$ variable determines when to switch from $t^{1/2}$ rate to $t^{1/3}$ from the perspective of the contribution of the microlayer. The change from 1/2 to 1/3 is mainly because the bubble size is larger in microgravity conditions and its growth rate is lower. Under earth gravity conditions, the bubble departs much earlier than in microgravity. For example: The departure diameter for water is about 1.4 mm in earth gravity [4, 63], but for similar conditions in reduced gravity, bubble departure was not observed [5]. As a matter of fact, the difference between 1/2 and 1/3 is small when the bubble size is less than 1 mm. The physics behind this reduction in microgravity could be attributed to the microlayer. As the bubble size keeps on growing, the size and thickness of the microlayer increases. So, it would take longer to evaporate the higher

quantity of liquid in the microlayer. Hence, it lowers the vapor volume flux from the microlayer, and thus reduces the bubble size compared to the earth gravity case.

Other assumptions in this approach include the fact that the bubble shape is spherical (as per the Olander and Watts equation), and the liquid in the microlayer is stagnant. One final assumption is that the microlayer thickness does not depend on the surface tension. The last two assumptions are somewhat related and are explained below.

Typically, the fluid flow in the microlayer is driven by the pressure difference between the liquid and vapor pressure, it is denoted by the below equation:

$$p_l = p_v - \sigma\kappa - \frac{A}{\delta^3} \tag{64}$$

The third term on the Right Hand Side (RHS) of equation 64 is the dis-joining pressure, which arises from attractive forces between molecules in the fluid and the solid, A is the is the dispersion constant relating dis-joining pressure to the film thickness. This term is very small as these forces typically act in the range of few molecular diameters (on the order $< 1nm$), and thus can be neglected. The surface tension contribution only comes into the picture due to the second term on the RHS. However, since the liquid film is almost flat, the curvature of the vapor-liquid interface can be assumed to negligible, which makes the capillary pressure term $\sigma\kappa$ to be ≈ 0. So the above equation reduces to:

$$p_l \approx p_v \tag{65}$$

As the pressure difference is almost negligible, it can be safely assumed that the liquid in the microlayer is stagnant.

Next, the effect of the $size_{perim}$ variable is reported in Figure 35.

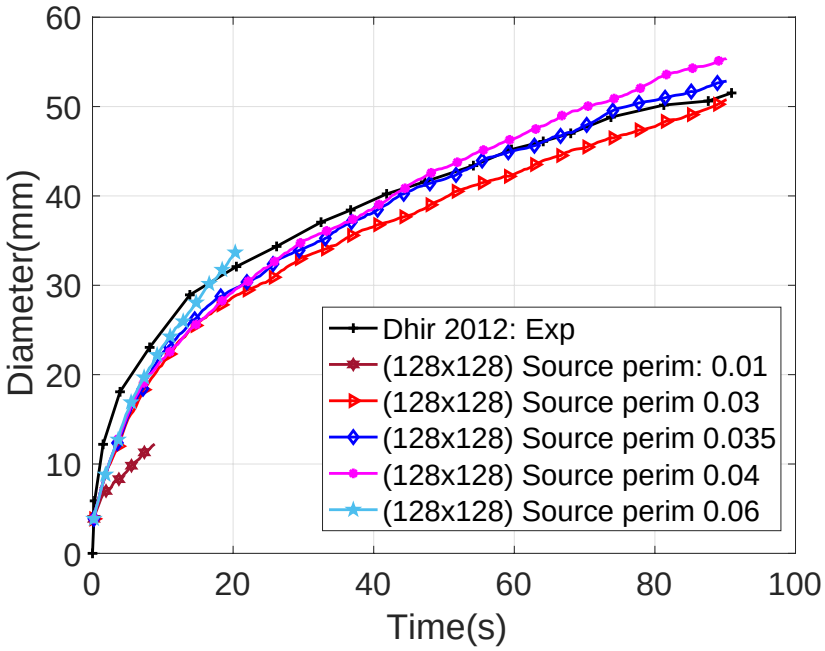

Figure 35. Effect of variable $size_{perim}$ or $source_{perim}$

As can be observed from Figure 35, as the value of $size_{perim}$ increases, the bubble growth rate flattens at a lower position and with a lower slope. From Figure 35, it can be seen that $size_{perim} = 0.035$m gives a better agreement with the experimental results, however, it should be noted that the experiments on ISS went through some complications, and they were able to perform only one completed single bubble experiment which makes the standard deviation high. These anomalies could certainly add into the uncertainty of the experimental results itself. So, a recommendation of $size_{perim}$ in the range of $0.035 - 0.04$m is a reasonable approximation.

Heat-flux as a function of the X-position at time, $t = 15s$ is shown in Figure 36.

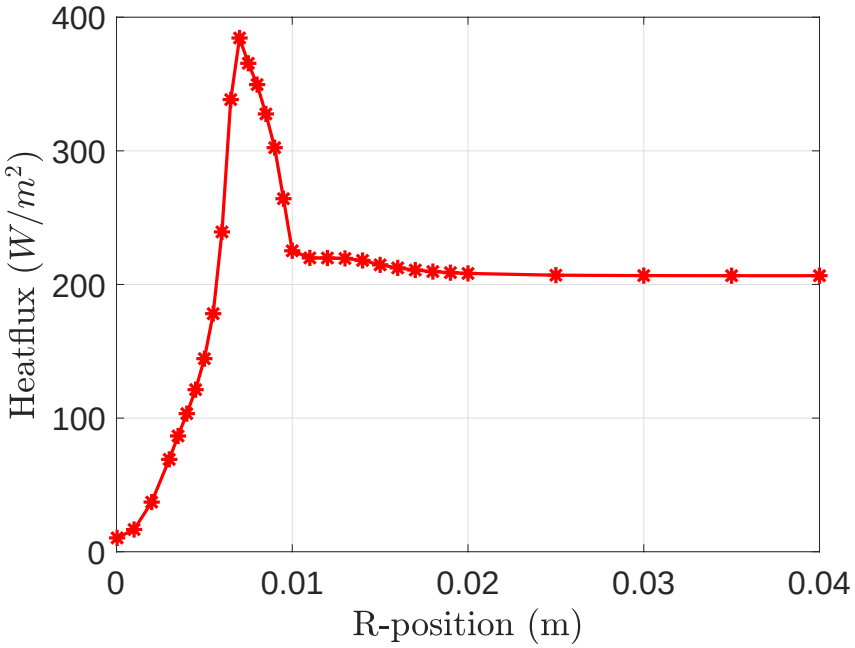

Figure 36. Heat flux at time, $t = 15s$

As can be seen from Figure 36, a peak of the heat-flux can be observed at the triple point as majority of the phase change takes place at this specific location. The maximum heat-flux value as per the MoF simulations is 384.4W/m^2 at $t = 15s$. Similar trend is also observed at time, $t = 60s$ in Figure 37.

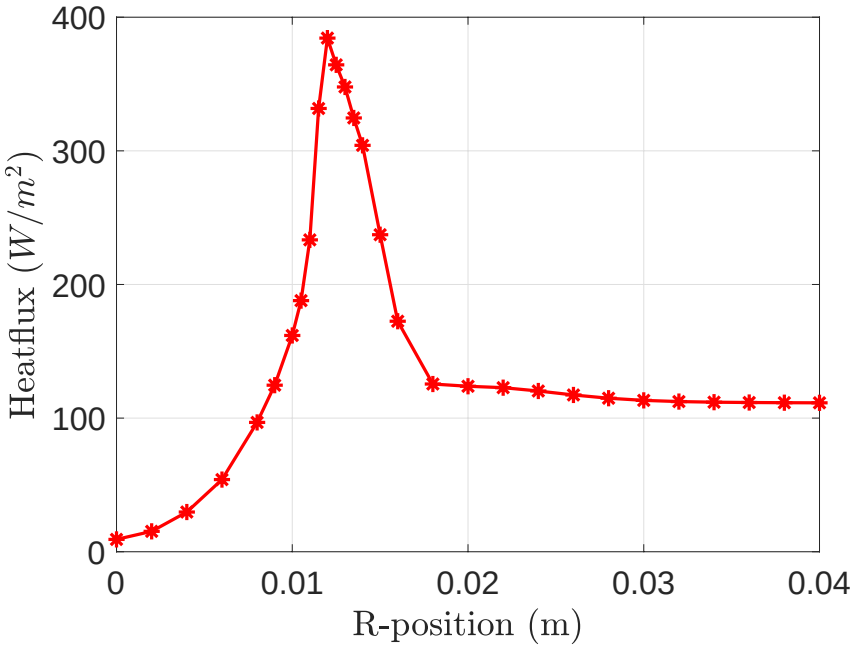

Figure 37. Heat flux at time, $t = 60s$

Dhir *et al.*(2012) [7] reports similar results, and the comparison would be provided later in the Section along with the bubble shape. In Figure 37, at $t = 60s$, the peak of heat-flux is at a higher value of the X-position in comparison to Figure 36 at $t = 15s$. This is because at $t = 15s$, the bubble base radius is smaller, and as the bubble has grown to a larger size, the bubble radius and hence the triple point is at a higher X-value at $t = 60s$. The two time-values of $t = 15s$, and $t = 60s$, are chosen so that comparison could be made to results from experiments by Dhir *et al.*(2012) [7], as they reported results at the same two instants.

Next, the velocity vectors near the triple point is reported for time-instant of $t = 15s$ in Figure 38.

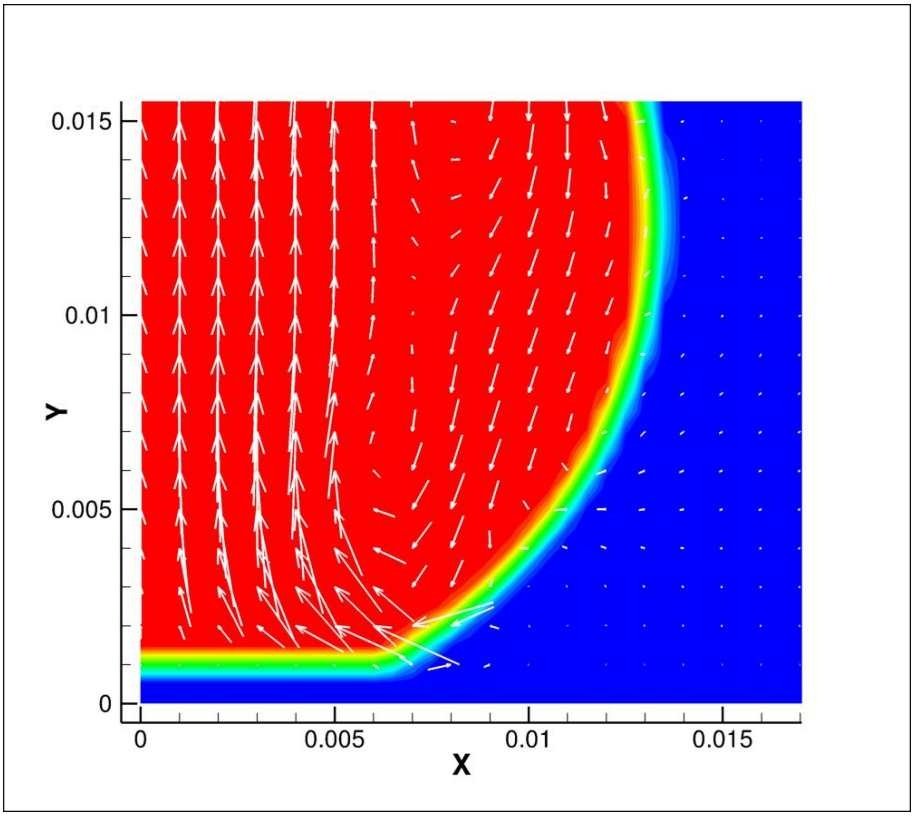

Figure 38. Velocity vectors near triple point at time, $t = 15s$

Similar results for velocity vectors near triple point is also reported for time-instant of $t = 60s$ in Figure 39.

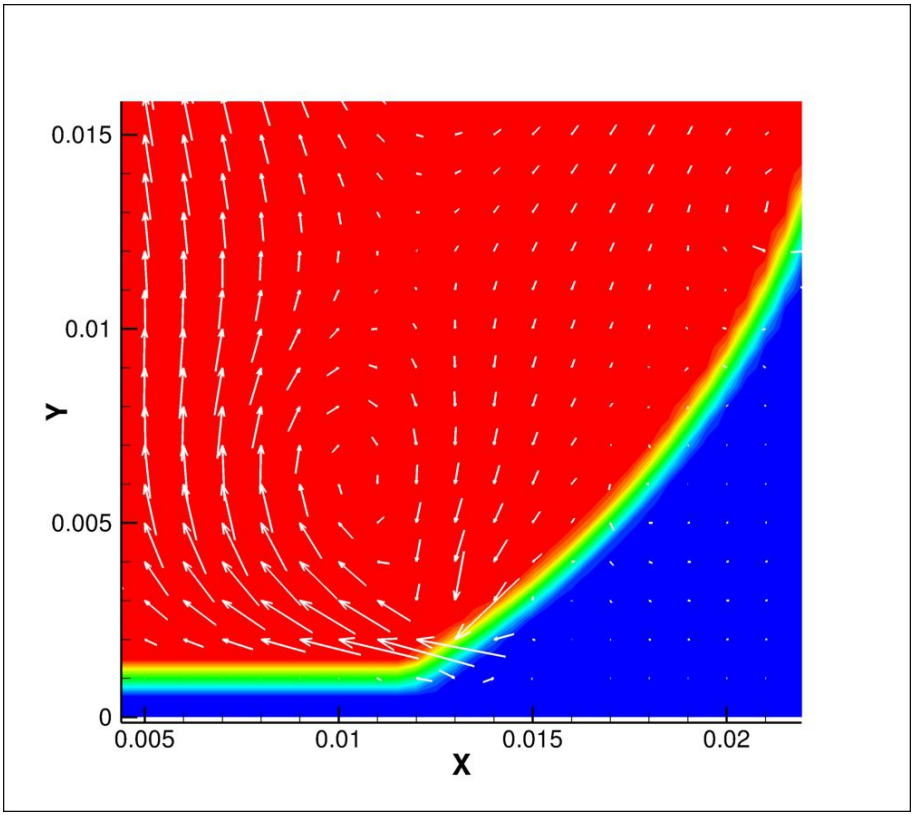

Figure 39. Velocity vector near triple point at time, $t = 60s$

Both results in Figures 38 and 39 show that the velocity field is similar near the triple point at the two time-instants.

Bubble shape along with temperature distribution comparison with experiments and numerical simulations of Dhir *et al.*(2012) [7] at time, $t = 15s$ are reported in Figure 40.

Also reported in the Figure is the heat-flux comparison at that time instant as a function of the X-position. Dhir *et al.*(2012) [7] reports the experimental and numerical results on the left. The MoF simulation results are on the right. The heat-flux for experimental results (shown with black line) do not show a peak at the triple point due to insufficient resolution in the experiments. Similar comparison is also reported for time, $t = 60s$ in Figure 41.

It should be noted that the image on the left shows a unit of W/cm^2 for the

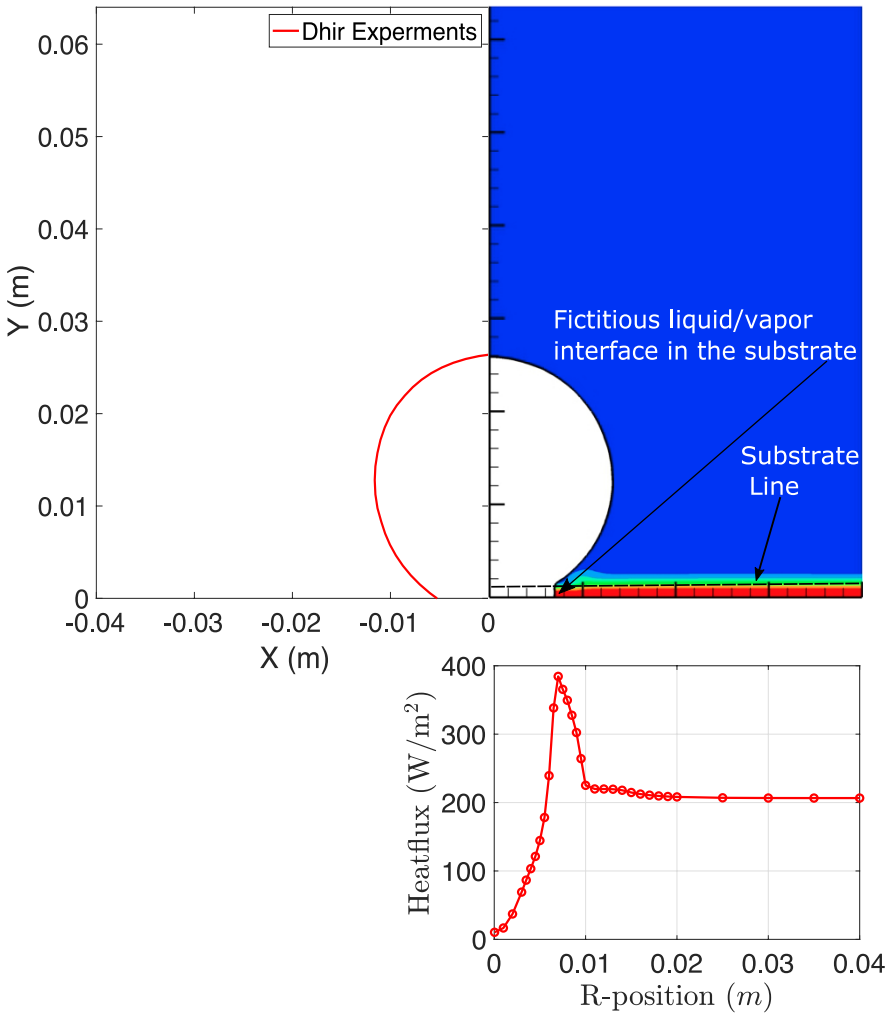

Figure 40. Comparison of bubble shape along with heat-flux and temperature distribution at time, $t = 15s$ between Dhir *et al.*(2012) [7] experimental and numerical results (left) and Dhir *et al.*(2012) [7] Experimental and present MoF simulations (right)

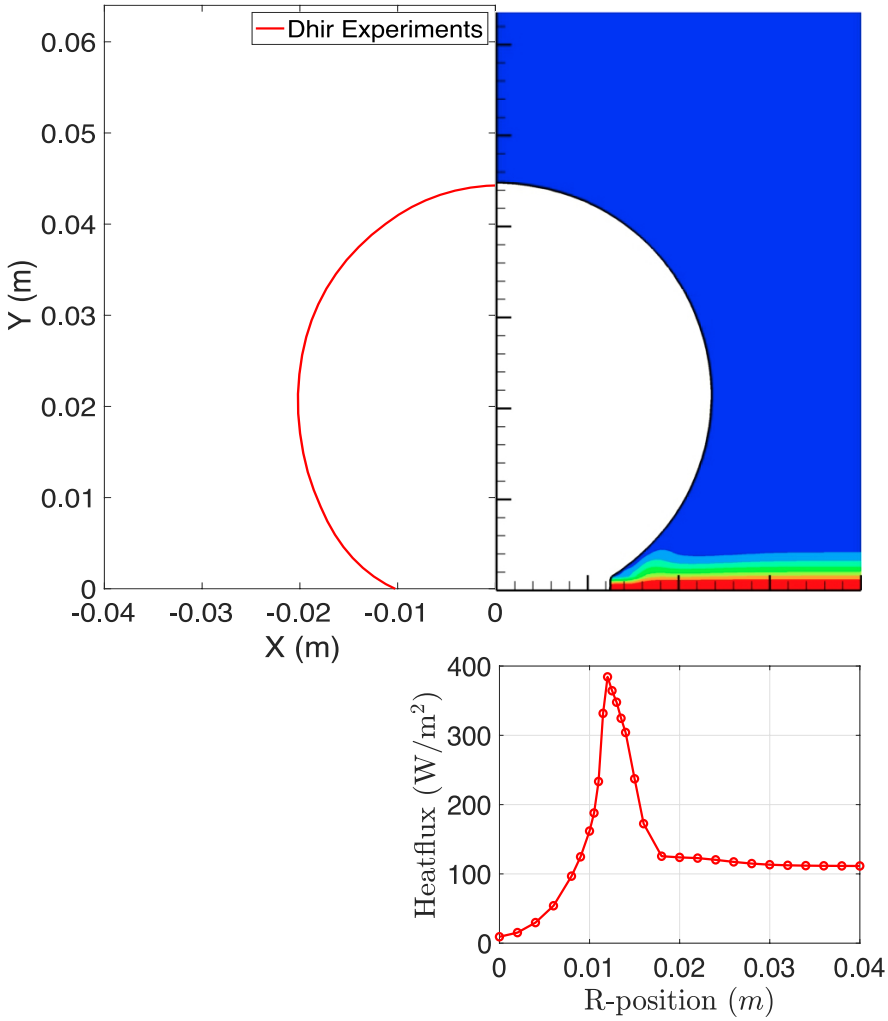

Figure 41. Comparison of bubble Shape along with heat flux and temperature distribution at time, $t = 60s$ between Dhir *et al.*(2012) [7] experimental and numerical results (left) and Dhir *et al.*(2012) [7] Experimental and present MoF simulations (right)

heat-flux, and the MoF simulation reports W/m^2, this is because the image has a typographical error. They report the correct results in their paper in the text, and flux values in units of W/cm^2 are too high and W/m^2 values are the ones that makes reasonable sense given the size of the heater they used. Dhir *et al.*(2012) [7] reports a peak value of heat-flux of $574W/m^2$ at both $t = 15s$ and $t = 60s$ time instants, and the MoF simulations reports $384W/m^2$ at $t = 15s$ and $388W/m^2$ at $t = 60s$ time instants. These values are in comparable range.

The results validate the reported microlayer approach formulated for micro-gravity simulations. This approach considers the microlayer length to be along almost the entire radial extent of the bubble base, and the microlayer thickness is variable with time and radius of the bubble base. The depletion of the microlayer is incorporated using the evaporation term, so the microlayer follows a similar trend as observed in experiments. This approach could be used for any test liquid under micro-gravity conditions, and there is no requirement to 'model' the microlayer, as the contribution of the microlayer is being considered, so less computations are needed making the approach faster as well.

CHAPTER V

DATA-DRIVEN PREDICTION FOR NUCLEATE BOILING

1 Introduction

The interest in nucleate boiling is mainly due to high heat flux generated at considerably lower wall superheats. This makes nucleate boiling an efficient mode of heat transfer for cooling applications including cooling in microgravity where an efficient medium of heat transfer is required to make the components more compact.

The typical nature of the boiling curve during the nucleate boiling phase generally shows a sharp increase in the heat flux with increase in wall superheat up to a maximum value known as Critical Heat Flux (CHF). Beyond the CHF, a decrease in the heat flux value is observed with an increase in wall superheat [83]. It is difficult to control the heat flux near the CHF because nucleate boiling is a complicated process that comprises of multiple mechanisms such as liquid-vapor phase change, bubble dynamics, contact line dynamics, and nucleation site densities [10]. These mechanisms further depend on experimental parameters such as wall superheat, liquid sub cooling, gravity, surface roughness and thermo-physical properties of the liquid and vapor in question. One of the goals of nucleate boiling research has been to provide a generalized prediction of the heat flux based on other experimental input parameters such that it can be maintained at an optimum value close to the CHF [4]. Empirical correlations have been reported in the literature, however they lack the accuracy for a general mechanistic prediction [10].

Empirical Correlations

Multiple studies related to experiments, numerical simulations and predictive correlations of nucleate boiling have been reported in the literature [84]. Numerical simulation studies are typically performed for specific cases, and are computationally expensive. Additionally, simulations are challenging due to complexities arising from phase change and bubble dynamics. Similarly experiments are also performed for specific cases. Predictive correlations have also been reported in literature, most of which were developed by using empirical coefficients. Rohsenow (1952) [8] proposed one of the first correlations in nucleate boiling. He related the heat flux, $\dot{q}$ to the wall superheat, ΔT_w by the assumption of a single phase forced convection problem.

$$\frac{c_{pl}\Delta T_w}{h_{fg}} = C_s \left[\frac{\dot{q}\sqrt{\dfrac{\sigma}{g\left(\rho_l - \rho_v\right)}}}{\mu_l h_{fg}} \right]^{1/3} Pr_l^{1\text{or}1.7} \tag{66}$$

In Rohsenow's model C_s depends on the heater material and fluid combination. Later Liaw and Dhir (1989) [85] improved Rohsenow's model. In the improved model C_s varies linearly with contact angle.

$$\frac{\dot{q}\sqrt{\dfrac{\sigma}{g(\rho_l - rho_v)}}}{\mu_l h_{fg}} = C_s^{-3} \left[\frac{c_{pl}\Delta T_w}{h_{fg}} \right]^3 Pr_l^{-3\text{or}-5.1} \tag{67}$$

In equations 66, and 67, c_p is the specific heat, $\dot{q}$ is the heat-flux, h_{fg} is the latent heat of vaporization, σ is the surface tension, g is the acceleration due to gravity, ρ_l, ρ_v are the liquid phase and vapor phase densities respectively. μ_l is the viscosity of the liquid. The exponent value of -3 for water and -5.1 for all other liquids to the Prandtl Number (Pr_l) in equation 67 were obtained empirically. Rohsenow proposed that C_s depends on the heater material and fluid combination, but later Liaw and Dhir (1989) [85] showed that C_s varies linearly with contact angle.

Stephan and Abdelsalam (1980) [9] also provided a correlation by determining the important fluid property groups using regression analysis. The correlation provided

by them considers bubble departure diameter (D_d) as a variable, which is difficult to be considered as an input parameter for predicting heat flux in industrial applications. The correlation by Stephan and Abdelsalam does not consider surface parameters while Rohsenow's correlation implicitly considers surface contribution through a proportionality constant C_s. Stephan and Abdelsalam's correlation does not consider gravity but Rohsenow's equation considers gravity. Other correlations related to nucleate boiling have been proposed by studies of Fritz [11], and Gorenflow [12] among others, however these correlations are specific to sub process mechanisms such as bubble dynamics and nucleation site densities. Thus, these correlations do not aid in predicting the general heat flux. Rohsenow's corrected equation by Liaw and Dhir is a widely adopted model for the prediction of heat flux.

Machine Learning Techniques

Multiple studies on nucleate boiling experiments have been performed. Significant amount of data from these experiments is generated. These data can be exploited to identify new features and build better prediction models . It has been shown that Machine Learning models have been effective in their predictive capabilities across multiple fields. Computer Vision [86], Natural Language Processing [87], Software Engineering [88–92], Epidemiology [93] and Environmental Sciences [94] are some of the fields in which it has been used with great success. Machine learning models including Artificial Neural Networks (ANNs), have been used for prediction in fluid flow and heat transfer based problems too. Alizadehdakhel *et al.* (2019) [95] performed experiments, Computational Fluid Dynamics (CFD) simulations and neural network predictions of multiphase flow pressure drop in an unsteady problem. Jambunathan *et al.*(1996) [96] used back-propagation algorithm based neural networks to predict convective heat transfer coefficient in a duct. Ling *et al.*(2015) [97] evaluated different machine learning algorithms for prediction of turbulence modeling. Rajen-

dran *et al.*(2018) [98] performed vortex detection on unsteady CFD simulations using recurrent neural networks. Singh *et al.*(2018) [99] combined numerical simulations with ANNs to perform thermal modeling in HVAC systems. Mohan *et al.*(2018) [100] implemented deep neural networks to build a Reduced Order Model (ROM) using dimensionality reduction technique like Proper Orthogonal Decomposition (POD). They use high-fidelity Direct Numerical Simulation (DNS) data to train the model. This is significant since DNS is computationally expensive specifically for turbulent flows [101, 102]. Naphon *et al.*(2016) [103] applied ANNs to analyze heat transfer of spirally fluted tubes. Guo *et al.*(2016), [104] used convolution neural networks for steady flow approximation of flow over vehicles. They train the model with velocity field data over primitive shapes like triangles, quadrilaterals, hexagons, at steady state. Then the model predicts the velocity field of multiple car samples provided as images. Wang *et al.*(2017) [105] used Random Forest algorithm to reconstruct discrepancy between RANS stress modeling and DNS data.

Machine learning models have also been used in predictions of boiling related research works. Liu *et al.*(2018) [106] predicted heat transfer from near wall local features using simulation data from four different heat flux values for boiling. They showed that the neural network model works well in case of both interpolation and extrapolation cases with respect to the training values provided. Since the training data for their neural networks are generated from simulation data, the same method cannot be used for experimental data because the type of input parameters Liu *et al.*(2018) uses for training for their model, such as pressure gradient and momentum convection are hard to determine a-priori in experiment. Hassanpour *et al.*(2018) [107] compared different Artificial Intelligence (AI) techniques for prediction of boiling heat transfer coefficient of alumina water based nano-fluids. Their results confirmed that diameter of nano-particles, its weight concentration in base fluid, wall superheat, and operating pressure are the best independent variables for estimating the pool boiling

heat transfer coefficient of water-alumina nano-fluid. Mazzola (1997) [108] integrated ANNs and empirical correlations for predicting the CHF for subcooled water. They provided a range for the variables determined from curve fitting techniques in order to predict the CHF. They report that their method would likely be suitable for thermal-hydraulic and heat transfer data processing. Alimoradi *et al.*(2017) [109] used ANNs to study optimization of subcooled flow boiling in a vertical pipe. They determined that there is an optimum condition which leads to minimizing the surface temperature and maximizing the averaged vapor volume fraction. They report that this optimization technique could be used to avoid burning the walls while maintaining maximum vapor volume fraction. Scalabrin *et al.*(2006) [110] modeled flow boiling heat transfer of pure fluids using ANNs. They report improvements to the conventional correlations in flow boiling using ANNs. Qiu *et al.*(2020) [111] used ANNs model to predict mini/micro-channels saturated flow boiling heat transfer coefficient. They report that the ANNs model did extremely well when a working fluid data was included in the training dataset, and poorly when a working fluid data was excluded from training dataset. Zhou *et al.*(2020) [112] compared ANNs predictions with other machine learning models for prediction of flow condensation heat transfer coefficients. They report machine learning models performed better than generalized correlation equation. Bubble images have been used by Suh *et al.*(2021) [113] as input to predict pool boiling characteristics as well. None of these works considered variation in gravity, and very few of them use data from multiple test liquids. McClure *et al.*(2021) [114] did consider gravity in order to predict heat flux, however they only considered four input parameters: wall superheat, gravity, surface tension, pressure. They did not consider liquid subcooling, vapor and liquid densities, thermal conductivity and other parameters which will be shown to be significant in the feature importance study presented in this work. This work uses deep learning to create a model for nucleate boiling heatflux with a comprehensive set of all of the significant

input parameters including gravity for five different test liquids. These input parameters were determined based on four different feature importance techniques. So far according to the author's knowledge no other study has done this.

Limited dataset size is another issue that needs to be addressed. Using a high number of input parameters while the number of training samples are low could reduce the model accuracy as the dimensionality for the model to learn would be high. To solve that problem, we propose to use a combination of feature selection techniques and dimensional analysis to reduce the number of input parameters. This helps in keeping the information of each variable intact, and yet reducing the number of parameters which aids in model convergence and increasing model accuracy, and reduces training time [115]. In this work, we use one algorithm from each of the three feature selection methods: Wrapper Methods, Filter Methods, and Embedded Methods.

Wrapper Methods: This method selects features by comparing the model's accuracy while (a) the specific feature is selected, and (b) the specific feature is not selected. It uses a predictive model to rate each feature. The entire feature set once including and once excluding the feature is used to train a model, both are tested on an unseen dataset and compared for increase or decrease in error to determine the significance of that particular feature. Although wrapper methods are computationally expensive, they can provide the best performing feature set for that particular problem [116]. Forward sequential wrapper methods where the model starts with an empty set, then adds features as the performance varies [117] and Backward sequential wrapper methods where the algorithm starts with all available features, then it removes the feature whose elimination increases the model accuracy [118] are common types of wrapper methods.

Filter Methods: Filter methods use statistical quantities to provide a score to each feature. These scores reflect the degree of correlation of each feature with the

target variable. This method is fast to compute, but it may fail in capturing the best features if they are not statistically correlated to the target variable.Common wrapper methods include F-score ([119]), Mutual Information [120], and Pearson Correlation [121] among others.

Embedded Methods: In this method, feature selection is part of the model construction process. It is implemented by algorithms that have their own built-in feature selection methods. LASSO [122] (Least Absolute Shrinkage and Selection Operator) and Ridge regression technique [123] are popular examples of embedded methods. LASSO for example, constructs a linear model by penalizing the regression coefficients with a L1 penalty. This reduces some coefficients to zero. Features with non-zero regression coefficients are 'selected' by the LASSO algorithm.

The accuracy of machine learning models depends on the quality and quantity of the dataset. In many cases, like the study of nucleate boiling, the dataset is very limited while the number of features involved is large, which can be problematic to train the model ([107], [110], [124]). To address the problem we propose an approach to reduce the number of features and to improve model prediction accuracy. The approach consists of two steps:

- Step 1: Reduce number of features from 12 to 8 by using feature selection techniques as mentioned above.
- Step 2: Using the 8 selected variables from Step 1, we perform dimensional analysis to generate 4 non-dimensional Π terms.

In this way, we reduce the dimensionality in the problem. In Step 1, we use a total of four feature selection techniques: one from each of the three methods, namely, the Backward Elimination Technique (Wrapper Method), Pearson Correlation (Filter Method) and LASSO (Embedded Method) and an additional manual-wrapper type method based on results of ANNs model which was trained by removing one feature

at a time. Based on the combined conclusion from all the techniques we select the eight variables for performing dimensional analysis in Step 2.

In this work, we use ANNs to predict nucleate boiling heat flux. Comparisons are made between models that are trained based on (1) a consolidated experimental dataset using all 12 parameters as input and (2) the reduced dataset with 3 non-dimensional Π terms as input. The effectiveness of our approach is highlighted by the change in the reported error metric MAPE (Mean Absolute Percentage Error) values. We compare the ANNs predictions for both datasets against other machine learning models such as Random Forest-Regression (RFR) and Extreme Gradient Boost (XG-Boost or XGB) algorithms. Additionally, we compare the ANN model prediction to a well known boiling correlation prediction (Liaw and Dhir [85]-corrected Rohsenow's equation [8]). Our results show that using feature selection study and dimensional analysis to reduce the number of parameters is a viable option to generate accurate predictions from machine learning models for a limited dataset size. The remainder of the chapter is divided as follows: Section 2 provides the methods description and reports the details on the dataset, a discussion on the feature importance study and dimensional analysis performed. Section 3 provides ANNs prediction results using Dataset-B and discusses the comparison of ANNs prediction with other machine learning models for both Dataset-A and Dataset-B. It also includes discussion on effect of parameters and parameter significance for different regimes and conditions. Additionally, comparison of heat flux prediction is provided between ANNs and Rohsenow's correlation.

2 Method

This section provides details on the methods used. Description of ANNs methodology, ANNs architecture, the full dataset used, details pertaining to the feature selection study, and the dimensional analysis description.

ANNs

A neural network [125] is a collection of mutually connected units or neurons. Each neuron in a network has a single task, and it is connected to multiple other neurons in the same layer. A regular neural network with four inputs X_1, X_2, X_3, and X_4 (for example density and viscosity in the fluid flow cases) is shown in figure 42. The first layer (to the extreme left) is called the input layer which contains the features.

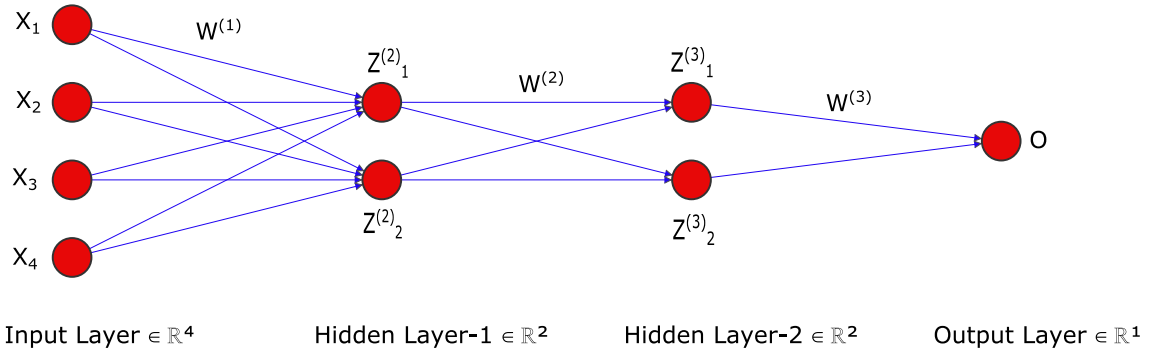

Figure 42. Regular Neural Network

Also shown in figure 42 is the output layer shown on the extreme right consisting of only one unit named O which corresponds to the label (for example: heat flux in this work). The layers shown in the middle are hidden layers. In figure 42 two hidden layers are shown, each with two neurons. For complicated problems multiple layers are usually employed. Also the input and output layers can consist of multiple features and labels. A step-by-step description of the process is provided below. In our case, we train the model for 2500 epochs or iterations. Model architecture for the boiling parameters case that is used in this work for DATASET-A consists of 12 input parameters. The output layer at the extreme right contains one unit which corresponds to the heat flux.

A step wise description of the ANN process is given below:

Step 1: Each Neuron attaches a weight to each of its inputs to create a linear function of the them. For each layer, the values at the hidden neurons are computed

by using the weights, biases and activation functions (to address non-linearity). So for neurons in layer $l = 2$:

$$z^{(2)} = W^{(1)}x + b^{(1)} \tag{68}$$

$$a^{(2)} = f(z^{(2)}) \tag{69}$$

The equation for $z^{(2)}$ (equation 68) could also be written in an expanded form as:

$$z^{(2)} = \begin{bmatrix} W_{11}^{(1)}x_1 + W_{12}^{(1)}x_2 + W_{13}^{(1)}x_3 + W_{14}^{(1)}x_4 \\ W_{21}^{(1)}x_1 + W_{22}^{(1)}x_2 + W_{23}^{(1)}x_3 + W_{24}^{(1)}x_4 \end{bmatrix} + \begin{bmatrix} b_1^{(1)} \\ b_2^{(1)} \end{bmatrix} \tag{70}$$

where $z^{(l)}$ is the value of the neuron in layer l, W denotes the weight and superscript of W denotes the layer number. b denotes the bias. The first digit in the subscript of W denotes the index of the neuron in the next layer and the second digit denotes the index of the neuron in previous layer. For neurons in layer $l = 3$, the equations would be:

$$z^{(3)} = W^{(2)}a^{(2)} + b^{(2)} \tag{71}$$

$$a^{(3)} = f(z^{(3)}) \tag{72}$$

Here a is the activation function. In our case it is the $ReLU$ function which is an abbreviation for Rectified Linear Unit. This function returns 0 if it receives any negative input, but for any positive value x, it returns that value back. Mathematically, $ReLU$ can be depicted as:

$$a(x) = \max(0, x) \tag{73}$$

A graphical representation of ReLu is shown in figure 43.

Step 2: The weight values associated with each neuron is updated to create a model during training with the aim of minimizing the loss function. In our model we use 'Mean Absolute Error' (MAE) as the loss function. Loss function for our model is given as:

$$L(y, \hat{y}) = \frac{1}{m}\sum_{i=1}^{m}(y_i - \hat{y}_i) \tag{74}$$

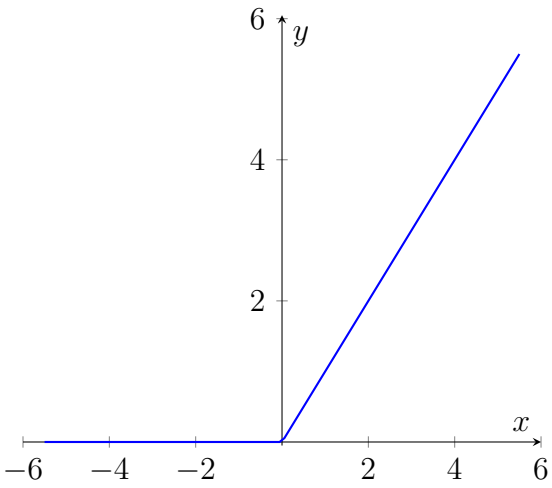

Figure 43. Graphical Representation of ReLU

Here $\hat{y}$ is the output produced by the model, and y is the target value. The goal of the model is to minimize the loss function L.

Step 3: Based on the value of the loss function the model determines how much to adjust the weights and biases so that the error can be minimized. This is done using the Back-propagation algorithm. The determination of the degree of adjustment to the weight functions is done by computing the gradient of the loss function with respect to the weight values by using the chain rule. For a single weight $W_{mn}^{(l)}$, the process can be depicted mathematically as:

$$\frac{\partial L}{\partial W_{mn}^{(l)}} = \frac{\partial L}{\partial z_m^{(l)}} \frac{\partial z_n^{(l)}}{\partial W_{mn}^{(l)}} \tag{75}$$

But, it is already known that:

$$z_m^{(l)} = \sum_{n=1}^{s} W_{mn}^{(l)} a_n^{(l-1)} + b_m^{(l)} \tag{76}$$

where s is the number of neurons in layer $(l-1)$. Differentiating,

$$\frac{\partial z_m^{(l)}}{\partial W_{mn}^{(l)}} = a_n^{(l-1)} \tag{77}$$

Plugging into equation 75, we get:

$$\frac{\partial L}{\partial W_{mn}^{(l)}} = \frac{\partial L}{\partial z_m^{(l)}} a_n^{(l-1)} \tag{78}$$

Similar set of equations are also applied for the bias functions as well.

Step 4: Once the partial derivatives of the weights are calculated at each epoch, an optimizer is used to reduce the Loss function. In our problem we use the well-known RMSprop or 'Root Mean Square Propagation' optimizer. The process in which RMSprop minimizes the Loss function is shown below:

$$W_{t+1} = W_t - \frac{\alpha}{\sqrt{S_t + \epsilon}} \cdot \frac{\partial L}{\partial W_t} \tag{79}$$

where

$$S_t = \beta S_{t-1} + (1 - \beta) \left[\frac{\partial L}{\partial W_t} \right]^2 \tag{80}$$

Here W is the weight, α is the learning rate with a default value of 0.001. β is a parameter which determines the decay of the learning rate, it has the default value of 0.9. ϵ is the fuzz factor which ensures a division by zero or the vanishing gradient problem does not arise. It has a default value of $(1E-6)$. t is the time-step or epoch in consideration which makes $(t-1)$ to be the previous epoch. Steps 1-4 are repeated in each epoch.

Other Machine Learning Models

Here we provide a brief description of the two other machine learning models used.

- Random Forest [126]: Random Forest is based on the decision tree algorithm. Decision trees are predictive models that use a set of binary rules to calculate a target value. It estimates the target value with a series of questions to the data, each question narrowing the possible values until the model is accurate enough to make a prediction. The criteria for the decision is based on the Mean Squared Error or MSE, which is given as:

$$MSE = \frac{1}{N} \sum_{i=1}^{N} (f_i - y_i)^2 \tag{81}$$

where N is the number of data points, f_i is the value returned by the model, and y_i is the actual value for data point i.

Multiple Decision Trees are used together in a random forest algorithm along with a statistical technique of ensemble learning called "bagging" which is a way to decrease the variance in the prediction by generating additional data for training using combinations with repetitions to produce multiple sets of the original data. By combining the information from each decision tree the random forest generates an ensemble model, which then predicts the final output. It is better than single decision trees as it reduces over-fitting.

- Extreme Gradient Boosting [127]: Similar to bagging, another type of ensemble learning technique is called "boosting". It uses weighted averages in an iterative way. Similar to other gradient boosting algorithms, Extreme Gradient Boost also tries to reduce the MSE. The main feature of Extreme Gradient Boosting is in its ability to penalize the complexity of trees.

Random Forest regression and Extreme Gradient Boosting has been previously used by Zhou *et al.* [112] in predicting flow condensation heat transfer coefficient in mini/micro-channel. They showed that both these methods provide accurate results. There are five hidden layers between the input and the output layer. The number of neurons in the 5 hidden layers are set to 1000, 500, 250, 100, and 50. We tested different combinations of number of layers, neurons, epochs, value of learning rate, for hyper-parameter tuning. The reported model provided the optimum results, hence this architecture was chosen for the study. All codes were developed using Python programming language on Tensorflow [128] and Keras [129] framework using Sci-kit learn [130] package.

Description of Data

The original 12-parameter dataset which is used to predict the heat-flux is denoted as DATASET-A, and the reduced data-set which uses 3 non-dimensional Π terms to predict the fourth non-dimensional heat-flux term as DATASET-B.

For DATASET-A, we consolidated 231 data points from multiple publications, namely: Dhir (2005) [10], Oka *et al.*(1995) [131], Merte *et al.*(1996) [132], Straub *et al.*(2001) [133], Raj *et al.*(2012) [17], and Warrier *et al.*(2015) [18]. Details about the dataset are provided in table 5. It should be noted that only ranges of features pertinent to experimental conditions are provided in the table. Other features which include the fluid properties are not included since they are constant values for each liquid.

These data points cover 12 parameters with a wide range: 5 different gravity values (ranging from earth gravity to micro-gravity), 10 different liquid sub-cooling values, 5 different surface roughness values, 230 different wall superheat values (where negative wall superheat signifies natural convection stage of the boiling curve) and 4 different liquids which includes water, perfluoro-n-hexane, CFC-113 and n-pentane. Out of the 231 samples, a random $80\% - 20\%$ split was made for training data and testing data respectively. On the training set data, a further validation split of $80\% - 20\%$ was applied. Data was scaled using the standard scaling equation:

$$z = (x - \mu)/s \tag{82}$$

where z is the scaled output, x is the input prior to scaling, μ is the mean, and s is the standard deviation. The 12 parameters are given in table 6 with their respective symbols and units. The details pertaining to the highlighted portions and the column named "Contribution" in table 6 has been discussed later in the chapter.

Range of variables	**Dhir (2005) [10]**	**Warrier *et al.* (2015) [18]**	**Raj *et al.* (2012) [17]**	**Straub *et al.* (2001) [133]**	**Merte *et al.* (1996) [132]**	**Oka *et al.* (1995) [131]**	**Total**
Heatflux (W/m^2)	1439 - 115,895	40 - 39,300	3230 - 391,300	106,440 - 404,000	9430 - 80,700	4826 - 221,171	40 - 404,000
Gravity (m/s^2)	0.098 - 9.8	2.45E-7 - 9.8	9.8E-6 - 9.8	9.8E-4 - 9.8	9.8E-4 - 9.8	9.8E-2 - 9.8	2.45E-7 - 9.8
Wall superheat ($^\circ C$ **or** K)	6- 12	-15.8 - 11.7	14.1 - 39.1	10.6 - 40.4	11.3 - 39.8	3.04 - 54.26	-15.88 - 54.26
Liquid subcooling ($^\circ C$ **or** K)	0	10.55	11	17	11	3 - 19	0 - 19
Surface roughness (μ**-m**)	8.5	16.3	1	NA(0)	NA(0)	0.1	0 - 16.3
System pressure (KPa)	101.32	125	101	102	150	101.3	101 - 150
Number of Samples	10	19	17	9	9	167	231
Liquid	Water	pfnh / FC72	pfnh / FC72	R113	R113	n-pentane R113, Water	Water, pfnh, R113, n-pentane

Table 5. Range of values from each source

8 parameters selected for dimensional analysis based on feature importance study

Parameter	Symbol	Units	Contribution
Heat flux	$\dot{q}$	W/m^2	Prediction variable
Wall Superheat	ΔT_w	K	40%
Gravity	g	m/s^2	28%
Liquid subcooling	ΔT_{sub}	K	22%
Vapor Density	ρ_v	Kg/m^3	3%
Thermal Conductivity	κ_l	W/mK	2%
Surface Tension	σ	N/m	1%
Liquid Density	ρ_l	Kg/m^3	1%
Dynamic Viscosity of Liquid	μ	$N-s/m^2$	1%
Specific Heat Capacity of Liquid	c_p	J/KgK	1%
Surface Roughness	r	μm	1%
Latent Heat of Vaporization	L	J/Kg	0%
System Pressure	P	Pa	0%

4 parameters selected as repeating variables

Table 6. 12 parameters from the original dataset

A flowchart of the entire parameter reduction procedure is provided in figure 44.

Feature Importance study

A deeper look at Dataset-A shows that we have 12 different parameters which are used in predicting one parameter. This means the model has twelve degrees of freedom. It can be problematic to train an ANNs model with 12 parameters but less than 200 data points. Hence, with the goal of reducing the number of parameters we first perform a feature importance study. We use four feature selection techniques: one from each of the wrapper, filter and embedded methods, and one additional manual wrapper method based on ANNs model prediction result.

We first report the results for the manual wrapper method. The ANNs prediction is used as the basis for this method. Here, 'Mean Absolute Percent Error' (MAPE)

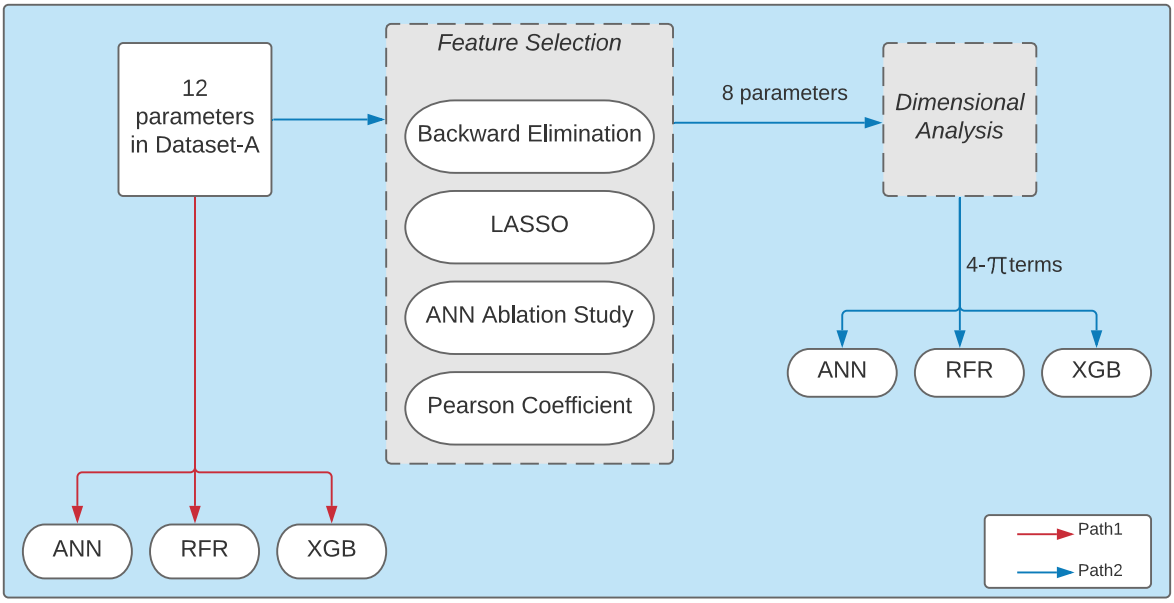

Figure 44. Flowchart of parameter reduction

value is treated as the error metric, it is calculated as:

$$MAPE = \frac{1}{n}\sum_{i=1}^{n}\left|\frac{A_i - F_i}{A_i}\right| \tag{83}$$

where A is the actual value, F is the predicted value and n is the number of samples predicted. In order to understand the contribution of each parameter, we perform an ablation study by following the below steps:

- Step 1: Run the ANNs model by training on all 12 parameters of Dataset-A. It reports a MAPE of 25.77% (Details are provided in section 3).
- Step 2: Remove one parameter and train the same model architecture on the remaining 11 parameters. Record the MAPE value as it indicates the significance of the parameter that was left out.
- Step 3: Add the previously left out parameter back and remove a different parameter and perform Step 2.
- Step 4: Repeat step 2 and 3 for all parameters.

- Step 5: Compare the MAPE values for each of the runs.

Based on the degree of change in MAPE, the effect of each parameter can be determined. Figure 45 shows the error between the MAPE in each case when one parameter is left out of the training set and the initial DATASET-A which include all parameters. This shows the effect of leaving out each parameter on the MAPE. Based on the results in figure 45, the percent contribution for each parameter was

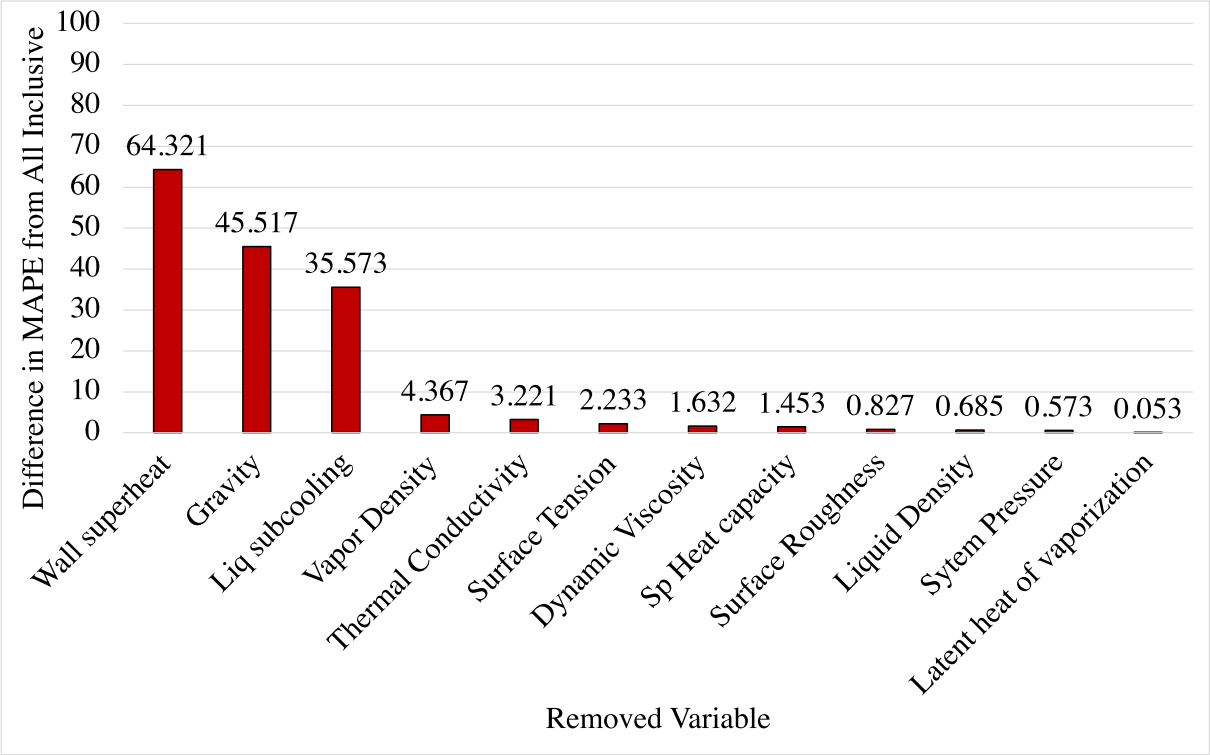

Figure 45. Feature Importance Study: Effect of leaving out one variable on MAPE using ANNs

calculated. The contribution of each parameter in order of decreasing significance and the most important eight parameters are highlighted in table 6 in the column named "Contribution".

Next, we perform a second feature importance study technique called Pearson Correlation [121]. This method determines the correlation between each variable

calculating the correlation coefficient, r:

$$r = \frac{\sum(x_i - \bar{x})(y_i - \bar{y})}{\sqrt{\sum(x_i - \bar{x})^2 \sum(y_i - \bar{y})^2}} \tag{84}$$

. Based on the correlation coefficient values for each variable in DATASET-A, a heatmap was generated which shows the degree of correlation among each variables in figure 46.

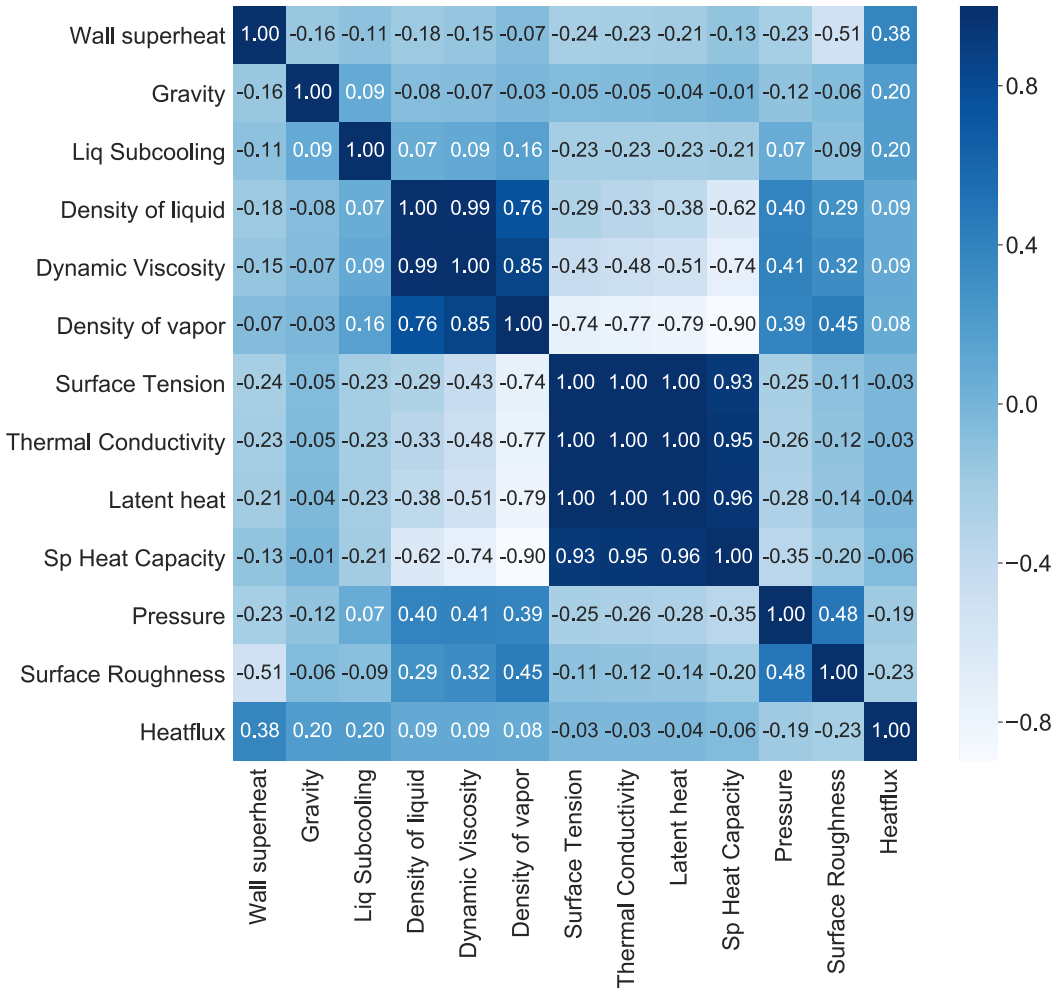

Figure 46. Feature Importance Study: Correlation Factor for Pearson Correlation

In figure 46, each cell reports the correlation factor between the two variables corresponding to the row and column that the cell belongs to. So, for the heat flux correlation, one should look at the right most column. The high correlation coefficient between density and viscosity is in agreement with the physics, since density is

linearly proportional to viscosity. Similarly, high coefficient values between thermal conductivity and latent heat of vaporization also makes sense in the nucleate boiling space as both these variables are related to the total heat coming into the liquid. Regarding the heat flux correlations, the results reported using Pearson Correlation technique is in good agreement to the ablation study reported earlier. Wall superheat, Gravity and Liquid subcooling are determined to be the three highest correlated variables with heat flux.

Out of the 5 parameters with 1% contribution, surface tension was selected due to to its significance in nucleate boiling heatflux [134], and since its percentage being a little higher than the other ones (which was rounded off to 1%). Liquid density was the other parameter selected to formulate density ratio between liquid and vapor densities as a dimension-less parameter in the dimensional analysis (details on dimensional analysis are described in section 2), since density ratio has been shown to be a significant parameter for nucleate boiling in other studies [10].

Additionally, we used two other feature importance study techniques, namely: Backward Elimination technique and the LASSO (Least Absolute Shrinkage and Selection Operator) technique. All methods report the same conclusion that **Wall Superheat, Gravity and Liquid subcooling** are the three most significant parameters in predicting nucleate boiling heat flux. Details about the Backward Elimination and the LASSO techniques are not included for brevity.

Effect of dimensional analysis

Based on the results from the feature importance study, we initially determined the three most significant parameters. So we start by training the ANNs model with the three significant parameters, namely: Wall Superheat, Gravity and Liquid subcooling. The MAPE reported by training the ANNs using only these 3 parameters was 68.32% which is much higher than the MAPE with 12 parameters of 25.77%. This shows that

3 parameters are not enough to construct an accurate functional mapping by ANNs. The model needs the effect of more parameters, with reduced number of parameters. So we select the eight most important parameters including heat flux to perform dimensional analysis [135] as highlighted in the black colored box in table 6 with the goal of reducing the number of parameters from 8 to 4 non-dimensional Π terms. Out of these eight, the parameters that were selected as repeating variables are highlighted in table 6 with violet cell background color. The Π terms generated as a result of performing dimensional analysis are shown in table 7.

Π_1	Π_2	Π_3	Π_4
$\frac{\Delta T_{sub}}{\Delta T_w}$	$\frac{g^{(1/4)}\sigma^{(5/4)}}{\kappa_l \Delta T_w \rho_v^{(1/4)}}$	$\frac{\rho_l}{\rho_v}$	$\log\left(\frac{g^{(9/4)}\rho_v^{(1/4)}}{\dot{q}\sigma^{3/4}}\right)$

Table 7. Π terms generated by dimensional analysis

3 Results and Discussion

Once the Π terms are generated, the next step is to train the model using Π_1, Π_2 and Π_3 as input to predict the non-dimensional heat flux Π_4. Here a log function was used in Π_4 to reduce the range of the non-dimensional gravity values (microgravity is in the range of $\sim 1.0E-6 m/s^2$) and earth gravity is $\sim 9.8 m/s^2$). From the original Dataset-A we generate a new dataset Dataset-B which has the 4 non-dimensional Π terms and their values for the same 231 samples.

Model is trained based on Dataset-B, with only one change to the reported model in section 2. Since the log function was used in Π_4, it generated many negative values. Hence, to incorporate that, the 'ELU' activation function or Exponential Linear Unit instead of 'ReLU' was implemented. ELU unlike ReLU can produce

negative outputs. ELU is defined as:

$$f(x) = \begin{Bmatrix} x & x > 0 \\ \alpha \cdot (\exp(x) - 1) & x \leq 0 \end{Bmatrix} \tag{85}$$

where α is the scale for negative factor and is set to the default value of 1.0 in our code.

The results for the Π_4 predictions of 46 samples using ANNs are provided in figure 47. The Ground Truth values (actual Π_4 values) are plotted along the x-axis, and

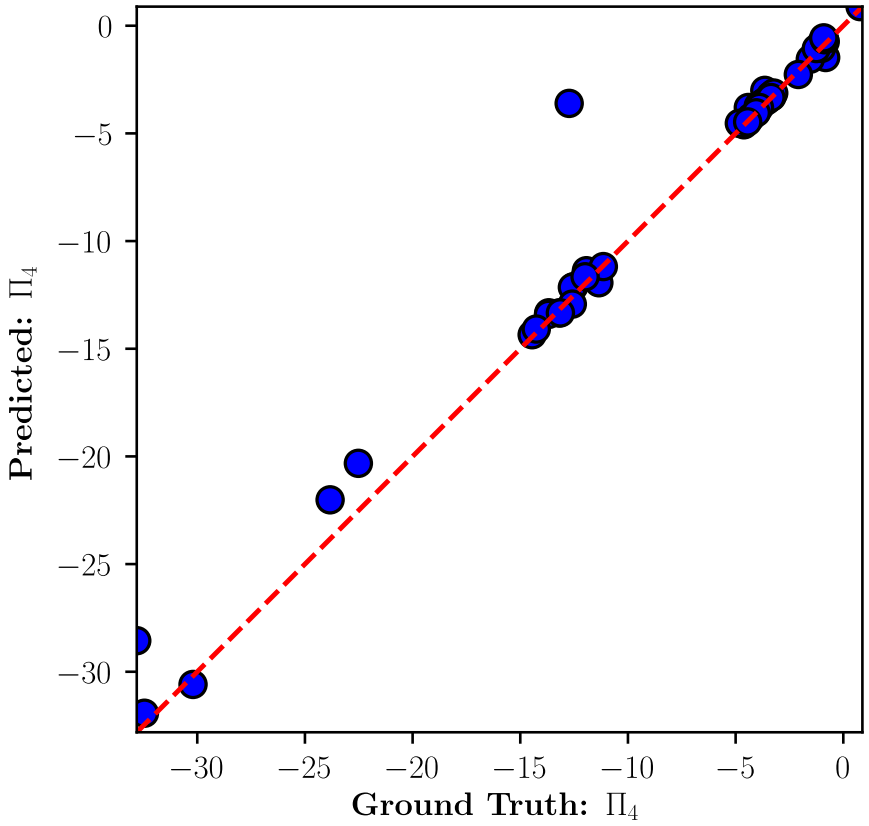

Figure 47. ANNs prediction for Π_4: DATASET-B

the model predictions are plotted along the y-axis. The points adhering closer to the center diagonal line passing through the origin depicts higher accuracy. The MAPE reported for ANNs model using non-dimensional Π terms is **9.12%**, which reduces

to 6.43% after removing 3 outlier predictions (the top 3 with the highest difference between predicted and actual results were chosen to be removed in this case).

Next, we compare results from different models that are trained based on different dataset. In section 3 we compare ANNs with Extreme Gradient Boost (XGB) and Random Forest-Regression (RFR) algorithm predictions using DATASET-B. In Section 3 we compare the prediction results with DATASET-A for ANNs and other machine learning models. In section 3, we provide the comparison of ANNs prediction with that of Rohsenow's correlation.

Comparison with other machine learning models

Two new models are trained using DATASET-B to predict non-dimensional heat flux Π_4. The predictions for Π_4 using XGB and RFR algorithms are provided in figure 48. The XGB model has an MAPE value of **16.31%** which is higher than 9.12% from the ANNs model. Random Forest-Regression reports a MAPE of **18.71%** which is higher than those from the ANNs model and the XGB model. MAPE for XGB prediction

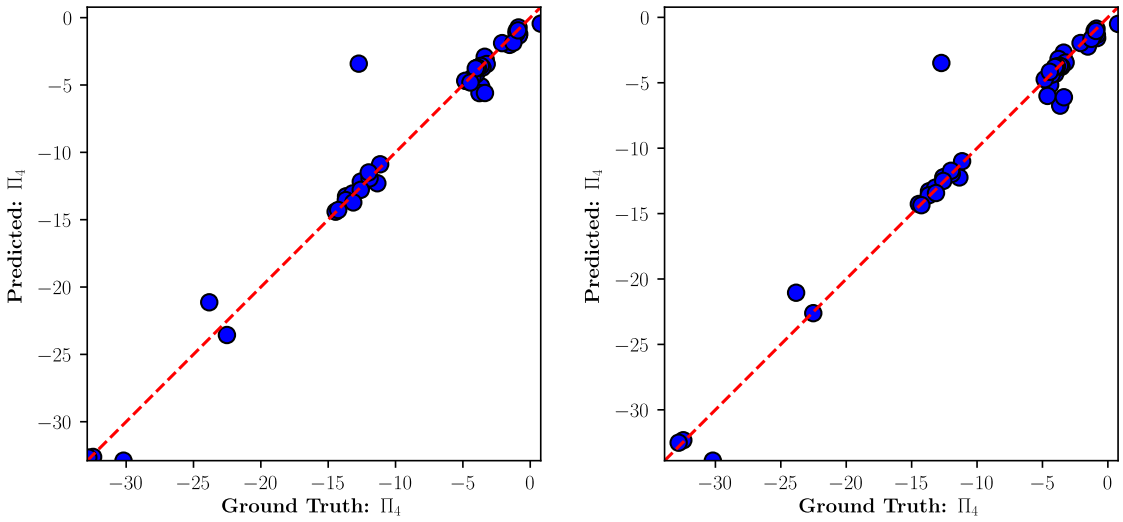

Figure 48. XGB (left) and RFR (right) predictions for Π_4: DATASET-B

for Π_4 using DATASET-B for 46 samples is **16.31%** which is higher than 9.12% of

ANNs.

Random Forest-Regression reports a MAPE of **18.71%** for Dataset-B which is higher than 9.12% of ANNs and 16.31% of XGB. As can be seen from figure 48, the predictions are very similar for both models with some minor differences.

Comparison with 12 parameter dataset predictions

To highlight the effectiveness of dimension reduction we compare results from the ANNs model trained using Dataset-A and from ANNs model trained using Dataset-B. Prediction was made over the testing dataset of 46 independent samples for Dataset-A. The results are shown in figure 49. In the case of Dataset-A, the

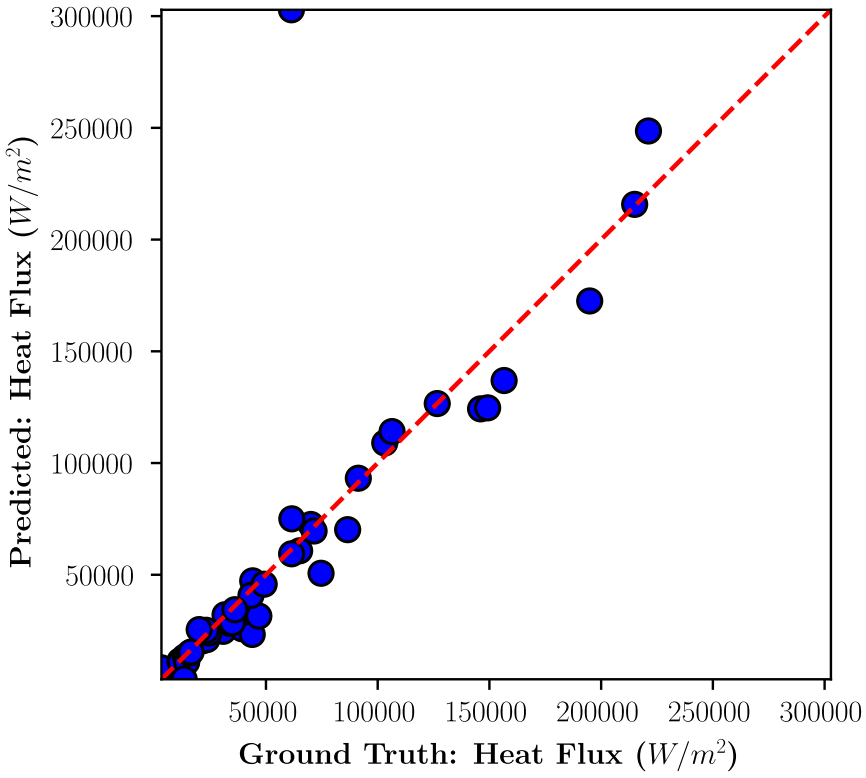

Figure 49. ANNs prediction for Heat flux: Dataset-A

MAPE value is **25.77%**. After excluding two outlier samples MAPE reduces to 14.4%. The outliers did not have any specific correlation, they are for different liq-

uids with different gravity, wall superheat and liquid subcooling values, indicating that the outliers do not conform to any specific type which the model is unable to predict correctly. In comparison, the prediction error for DATASET-B using ANNs was much lower at 9.12%.

Next, we provide the predictions from the XGB and RFR model for DATASET-A. Prediction was made over the testing data-set of 46 independent samples as in DATASET-B. The results for the XGB and RFR prediction are shown are shown in figure 50.

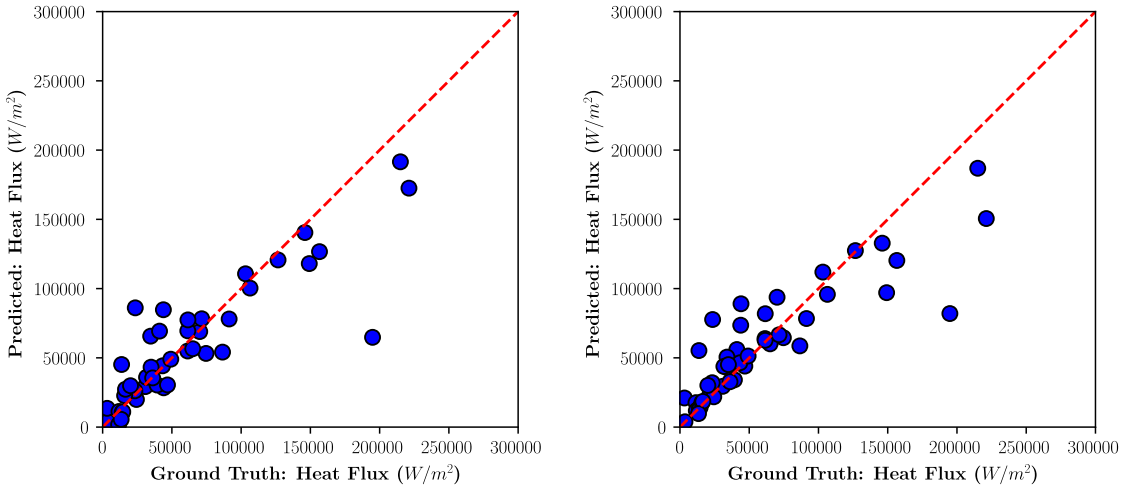

Figure 50. XGB (left) and RFR (right) predictions for Heat flux: DATASET-A

The corresponding MAPE values for XGB prediction for heat flux for DATASET-A is **42.19%** which is higher than the 25.77% of ANNs. In comparison, the prediction for DATASET-B using XGB was much lower at 16.31%.

For DATASET-A, RFR reports a MAPE of **44.20%** which is higher than 25.77% of ANNs and 42.19% of XGB. In comparison, the prediction for DATASET-B using RFR was much lower at 18.71%.

A comparison between figures 48 and 50 shows that the predictions for DATASET-B in figure 48 are much closer to the center line and hence more accurate than the

predictions for DATASET-A in figure 50. This can also be seen from the MAPE value comparisons.

A summary of the comparison of the MAPE values along with standard deviations of the MAPE for the machine learning models using both DATASET-A in predicting heat flux and DATASET-B in predicting Π_4 for the same 46 samples is provided in table 8. Here, the standard deviation, ϕ is calculated as:

$$\phi = \sqrt{\frac{\sum(x_i - \mu)^2}{N}} \tag{86}$$

where N is the number of the samples, x_i represents the values from the ith sample, and μ is the mean. The 46 samples were selected prior to the training process for all cases shown in table8. The selection process was completely random, however the same seed value was used for all methods so that the exact same samples are chosen to be included in the test set for all models. This would maintain a fair comparison for the predictive capabilities across the models.

Model	**Dataset-A**		**Dataset-B**	
	MAPE	**Standard Deviation**	**MAPE**	**Standard Deviation**
ANNs	25.77%	61.07	9.12%	16.28
XGB	42.19%	66.59	16.31%	28.49
RFR	44.20%	94.11	18.71%	32.95

Table 8. MAPE and standard deviation comparison of machine learning models for 46 samples using DATASET-A and DATASET-B

From the results in table 8 it is evident that the ANNs model reports the most accurate predictions for both DATASET-A and DATASET-B. The prediction for ANNs using the DATASET-B is considerably more accurate than that using DATASET-A. This trend holds true for XGB and RFR algorithms as well. This suggests that performing a feature importance study and dimensional analysis, which resulted in the reduction of the number of features to 3 from 12, improved the accuracy of models.

Analysis of Predictions:

Now we perform analysis to generate physically meaningful insights from the data.

Effect of gravity

The model learns the physics-based behavior from the data. This can be verified by considering the example of gravity and its effect on heat-flux. Typically experiments have shown that keeping other parameters constant, if gravity is reduced then a reduction in heatflux is observed ([17, 18, 132]). For the model prediction, we consider two sample points from the unseen test set. The two points are for the same liquid (pfnh) and uses all other parameters of similar value (including wall super heat of 21.5C), the only difference between the two datapoints is gravity value. One is microgravity, and one is earth gravity. The ground truth data for gravity and heatflux and the ANN model prediction of heatflux for the two points are shown in table 9.

Gravity (m/s^2)	**Actual Heatflux** (W/m^2)	**Predicted Heatflux** (W/m^2)	**Percent difference in MAPE**
9.8	215000	215755.34	0.35%
9.8E-6	30840	24687	19.94%

Table 9. Effect of gravity on heatflux

As can be seen from table 9, the ANN model predicts the trend of heatflux reducing with gravity. This trend has been verified by multiple experiments ([18,132,133]). The error for the earth gravity case is less than 1%. Although the error for the microgravity case is higher at 19.94%, this error is similar to the state-of-the-art scaling law model of Raj *et al.* [17] for microgravity conditions which provides an error of 20% for heat flux predictions. However, it should be noted that the scaling law model for [17] has been tested only for microgravity conditions. The ANN model predictions have

tested for all conditions. Additionally, the higher error for microgravity case can also be explained by the lower number of data points in microgravity conditions. With more experimental data available, the model accuracy could be further improved. This can be considered as part of a future work.

Effect of wall superheat

Next, we consider the effect of wall super heat on heatflux. From the unseen test set, we select 4 sample datapoints which are for the same test liquid (water) and uses all other parameters of similar values, the only difference is in the wall super heat values. Experiments have shown that heat-flux increases with wall-super heat, and this could be attributed to the additional supply of heat due to the increased temperature difference. The ground truth data for wallsuper heat and heatflux and the ANN model prediction of heatflux for the two points are shown in table 10.

Wall superheat (C)	**Actual Heatflux** (W/m^2)	**Predicted Heatflux** (W/m^2)	**Percent difference in MAPE**
10.88	31693.08	32111.77	1.32%
17.75	70102.91	72507.24	3.42%
20.21	103163.9	108982.7	5.64%
21.20	126648.9	126623.8	0.019%

Table 10. Effect of wall superheat on heatflux

As can be seen from table 10, the ANN model learns the behavior that heatflux increases with increase in wall superheat. Additionally, the accuracy of the model prediction is high which is evident from the low MAPE values. This shows that the model learns the behavior of individual parameters with heatflux and creates a universal functional mapping for all the parameters with heatflux.

Critical Heat Flux (CHF)

Rayleigh Taylor instabilities occurs when a fluid of low density is pushing or accelerating a fluid of higher density, it occurs due to continued acceleration, for which the velocity is significant. In case of boiling, Rayleigh-Taylor instability starts to have an effect when the heatflux is close to the CHF, and then continues through transitional boiling and later in film boiling ([136, 137]). This is due to the velocity of the vapor phase being higher during the transitional and film boiling phases. With increased heat flux density, the vapor phase abrupts the flow of fresh liquid onto the heater wall, and this leads to burn out [136]. To explore this, we first calculated the CHF (Critical Heat Flux) for all the datapoints in the dataset using Zuber's equation:

$$q_{CHF} = Ch_{fg}\rho_v \left[\frac{\sigma g(\rho_l - rho_v)}{\rho_v^2}\right]^{1/4} \tag{87}$$

Here C is constant with value of 0.149 for flat surfaces. We compared the calculated CHF values with the actual heatflux to see which data-points had reached CHF. It was determined that out of the 231 datapoints, only 27 datapoints had reached the CHF value. 18 out of those 27 were for reduced gravity or microgravity conditions. Out of those 27 datapoints, 5 datapoints were part of the randomly chosen test dataset which is unseen to the ANN model. Next, we check the ANN model's prediction accuracy for the cases where CHF was reached. In order to do that, we provide the results of the actual heatflux, predicted heatflux and MAPE for those 5 datapoints in table 11.

As can be seen from the table, that the average MAPE is about 15.36% for cases where the CHF was reached, hence the model is able to predict cases of nucleate boiling which are at the border of transition boiling, and start of Rayleigh-Taylor instability could be observed with reasonable accuracy. For comparison, the MAPE

Actual Heatflux (W/m^2)	**Predicted Heatflux** (W/m^2)	**MAPE**	**Average MAPE**
30480	24687.87	19.94%	15.36%
44060	47285.84	7.32%	
215000	215755.34	0.35%	
146040	124243.13	14.92%	
39310	25835.61	34.27%	

Table 11. Effect of Rayleigh-Taylor instabilities

of the complete dataset was 25.77% which shows that the cases where CHF had been reached has a lower error.

Kuzma-Kichta *et al.*([138] investigated bubble interface oscillations during boiling using acoustic diagnostics and a laser method under subcooled liquid condition. They reported that the bubble surface oscillation causes a complex non-linear micro-convection of the liquid around the bubble, affecting heat transfer on a heated surface. This is in agreement with our ANN model prediction that Liquid Subcooling is one of the significant parameters on which heatflux depends.

Parameter significance

One of the key novel contributions of this work includes the quantification of the importance of each parameter in heatflux prediction. This quantification had been provided in table 6. In order to verify the claim that "the three most significant parameters for heatflux prediction in nucleate boiling are: Wall superheat, Gravity, Liquid subcooling", we performed a study. We trained the ANN-model only with these 3 parameters and compared the accuracy of this model with the complete dataset. A second study was performed to verify if the 7 parameters that we selected for the dimensional analysis can predict heatflux with reasonable accuracy. The comparison is provided in table 12.

MAPE-3 parameter dataset	MAPE-7 parameter dataset	MAPE-12 parameter dataset
3.77	26.54	25.77

Table 12. MAPE comparison between 3-parameter (most significant inputs), 7-parameter (the parameters chosen for dimensional analysis), and the complete dataset with 12 -parameter

It is expected that the MAPE for the 12 parameter dataset to be lower than the 3 parameter and 7-parameter ones since it includes more information. The percentage difference between the 12-parameter MAPE with the 3-parameter one is about 16%, which shows that the contribution of the top 3 parameters is about 84%. The MAPE for the 7-parameter dataset is closer to the 12 parameter one than the 3-parameter one since it contains more relevant information. The 7 parameter dataset has a percentage difference of 2.9% from the 12-parameter one. This shows that the contribution of these seven parameters combined, namely: Wall superheat, Gravity, Liquid subcooling, Vapor density, Thermal conductivity, Surface tension, and liquid density is about 97% in the prediction of heatflux.

Boiling regimes

In order to explore the effect of different boiling regimes, we quantify the percentage contribution of the variables in both Surface Tension Dominated Boiling (SDB) and Buoyancy Dominated Boiling (BDB) regimes. Based on the threshold value of $L_h/L_c > 2.1$ for BDB and $L_h/L_c < 2.1$ for SDB, where L_h is the heater size, and $L_s = \sqrt{\frac{\sigma}{g(\rho_l - \rho_v)}}$ as proposed by Raj *et al.*(2010) [139], our dataset includes 60 datapoints in the SDB regime and remaining 171 datapoints in the BDB regime. We determine the contribution of each parameter by calculating the MAPE difference between (a) prediction from ANN model trained using complete dataset and (b) prediction from ANN model trained by removing that particular parameter which would show the contribution of the specific parameter. The MAPE thus calculated is based

on the test cases of either only SDB regime or only BDB regime. Based on the equation of L_s, surface tension, gravity, and densities of liquid and vapor are significant for the regimes, we provide the contribution of those parameters in table:

Variables	**Contribution percentage in SDB**	**Contribution percentage in BDB**
Gravity	0.96%	22.78%
Surface Tension	44.86%	0.57%
Liquid and Vapor Density	4.97%	1.62%

Table 13. Parameter significance for different boiling regimes

The results in table 13 quantify the effect of gravity and surface tension in the SDB and BDB regimes. The higher percentage contribution of Surface Tension in the SDB regime and lower in the BDB regimes shows that surface tension is a key parameter in SDB regime. Similarly, gravity is a key parameter in BDB regime. This can also be verified with the physics behind the problem, as gravity is reduced, buoyancy reduces, and surface tension effect becomes stronger. With continued reduction in gravity, surface tension becomes the dominant parameter. The contribution of gravity in SDB regime is almost non-existent, this was also reported by Raj *et al.* [17,139] from their experiments. Additionally, the model predictions also highlight that surface tension and liquid subcooling are the two most significant parameters in SDB regime with a combined contribution of 60%. Similarly, wall superheat and gravity are the two most significant parameters in BDB regime, with a combined contribution of 72%.

Comparison with Rohsenow's Correlation

Next, we compare ANNs predictions against predictions from the well-known correlation originally proposed by Rohsenow (1952) [8] and later improved by Liaw and Dhir (1989) [85]. Out of the 46 samples contact angle information was available for only 22 samples. So, we used those 22 samples to calculate the heat flux using the correlation. We also calculate the MAPE for ANNs using Dataset-B for those 22 samples in order to have a fair comparison with Rohsenow's correlation. Results of the experimental heat flux, Rohsenow's prediction, and the ANNs predictions are shown in figure 51.

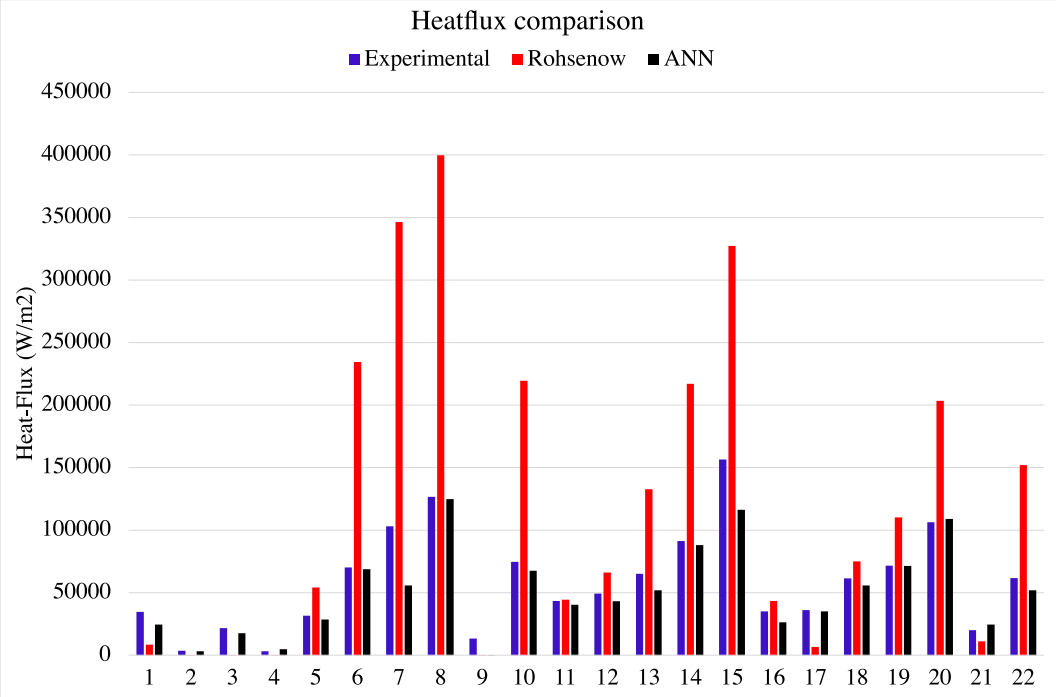

Figure 51. Comparison of heat flux between Experimental, Rohsenow's Correlation and Predictions from ANNs based on 22 samples

It is evident in figure 51, that ANNs predictions are much closer to the experimental values than Rohsenow's correlation. In order to quantify the differences the MAPE values along with the standard deviation of the MAPE using Dataset-B for 22 samples of ANNs and Rohsenow's correlation are reported in table 14.

Model	MAPE	Standard Deviation
ANNs	19.07%	22.46
Rohsenow	103.48%	67.18

Table 14. MAPE and standard deviation comparison of ANNs (heat flux calculated from Π_4) and Rohsenow correlation for 22 samples for heat flux prediction

Results in table 14 show that that ANNs prediction with Dataset-B outperforms Rohsenow's correlation to a considerable extent. The overall conclusion for the results using the 22 samples in table 14 is similar to that of the 46 samples reported in table 8. It confirms that ANNs using Dataset-B: (i) Outperforms its own predictions of Dataset-A, (ii) Outperforms other machine learning models using both Dataset-A and Dataset-B and (iii) Outperforms Rohsenow's correlation.

CHAPTER VI

CONCLUSIONS

An adaptive Moment of Fluid method has been used to perform numerical simulations of nucleate boiling of water vapor bubble in a pool of test liquid (water) under different heat transfer conditions. Comparison of results of single bubble dynamics especially bubble growth rate, departure radius, and departure time has been made with different results. Validation with analytical solution of Scriven (1959) for bubble growth in super-heated liquid under absence of wall heat transfer is reported as the first case. Details of this case has also been compared with the numerical model of Sato and Ničeno (2013). The MoF results are in good agreement (with less than 5% error) with the previous published theoretical and numerical results. MoF results provide better results in comparison to that by Sato and Ničeno (2013), specifically for the bulging in the shape of the thermal layer. Next, the bubble growth is simulated in presence of a heater wall and under earth gravity conditions. Results for this simulation has been compared to both experimental as well as numerical solutions of Dhir *et al.*(2001). The MoF simulations are in a better agreement with the experimental solution than the numerical ones of Dhir *et al.*(2001) (about 5% lower error than Dhir *et al.*model), which validates the MoF model results to be more accurate. Next, bubble growth in super-heated liquid with wall-heat transfer is performed under reduced gravity conditions and compared with experimental solutions of Siegel & Keshock (1964). The MoF results for the reduced gravity simulations also provide good agreement for the growth rate in comparison to experiments performed via a drop tower. MoF simulations are performed for micro-gravity conditions with perfluoro-n-hexane as the test liquid, in comparison to results from experiments on the

ISS performed by Dhir *et al.*(2012). Results for the micro-gravity simulations suggests that the contribution of the micro-layer would be important in the micro-gravity case as the numerical simulations get a good match with the growth rate only at a higher wall-super heat, which means for the experimental value, the micro-layer contribution needs to be included. A new method is proposed for estimating the bubble diameter at different gravity levels. This method is based on an analysis of empirical data at different gravity values and using power-series curve fitting to obtain a generalized bubble growth curve irrespective of the gravity value. This method is shown to provide a good estimate of the bubble diameter for a specific gravity value and time.

A review of the existing micro-layer models in the literature is presented, along with the disadvantages each of them entails. Specifically, the contact line model used by the Dhir group which was introduced by Stephan and Busse (1992), and later modified by Son *et al.*(1999), uses constant micro-layer with no depletion considered, which does not reflect actual process. The model further assumes micro-layer length to be only for a small portion of the bubble base, and not the larger radial extent as found experimentally. The micro-layer thickness is restricted to be in the order of one cell size. Next, the whole micro-layer model proposed by Sato and Ničeno (2015), is restricted for test liquid water in earth gravity as it uses empirical coefficients to calculate thickness. It also requires additional sub-grid scheme to be implemented for the micro-layer model. This model additionally does not take into consideration the fact that in micro-gravity experiments the growth rate is typically found to be $\approx t^{1/3}$ at the later stages, instead of $\approx t^{1/2}$ in earth gravity, where t is the time. A novel depletable micro-layer approach is proposed for micro-gravity conditions using perfluoro-n-hexane as the test liquid which maintains the $t^{1/3}$ growth rate towards the later stages as seen in ISS experiments and addresses all the disadvantages of the existing models. The approach calculates the micro-layer thickness based on bubble base radius and time at each time-step. Depletion of the model is calculated by

subtracting the evaporation term. Additional Sub-grid scale modeling is not required as the approach calculates the vapor volume flux into the bubble from the micro-layer and distributes it across the cells which comprises the micro-layer region. Heat-flux, bubble growth rate, velocity vector and bubble shape results at different time instants are provided. All the reported results provide good agreement with experiments performed on ISS as reported by Dhir *et al.*(2012) which validates the approach.

Additionally a data-driven model is used to predict the nucleate boiling heat-flux under different conditions. Experimental data from multiple experiments under varying conditions of wall-superheat, liquid sub-cooling, surface roughness, and gravity for different liquids have been collected. The predictions show that the datadriven ANNs based model is higher in terms of accuracy than previous state of the art models. The best published model so far is the Liaw and Dhir's modified equation of Rohsenow's correlation. The model provides a MAPE of about 102% for 46 independent sample points. Our ANN based model has a MAPE of only 9%, which is 10 times more accurate than the current available models. The work also quantifies the significance percentage of each parameter on which the nucleate boiling heat flux depends. Earlier work had discussed the roles of many parameters in boiling. However, the quantification of these parameters has not been reported as per the author's knowledge. The current work would help researchers to determine the parameters to reject with minimum loss in accuracy.

We provide quantified percentage contribution of the significant variables in the SDB and BDB regimes of nucleate boiling. The key highlight of these results is that surface tension and liquid subcooling are the most significant parameters in SDB regime with a combined contribution percentage of 60%, while wall superheat and gravity are the most significant parameters in BDB regime with a combined contribution percentage of 70%. Most of prior studies using deep learning did not consider variation in gravity. One of the studies did consider gravity, however they considered

only four input parameters: wall superheat, gravity, surface tension, pressure. They did not consider liquid subcooling, vapor and liquid densities, thermal conductivity and other parameters which are shown to be significant in the feature importance study presented in this work. Our work uses deep learning to create a model for nucleate boiling heat flux with a comprehensive set of all of the significant input parameters including gravity for five different test liquids. These were determined based on results from four different feature importance techniques. We propose a new way to handle challenges of small dataset in deep learning. Training a model of a large number of features on a small dataset could reduce the model accuracy. To solve that problem, we propose to use a combination of feature selection techniques and dimensional analysis to reduce the number of input parameters by creating non-dimensional π-terms from the most significant input parameters and then use these π-terms as input. This helps in keeping the information of each variable intact, and yet reducing the number of parameters to aid in model convergence and increasing model accuracy. The reduction in error using this methodology has been highlighted as well.

They key conclusions from this work are:

- MoF method simulations for nucleate boiling has been performed. Simulation results in earth gravity, and reduced gravity are in good agreement with experiments.

- A data-driven technique for prediction of effect of gravity on bubble growth rate shows accurate prediction of bubble diameter in different gravity levels.

- A novel depletable microlayer approach for microgravity is proposed, results for bubble growth rate, bubble shape, and heat-flux are comparable to experiments performed on ISS.

- A novel data-driven technique has been used for heatlfux prediction. ANN outperforms XGB, RFR and Rohsenow correlation in heatflux prediction.
- Dimensional Analysis and Feature Importance techniques help in reducing ANN error from 25.7% to 9.12%.
- Gravity, Wall super heat, and Liquid subcooling are the three most significant parameters in heatflux prediction.
- Novel results of quantification of parameter contribution in each boiling regime reported, and it shows that ANN can learn and predict physics (effect of parameters and boiling regimes).

A larger dataset could provide lower error and hence a more robust model. This could be considered as a part towards future work. Additionally, the extension of the microlayer model could be explored as a future work for a general case irrespective of the gravity level.

REFERENCES

[1] "Transport phenomena in multiphase systems," in "Transport Phenomena in Multiphase Systems," , A. Faghri and Y. Zhang, eds. (Academic Press, Boston, 2006), p. iii.

[2] G. Li, Y. Lian, and M. Sussman, "Simulations of gas-liquid two-phase jet flows using the moment of fluid method," Fluids Engineering Division Summer Meeting, Symposia: Gas-Liquid Two-Phase Flows **1C** (2013).

[3] Y. Sato and B. Ničeno, "A sharp-interface phase change model for a mass-conservative interface tracking method," Journal of Computational Physics **249**, 127 – 161 (2013).

[4] V. K. Dhir, "Numerical simulations of pool-boiling heat transfer," AIChE Journal **47**, 813–834 (2001).

[5] R. Siegel and E. G. Keshock, "Effects of reduced gravity on nucleate boiling bubble dynamics in saturated water," AIChE Journal **10**, 509–517 (1964).

[6] G. Son, V. K. Dhir, and N. Ramanujapu, "Dynamics and Heat Transfer Associated With a Single Bubble During Nucleate Boiling on a Horizontal Surface," Journal of Heat Transfer **121**, 623–631 (1999).

[7] V. K. Dhir, G. R. Warrier, E. Aktinol, D. Chao, J. Eggers, W. Sheredy, and W. Booth, "Nucleate Pool Boiling Experiments (NPBX) on the International Space Station," Microgravity Science and Technology **24**, 307–325 (2012).

[8] W. Rohsenow, "A method of correlating heat transfer data for surface boiling liquids," Trans. ASME **74** (1952).

[9] K. Stephan and M. Abdelsalam, "Heat-transfer correlations for natural convection boiling," International Journal of Heat and Mass Transfer **23**, 73 – 87 (1980).

[10] V. K. Dhir, "Mechanistic Prediction of Nucleate Boiling Heat Transfer–Achievable or a Hopeless Task?" Journal of Heat Transfer **128**, 1–12 (2005).

[11] W. Fritz, "Maximum volume of vapor bubbles," Phys.Z **36**, 379–384 (1935).

[12] D. Gorenflo, V. Knabe, and V. Bieling, "Bubble density on surfaces with nucleate boiling-its influence on heat transfer and burnout heat flux at elevated saturation pressures," in "International Heat Transfer Conference Digital Library," (Begel House Inc., 1986).

[13] A. Kundan, T. T. T. Nguyen, J. L. Plawsky, P. C. Wayner, D. F. Chao, and R. J. Sicker, "Condensation on highly superheated surfaces: Unstable thin films in a wickless heat pipe," Phys. Rev. Lett. **118**, 094501 (2017).

[14] R. Siegel and C. Usiskin, "A Photographic Study of Boiling in the Absence of Gravity," Journal of Heat Transfer **81**, 230–236 (1959).

[15] D. M. Qiu, V. K. Dhir, D. Chao, M. M. Hasan, E. Neumann, G. Yee, and A. Birchenough, "Single-bubble dynamics during pool boiling under low gravity conditions," Journal of Thermophysics and Heat Transfer **16**, 336–345 (2002).

[16] O. Kannengieser, C. Colin, and W. Bergez, "Pool Boiling with Non-condensable Gas in Microgravity: Results of a Sounding Rocket Experiment," Microgravity Science and Technology **22**, 447–454 (2010).

[17] R. Raj, J. Kim, and J. McQuillen, "Pool Boiling Heat Transfer on the International Space Station: Experimental Results and Model Verification," Journal of Heat Transfer **134** (2012).

[18] G. R. Warrier, V. K. Dhir, and D. F. Chao, "Nucleate pool boiling experiment (npbx) in microgravity: International space station," International Journal of Heat and Mass Transfer **83**, 781 – 798 (2015).

[19] C. M. Usiskin and R. Siegel, "An Experimental Study of Boiling in Reduced and Zero Gravity Fields," Journal of Heat Transfer **83**, 243–251 (1961).

[20] *Pool Boiling in a Reduced Gravity Field*, vol. 1.

[21] J.-F. Zhao, J. Li, N. Yan, and S.-F. Wang, "Bubble Behavior and Heat Transfer in Quasi-Steady Pool Boiling in Microgravity," Microgravity Science and Technology **21**, 175–183 (2009).

[22] R. C. Lee and J. E. Nydahl, "Numerical Calculation of Bubble Growth in Nucleate Boiling From Inception Through Departure," Journal of Heat Transfer **111**, 474–479 (1989).

[23] R. Mei, W. Chen, and J. F. Klausner, "Vapor bubble growth in heterogeneous boiling—ii. growth rate and thermal fields," International Journal of Heat and Mass Transfer **38**, 921 – 934 (1995).

[24] S. W. Welch, "Local simulation of two-phase flows including interface tracking with mass transfer," Journal of Computational Physics **121**, 142 – 154 (1995).

[25] *A Numerical Study of the Effect of Contact Angle on the Dynamics of a Single Bubble During Pool Boiling*, vol. Heat Transfer, Volume 7 of *ASME International Mechanical Engineering Congress and Exposition*.

[26] H. Abarajith, V. Dhir, G. Warrier, and G. Son, "Numerical simulation and experimental validation of the dynamics of multiple bubble merger during pool boiling under microgravity conditions," Annals of the New York Academy of Sciences **1027**, 235–58 (2004).

[27] S. Tanguy, M. Sagan, B. Lalanne, F. Couderc, and C. Colin, "Benchmarks and numerical methods for the simulation of boiling flows," Journal of Computational Physics **264**, 1 – 22 (2014).

[28] S.-W. Shin, S. I. Abdel-Khalik, and D. Jurić, "Direct three-dimensional numerical simulation of nucleate boiling using the level contour reconstruction method," (2005).

[29] J. Wu and V. K. Dhir, "Numerical Simulation of Dynamics and Heat Transfer Associated With a Single Bubble in Subcooled Boiling and in the Presence of Noncondensables," Journal of Heat Transfer **133** (2011).

[30] G. Son and V. K. Dhir, "Numerical simulation of film boiling near critical pressures with a level set method," (1998).

[31] F. Gibou, L. Chen, D. Nguyen, and S. Banerjee, "A level set based sharp interface method for the multiphase incompressible navier–stokes equations with phase change," Journal of Computational Physics **222**, 536 – 555 (2007).

[32] S. Tanguy, T. Ménard, and A. Berlemont, "A level set method for vaporizing two-phase flows," Journal of Computational Physics **221**, 837–853 (2007).

[33] E. Can and A. Prosperetti, "A level set method for vapor bubble dynamics," Journal of computational physics **231**, 1533–1552 (2012).

[34] S. O. Unverdi and G. Tryggvason, "A front-tracking method for viscous, incompressible, multi-fluid flows," (1992).

[35] D. Juric and G. Tryggvason, "Computations of boiling flows," International journal of multiphase flow **24**, 387–410 (1998).

[36] S. W. Welch and J. Wilson, "A volume of fluid based method for fluid flows with phase change," Journal of computational physics **160**, 662–682 (2000).

[37] K. Ghosh, A. Mukhopadhyay, S. Sen, and D. Sanyal, "An integral approach for predicting vapour film collapse and growth around a hot sphere in sub-cooled water," in "ASME International Mechanical Engineering Congress and Exposition," , vol. 47853 (2006), vol. 47853, pp. 409–415.

[38] M. Yuan, Y. Yang, T. Li, and Z. Hu, "Numerical simulation of film boiling on a sphere with a volume of fluid interface tracking method," International Journal of Heat and Mass Transfer **51**, 1646–1657 (2008).

[39] J. B. Haelssig, A. Y. Tremblay, J. Thibault, and S. G. Etemad, "Direct numerical simulation of interphase heat and mass transfer in multicomponent vapour–liquid flows," International Journal of Heat and Mass Transfer **53**, 3947–3960 (2010).

[40] G. Tomar, G. Biswas, A. Sharma, and A. Agrawal, "Numerical simulation of bubble growth in film boiling using a coupled level-set and volume-of-fluid method," Physics of Fluids **17**, 112103 (2005).

[41] D. Jamet, O. Lebaigue, N. Coutris, and J. Delhaye, "The second gradient method for the direct numerical simulation of liquid–vapor flows with phase change," Journal of Computational Physics **169**, 624–651 (2001).

[42] A. Badillo, "Quantitative phase-field modeling for boiling phenomena," Physical Review E **86**, 041603 (2012).

[43] S. N.W. and D. Edward, "Post conference comments," Summary of Conference on Bubble Dynamics and Boiling Heat Transfer Held at the Jet Propulsion Laboratory **JPL Memo No. 20-137** (1956).

[44] M. Cooper and A. Lloyd, "The microlayer in nucleate pool boiling," International Journal of Heat and Mass Transfer **12**, 895 – 913 (1969).

[45] F. D. Moore and R. B. Mesler, "The measurement of rapid surface temperature fluctuations during nucleate boiling of water," AIChE Journal **7**, 620–624 (1961).

[46] R. C. Hendricks and R. R. Sharp, *Initiation of cooling due to bubble growth on a heating surface* (National Aeronautics and Space Administration, 1964).

[47] T. Yabuki and O. Nakabeppu, "Heat transfer mechanisms in isolated bubble boiling of water observed with mems sensor," International Journal of Heat and Mass Transfer **76**, 286 – 297 (2014).

[48] A. Urbano, S. Tanguy, G. Huber, and C. Colin, "Direct numerical simulation of nucleate boiling in micro-layer regime," International Journal of Heat and Mass Transfer **123**, 1128 – 1137 (2018).

[49] S. Jung and H. Kim, "An experimental study on heat transfer mechanisms in the microlayer using integrated total reflection, laser interferometry and infrared thermometry technique," Heat Transfer Engineering **36**, 1002–1012 (2015).

[50] Y. Utaka, Y. Kashiwabara, M. Ozaki, and Z. Chen, "Heat transfer characteristics based on microlayer structure in nucleate pool boiling for water and ethanol," International Journal of Heat and Mass Transfer **68**, 479 – 488 (2014).

[51] S. [van Stralen], M. Sohal, R. Cole, and W. Sluyter, "Bubble growth rates in pure and binary systems: Combined effect of relaxation and evaporation microlayers," International Journal of Heat and Mass Transfer **18**, 453 – 467 (1975).

[52] G. Smirnov, "Calculation of the initial thickness of the microlayer in nucleate boiling," Inzhenerno Fizicheskii Zhurnal **28**, 503–508 (1975).

[53] R. R. Olander and R. G. Watts, "An Analytical Expression of Microlayer Thickness in Nucleate Boiling," Journal of Heat Transfer **91**, 178–180 (1969).

[54] P. Wayner, Y. Kao, and L. LaCroix, "The interline heat-transfer coefficient of an evaporating wetting film," International Journal of Heat and Mass Transfer **19**, 487 – 492 (1976).

[55] P. Stephan and C. Busse, "Analysis of the heat transfer coefficient of grooved heat pipe evaporator walls," International Journal of Heat and Mass Transfer **35**, 383 – 391 (1992).

[56] Y. Sato and B. Ničeno, "A depletable micro-layer model for nucleate pool boiling," Journal of Computational Physics **300**, 20 – 52 (2015).

[57] S. Hänsch, S. Walker, and C. Narayanan, "Mechanistic studies of single bubble growth using interface-tracking methods," Nuclear Engineering and Design **321**, 230 – 243 (2017). Multi-scale multi-physics analysis of reactor transients in the NURESAFE project.

[58] S. Hänsch and S. Walker, "Microlayer formation and depletion beneath growing steam bubbles," International Journal of Multiphase Flow **111**, 241 – 263 (2019).

[59] G. Li, Y. Lian, Y. Guo, M. Jemison, M. Sussman, T. Helms, and M. Arienti, "Incompressible multiphase flow and encapsulation simulations using the moment-of-fluid method," International Journal for Numerical Methods in Fluids **79**, 456–490 (2015).

[60] M. Jemison, M. Sussman, and M. Arienti, "Compressible, multiphase semi-implicit method with moment of fluid interface representation," Journal of Computational Physics **279**, 182 – 217 (2014).

[61] M. Jemison, M. Sussman, and M. Shashkov, "Filament capturing with the multimaterial moment-of-fluid method," Journal of Computational Physics **285**, 149 – 172 (2015).

[62] L. Scriven, "On the dynamics of phase growth," Chemical Engineering Science **10**, 1 – 13 (1959).

[63] S. Banerjee, Y. Lian, Y. Liu, and M. Sussman, "A New Method for Estimating Bubble Diameter at Different Gravity Levels for Nucleate Pool Boiling," Journal of Heat Transfer **144** (2021). 021601.

[64] N. Kwatra, J. Su, J. T. Grétarsson, and R. Fedkiw, "A method for avoiding the acoustic time step restriction in compressible flow," Journal of Computational Physics **228**, 4146 – 4161 (2009).

[65] M. Sussman, A. S. Almgren, J. B. Bell, P. Colella, L. H. Howell, and M. L. Welcome, "An adaptive level set approach for incompressible two-phase flows," Journal of Computational Physics **148**, 81 – 124 (1999).

[66] M. Jemison, E. Loch, M. Sussman, M. J. Shashkov, M. Arienti, M. Ohta, and Y. Wang, "A coupled level set-moment of fluid method for incompressible two-phase flows," Journal of Scientific Computing **54**, 454–491 (2013).

[67] V. Dyadechko and M. Shashkov, "Moment-of-fluid interface reconstruction," (2005).

[68] M. Arienti and M. Sussman, "An embedded level set method for sharp-interface multiphase simulations of diesel injectors," International Journal of Multiphase Flow **59**, 1 – 14 (2014).

[69] Y. Lian, Y. Guo, and A. Work, "Numerical simulation of supercooled large droplets using the moment of fluid method," 52nd AIAA Aerospace Sciences Meeting - AIAA Science and Technology Forum and Exposition, SciTech 2014 (2014).

[70] Y. Lian, Y. Guo, A. Work, and M. Sussman, "Multiphase flow simulation using moment of fluid method," The 8th International Conference on Computational Fluid Dynamics, Chengdu, Sichuan, P.R. China (2014).

[71] G. Weymouth and D. K.-P. Yue, "Conservative volume-of-fluid method for free-surface simulations on cartesian-grids," Journal of Computational Physics **229**, 2853 – 2865 (2010).

[72] J. Brackbill, D. Kothe, and C. Zemach, "A continuum method for modeling surface tension," Journal of Computational Physics **100**, 335 – 354 (1992).

[73] A. Urbano, S. Tanguy, G. Huber, and C. Colin, "Direct numerical simulation of nucleate boiling in micro-layer regime," International Journal of Heat and Mass Transfer **123**, 1128–1137 (2018).

[74] A. Guion, S. Afkhami, S. Zaleski, and J. Buongiorno, "Simulations of microlayer formation in nucleate boiling," International Journal of Heat and Mass Transfer **127**, 1271–1284 (2018).

[75] G. Tryggvason and J. Lu, "Direct numerical simulations of flows with phase change," Procedia IUTAM **15**, 2 – 13 (2015). IUTAM Symposium on Multiphase Flows with Phase Change: Challenges and Opportunities.

[76] V. S. Ajaev, T. Gambaryan-Roisman, and P. Stephan, "Static and dynamic contact angles of evaporating liquids on heated surfaces," J of Colloid and Interface Science **342**, 550 – 558 (2010).

[77] A. Mukherjee and S. G. Kandlikar, "Numerical study of single bubbles with dynamic contact angle during nucleate pool boiling," International Journal of Heat and Mass Transfer **50**, 127 – 138 (2007).

[78] H. Jo, S. Kim, H. Kim, J. Kim, and M. H. Kim, "Nucleate boiling performance on nano/microstructures with different wetting surfaces," Nanoscale research letters **7**, 1–9 (2012).

[79] T.-S. Jiang, O. Soo-Gun, and J. C. Slattery, "Correlation for dynamic contact angle," J of colloid and interface science **69**, 74–77 (1979).

[80] S. F. Kistler, "Hydrodynamics of wetting," Wettability **6**, 311–430 (1993).

[81] S. Sikalo, C. Tropea, and E. Ganifá, "Dynamic wetting angle of a spreading droplet," Experimental Thermal and Fluid Science **29**, 795–802 (2005). Two Phase Flow.

[82] S. Banerjee, Y. Liu, M. Sussman, and Y. Lian, "Depletable micro-layer for nucleate boiling simulations in micro-gravity conditions: A new approach," International Journal of Heat and Mass Transfer **190**, 122642 (2022).

[83] A. Faghri and Y. Zhang, "Boiling," in "Fundamentals of Multiphase Heat Transfer and Flow," (Springer, 2020), pp. 469–534.

[84] S. Banerjee, Y. Lian, Y. Liu, and M. Sussman, "A new method for estimating bubble diameter at different gravity levels for nucleate pool boiling," J of Heat Transfer-Transactions of the ASME (2021).

[85] S.-P. Liaw and V. Dhir, "Void fraction measurements during saturated pool boiling of water on partially wetted vertical surfaces," J of Heat Transfer-Transactions of the ASME (1989).

[86] A. Voulodimos, N. Doulamis, A. Doulamis, and E. Protopapadakis, "Deep learning for computer vision: A brief review," Computational intelligence and neuroscience **2018** (2018).

[87] T. Young, D. Hazarika, S. Poria, and E. Cambria, "Recent trends in deep learning based natural language processing," ieee Computational intelligenCe magazine **13**, 55–75 (2018).

[88] P. Chatterjee, "Extracting Archival-Quality Information from Software-Related Chats," in "Proceedings of the 42nd International Conference on Software Engineering," (Association for Computing Machinery, New York, NY, USA, 2020), ICSE '20.

[89] P. Chatterjee, K. Damevski, and L. Pollock, "Automatic extraction of opinion-based q amp;a from online developer chats," in "2021 IEEE/ACM 43rd International Conference on Software Engineering (ICSE)," (2021), pp. 1260–1272.

[90] P. Chatterjee, K. Damevski, N. A. Kraft, and L. Pollock, "Automatically identifying the quality of developer chats for post hoc use," ACM Trans. Softw. Eng. Methodol. **30** (2021).

[91] P. Chatterjee, K. Damevski, N. A. Kraft, and L. Pollock, *Software-Related Slack Chats with Disentangled Conversations* (Association for Computing Machinery, New York, NY, USA, 2020), p. 588–592.

[92] P. Chatterjee, "Mining information from developer chats towards building software maintenance tools," Ph.D. thesis, University of Delaware (2021).

[93] S. Banerjee and Y. Lian, "Data driven covid-19 spread prediction based on mobility and mask mandate information," Applied Intelligence pp. 1–10 (2021).

[94] A. Jakaria, M. M. Hossain, and M. A. Rahman, "Smart weather forecasting using machine learning: a case study in tennessee," arXiv preprint arXiv:2008.10789 (2020).

[95] A. Alizadehdakhel, M. Rahimi, J. Sanjari, and A. A. Alsairafi, "Cfd and artificial neural network modeling of two-phase flow pressure drop," International Communications in Heat and Mass Transfer **36**, 850–856 (2009).

[96] K. Jambunathan, S. Hartle, S. Ashforth-Frost, and V. Fontama, "Evaluating convective heat transfer coefficients using neural networks," International Journal of Heat and Mass Transfer **39**, 2329–2332 (1996).

[97] J. Ling and J. Templeton, "Evaluation of machine learning algorithms for prediction of regions of high reynolds averaged navier stokes uncertainty," Physics of Fluids **27**, 085103 (2015).

[98] V. Rajendran, K. Y. Kelly, E. Leonardi, and K. Menzies, "Vortex detection on unsteady cfd simulations using recurrent neural networks," p. 3724 (2018).

[99] S. Singh and H. Abbassi, "1d/3d transient hvac thermal modeling of an off-highway machinery cabin using cfd-ann hybrid method," Applied Thermal Engineering **135**, 406–417 (2018).

[100] A. T. Mohan and D. V. Gaitonde, "A deep learning based approach to reduced order modeling for turbulent flow control using lstm neural networks," arXiv preprint arXiv:1804.09269 (2018).

[101] S. Banerjee, O. Ayala, and L.-P. Wang, "Direct numerical simulations of small particles in turbulent flows of low dissipation rates using asymptotic expansion," in "5th Thermal and Fluids Engineering Conference (TFEC)," (2020), pp. 659–668.

[102] S. Banerjee, *Turbulent collision statistics of cloud droplets at low dissipation rates* (University of Delaware, 2016).

[103] P. Naphon and T. Arisariyawong, "Heat transfer analysis using artificial neural networks of the spirally fluted tubes," Journal of Research and Applications in Mechanical Engineering **4**, 135–147 (2016).

[104] X. Guo, W. Li, and F. Iorio, "Convolutional neural networks for steady flow approximation," pp. 481–490 (2016).

[105] J.-X. Wang, J.-L. Wu, and H. Xiao, "Physics-informed machine learning approach for reconstructing reynolds stress modeling discrepancies based on dns data," Physical Review Fluids **2**, 034603 (2017).

[106] Y. Liu, N. Dinh, Y. Sato, and B. Niceno, "Data-driven modeling for boiling heat transfer: using deep neural networks and high-fidelity simulation results," Applied Thermal Engineering **144**, 305–320 (2018).

[107] M. Hassanpour, B. Vaferi, and M. E. Masoumi, "Estimation of pool boiling heat transfer coefficient of alumina water-based nanofluids by various artificial intelligence (ai) approaches," Applied Thermal Engineering **128**, 1208–1222 (2018).

[108] A. Mazzola, "Integrating artificial neural networks and empirical correlations for the prediction of water-subcooled critical heat flux," Revue Générale de Thermique **36**, 799–806 (1997).

[109] H. Alimoradi and M. Shams, "Optimization of subcooled flow boiling in a vertical pipe by using artificial neural network and multi objective genetic algorithm," Applied Thermal Engineering **111**, 1039–1051 (2017).

[110] G. Scalabrin, M. Condosta, and P. Marchi, "Modeling flow boiling heat transfer of pure fluids through artificial neural networks," International Journal of Thermal Sciences **45**, 643–663 (2006).

[111] Y. Qiu, D. Garg, L. Zhou, C. R. Kharangate, S.-M. Kim, and I. Mudawar, "An artificial neural network model to predict mini/micro-channels saturated flow boiling heat transfer coefficient based on universal consolidated data," International Journal of Heat and Mass Transfer **149**, 119211 (2020).

[112] L. Zhou, D. Garg, Y. Qiu, S.-M. Kim, I. Mudawar, and C. R. Kharangate, "Machine learning algorithms to predict flow condensation heat transfer coefficient in mini/micro-channel utilizing universal data," International Journal of Heat and Mass Transfer **162**, 120351 (2020).

[113] Y. Suh, R. Bostanabad, and Y. Won, "Deep learning predicts boiling heat transfer," Scientific reports **11**, 1–10 (2021).

[114] E. R. McClure and V. P. Carey, "Genetic algorithm and deep learning to explore parametric trends in nucleate boiling heat transfer data," Journal of Heat Transfer **143**, 121602 (2021).

[115] G. James, D. Witten, T. Hastie, and R. Tibshirani, *An introduction to statistical learning*, vol. 112 (Springer, 2013).

[116] N. El Aboudi and L. Benhlima, "Review on wrapper feature selection approaches," in "2016 International Conference on Engineering MIS (ICEMIS)," (2016), pp. 1–5.

[117] A. W. Whitney, "A direct method of nonparametric measurement selection," IEEE Transactions on Computers **100**, 1100–1103 (1971).

[118] T. Marill and D. Green, "On the effectiveness of receptors in recognition systems," IEEE transactions on Information Theory **9**, 11–17 (1963).

[119] S. Ding, "Feature selection based f-score and aco algorithm in support vector machine," in "2009 Second International Symposium on Knowledge Acquisition and Modeling," , vol. 1 (IEEE, 2009), vol. 1, pp. 19–23.

[120] S. Lee, Y.-T. Park, B. J. d'Auriol *et al.*, "A novel feature selection method based on normalized mutual information," Applied Intelligence **37**, 100–120 (2012).

[121] K. Pearson, "Notes on the history of correlation," Biometrika **13**, 25–45 (1920).

[122] R. Tibshirani, "Regression shrinkage and selection via the lasso," Journal of the Royal Statistical Society: Series B (Methodological) **58**, 267–288 (1996).

[123] A. E. Hoerl and R. W. Kennard, "Ridge regression: Biased estimation for nonorthogonal problems," Technometrics **12**, 55–67 (1970).

[124] L. Van Der Maaten, E. Postma, and J. Van den Herik, "Dimensionality reduction: a comparative," J Mach Learn Res **10**, 13 (2009).

[125] W. S. McCulloch and W. Pitts, "A logical calculus of the ideas immanent in nervous activity," The bulletin of mathematical biophysics **5**, 115–133 (1943).

[126] L. Breiman, "Random forests," Machine learning **45**, 5–32 (2001).

[127] T. Chen and C. Guestrin, "Xgboost: A scalable tree boosting system," in "Proceedings of the 22nd acm sigkdd international conference on knowledge discovery and data mining," (2016), pp. 785–794.

[128] M. Abadi, P. Barham, J. Chen, Z. Chen, A. Davis, J. Dean, M. Devin, S. Ghemawat, G. Irving, M. Isard, M. Kudlur, J. Levenberg, R. Monga, S. Moore, D. G. Murray, B. Steiner, P. Tucker, V. Vasudevan, P. Warden, M. Wicke, Y. Yu, and X. Zheng, "Tensorflow: A system for large-scale machine learning," in "Proceedings of the 12th USENIX Conference on Operating Systems Design and Implementation," (USENIX Association, USA, 2016), OSDI'16, p. 265–283.

[129] F. Chollet *et al.*, "Keras," `https://keras.io` (2015).

[130] F. Pedregosa, G. Varoquaux, A. Gramfort, V. Michel, B. Thirion, O. Grisel, M. Blondel, P. Prettenhofer, R. Weiss, V. Dubourg, J. Vanderplas, A. Passos, D. Cournapeau, M. Brucher, M. Perrot, and E. Duchesnay, "Scikit-learn: Machine learning in Python," Journal of Machine Learning Research **12**, 2825–2830 (2011).

[131] T. OKA, "Pool boiling of n-pentane, cfc-113 and water under reduced gravity: Parabolic flight experiments with a transparent heater," Trans. ASME, J. Heat Transfer **117**, 408 (1995).

[132] H. Merte Jr, H. Lee, and R. Keller, "Report on pool boiling experiment flown on sts-47 (pbe-ia), sts-57 (pbe-ib), and sts-60 (pbe-ic). final report," Tech. rep., Michigan Univ., Ann Arbor, MI (United States) (1996).

[133] J. Straub, "Boiling heat transfer and bubble dynamics in microgravity," Advances in Heat Transfer **35**, 57–172 (2001).

[134] A. Morgan, L. Bromley, and C. Wilke, "Effect of surface tension on heat transfer in boiling," Industrial & Engineering Chemistry **41**, 2767–2769 (1949).

[135] J. B. J. baron de Fourier, *Théorie analytique de la chaleur* (Firmin Didot, 1822).

[136] N. Zuber, "The hydrodynamic crisis in pool boiling of saturated and subcooled liquids," (1963).

[137] J. H. Lienhard and V. K. Dhir, *Extended hydrodynamic theory of the peak and minimum pool boiling heat fluxes*, vol. 2270 (National Aeronautics and Space Administration, 1973).

[138] Y. A. Kuzma-Kichta, A. Ustinov, and A. Ustinov, "Boiling investigation by laser and acoustic diagnostics method," in "3rd European thermal sciences conference (Heidelberg, 10-13 September 2000)," (2000), pp. 713–717.

[139] R. Raj and J. Kim, "Heater size and gravity based pool boiling regime map: transition criteria between buoyancy and surface tension dominated boiling," Journal of heat transfer **132** (2010).

APPENDIX: PERMISSION LETTERS

The work presented here has been published in the following peer-reviewed journal papers. The respective permission letters to include them in this dissertation has been included as well:

1. Banerjee, S., Lian, Y., Liu, Y. and Sussman, M., 2022. A New Method for Estimating Bubble Diameter at Different Gravity Levels for Nucleate Pool Boiling. Journal of Heat Transfer, 144(2). [84]

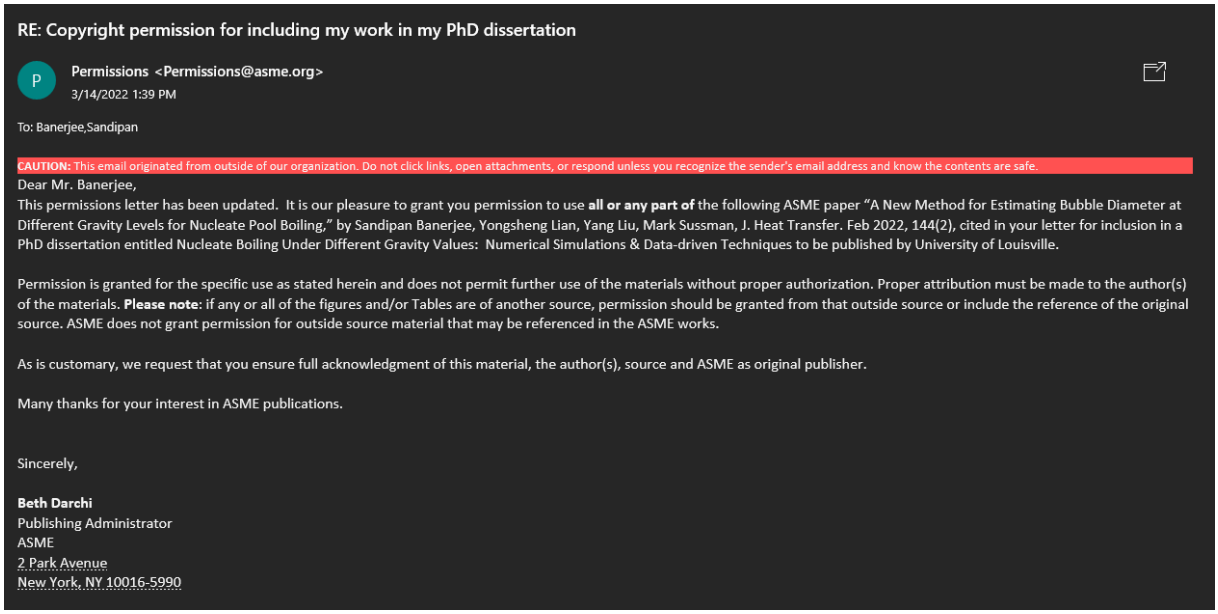

RE: Copyright permission for including my work in my PhD dissertation

Permissions <Permissions@asme.org>
3/14/2022 1:39 PM

To: Banerjee,Sandipan

CAUTION: This email originated from outside of our organization. Do not click links, open attachments, or respond unless you recognize the sender's email address and know the contents are safe.

Dear Mr. Banerjee,

This permissions letter has been updated. It is our pleasure to grant you permission to use **all or any part of** the following ASME paper "A New Method for Estimating Bubble Diameter at Different Gravity Levels for Nucleate Pool Boiling," by Sandipan Banerjee, Yongsheng Lian, Yang Liu, Mark Sussman, J. Heat Transfer. Feb 2022, 144(2), cited in your letter for inclusion in a PhD dissertation entitled Nucleate Boiling Under Different Gravity Values: Numerical Simulations & Data-driven Techniques to be published by University of Louisville.

Permission is granted for the specific use as stated herein and does not permit further use of the materials without proper authorization. Proper attribution must be made to the author(s) of the materials. **Please note**: if any or all of the figures and/or Tables are of another source, permission should be granted from that outside source or include the reference of the original source. ASME does not grant permission for outside source material that may be referenced in the ASME works.

As is customary, we request that you ensure full acknowledgment of this material, the author(s), source and ASME as original publisher.

Many thanks for your interest in ASME publications.

Sincerely,

Beth Darchi
Publishing Administrator
ASME
2 Park Avenue
New York, NY 10016-5990

Figure 1. Permission letter for 1st paper

2. Banerjee, S., Liu, Y., Sussman, M. and Lian, Y., 2022. Depletable micro-layer for nucleate boiling simulations in micro-gravity conditions: A new approach. International Journal of Heat and Mass Transfer, 190, p.122642. [82]

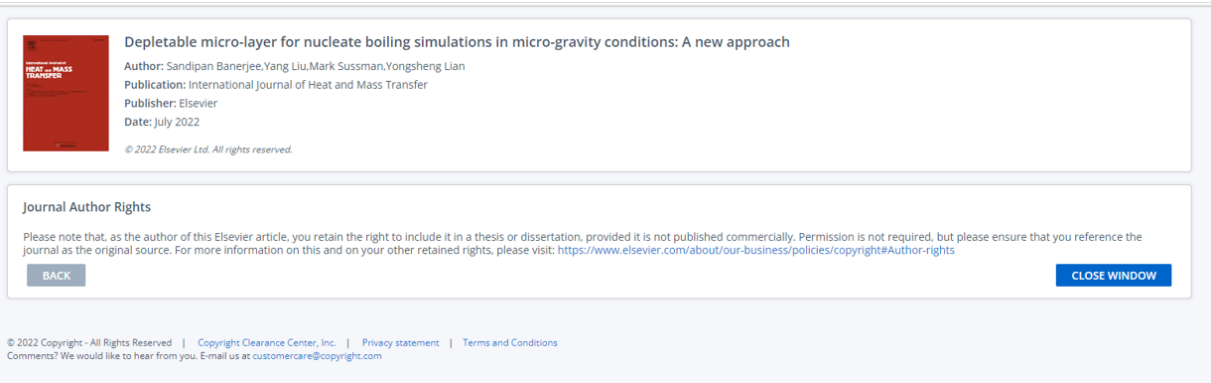

Figure 2. Permission letter for 2nd paper

CURRICULUM VITA

Sandipan Banerjee

Education

- PhD. in Mechanical Engineering (Expected: May 2022), University of Louisville, KY, USA, Recipient of University Fellowship which entails 4 years funding for doctoral studies.
- Master of Science in Mechanical Engineering, University of Delaware, DE, USA, August 2016
- Bachelor of Technology in Mechanical Engineering, West Bengal University of Technology, India, August 2008

Professional Positions

- PhD. Candidate, Mechanical Engineering Department, University of Louisville, KY. May 2017 - Present
- Fellow, Technology Commercialization, University of Minnesota, Twin Cities, MN, January 2021 - Present
- Graduate Research Assistant, University of Delaware, Newark, DE, September 2014 - August 2016
- Senior Engineer, Quest-Global, Bangalore, for OEM - Rolls-Royce, plc. June 2011 - May 2014

- Project Engineer, Wipro Technologies, Bangalore, for OEM - Harman Becker Automotive Systems, January 2009 - June 2011

Honors and Awards

- University Fellowship - 4 year funding for Doctoral studies awarded by J.B. Speed School of Engineering, University of Louisville to the most qualified new doctoral graduate students, 2017.
- Conference Travel Support -Awarded by Mechanical Engineering department at University of Louisville for supporting students to present their research in conferences, 2020.
- Conference Travel Support -Awarded by Graduate Student Council at University of Louisville for supporting graduate students to present their research in conferences, 2020.

Publications and Presentations

- Sandipan Banerjee, Yang Liu, Mark Sussman, Yongsheng Lian, "Depletable micro-layer for nucleate boiling simulations in micro-gravity conditions: A new approach", International Journal of Heat and Mass Transfer, Accepted, Impact Factor: 5.584.
- Sandipan Banerjee, Yongsheng Lian, Yang Liu, Mark Sussman, "A new method for estimating bubble diameter at different gravity levels for nucleate pool boiling", Journal of Heat Transfer, Feb 2022, 144(2): 021601, Impact Factor: 2.021.
- Sandipan Banerjee, Yongsheng Lian, "Data Driven Covid-19 Spread Prediction Based On Mobility and Mask Mandate Information", Journal: Applied Intelligence, 2020, 52, pages1969–1978 (2022), Impact Factor: 3.325.

- Sandipan Banerjee, Mark Sussman, Yongsheng Lian, "Dimensional Analysis in Error Reduction for Prediction of Nucleate Boiling Heat-flux by Artificial Neural Networks for Limited Dataset", Journal of Heat Transfer, Under Review.

- Sandipan Banerjee, Orlando Ayala, Lian-Ping Wang, "Direct Numerical Simulations of Small Particles in Turbulent Flows of Low Dissipation Rates Using Asymptotic Expansion", In Proceedings of the 5th Thermal and Fluids Engineering Conference, 2020, Full Paper.

- Sandipan Banerjee, Yongsheng Lian, Yang Liu, Mark Sussman, "A new hybrid approach for a depletable microlayer for nucleate boiling in microgravity conditions", In Proceedings of the 15th International Conference On Heat Transfer, Fluid Mechanics And Thermodynamics, Full Paper.

- Sandipan Banerjee, "Turbulent Collision Statistics of Cloud Droplets at Low Dissipation Rates", Master's Thesis, 2016 , University of Delaware.

- Sandipan Banerjee, Mark Sussman, Yang Liu, Yongsheng Lian, "A new hybrid approach for a depletable microlayer for nucleate boiling in microgravity conditions, 15th International Conference On Heat Transfer, Fluid Mechanics And Thermodynamics, Conference Presentation, 2021.

- Sandipan Banerjee, Mark Sussman, Yang Liu, Yongsheng Lian, "A Depletable Microlayer Approach for Nucleate Pool Boiling in Microgravity Conditions", 45th DCASS (Dayton-Cincinnati Aerospace Sciences Symposium)-Dayton, OH, Conference Presentation, 2020.

- Sandipan Banerjee, Orlando Ayala, Lian-Ping Wang, "Direct Numerical Simulations of Small Particles in Turbulent Flows of Low Dissipation Rates Using Asymptotic Expansion", In Proceedings of the 5th Thermal and Fluids Engineering Conference, Conference Presentation, 2020.

- Sandipan Banerjee, Yang Liu, Mark Sussman, Yongsheng Lian, "Nucleate Boiling Simulations at Earth Gravity and Reduced Gravity Using an Adaptive Moment Of Fluid (Mof) Method", GSRRC-Regional Research Conference-University of Louisville, 2020.

- Sandipan Banerjee, "Nucleate Boiling under different gravity values: Numerical Simulations & Data- driven Techniques", PhD Proposal Presentation , University of Louisville, 2020.

- Sandipan Banerjee, "Turbulent Collision Statistics of Cloud Droplets at Low Dissipation Rates", Master's Thesis Defense Presentation,, University of Delaware, 2016.

- Sandipan Banerjee, Orlando Ayala, Lian-Ping Wang, "Collision statistics of inertial particles suspended in turbulent flows of low dissipation rates", APS-DFD (American Physical Society-Division of Fluid Dynamics), Conference Presentation, 2015.